R. & M. No. 3648

MINISTRY OF AVIATION SUPPLY

AERONAUTICAL RESEARCH COUNCIL
REPORTS AND MEMORANDA

The Two-Dimensional Characteristics of a 12·2% Thick RAE 100 Aerofoil Section

By D. S. WOODWARD
Aerodynamics Dept., R.A.E., Farnborough

LONDON: HER MAJESTY'S STATIONERY OFFICE
1971
PRICE £1 15*s* 0*d* [£1·75] NET

The Two-Dimensional Characteristics of a 12·2% Thick RAE 100 Aerofoil Section

By D. S. WOODWARD

Aerodynamics Dept., R.A.E., Farnborough

Reports and Memoranda No. 3648*
January, 1969

Summary.

The 12·2% thick RAE 100 aerofoil section was chosen as being likely to fulfil the requirements for the basic aerofoil section of a series of swept-back wings designed to provide fundamental information on the high lift and stalling behaviour of swept wing aircraft. The choice was based upon previously published work on the stall characteristics of two-dimensional aerofoils, and the results presented show that the desired behaviour at high lift has been obtained.

The measurements of the aerofoil characteristics were obtained by surface pressure plotting. Not only were the overall forces and moments obtained from these measurements, but also the pressure distributions were analysed in three ways intended to provide information on the changes from the potential flow pressure distribution which are produced by the displacement thickness of the boundary layer.

CONTENTS

*Replaces RAE Technical Report 68 303—A.R.C. 31 374.

---

1. *Introduction.*

This Report describes the measurement, mainly by surface pressure plotting, of the two-dimensional characteristics of a 12·2 per cent thick RAE 100 aerofoil section. This aerofoil section had been selected, on the basis of existing empirical knowledge, to be the basic section of a series of wings in a general research programme aimed at clarifying the problem of the stall behaviour of swept wings, and it was clearly necessary to establish whether it had, in fact, the characteristics which were desired.

For the swept-wing series, a symmetrical section was required whose stall pattern would change from the leading-edge type to the trailing-edge type[1,2] within the Reynolds number range

$$0{\cdot}50 \times 10^6 < R_c < 0{\cdot}70 \times 10^6$$

The choice of the section was based on the empirical criterion, governing short bubble breakdown, due to Owen and Klanfer[3], combined with the detailed boundary-layer calculations on R.A.E. series aerofoils reported by Curle and Skan[4], and was further supported by the empirical correlation of Gault[2]. A short description of two-dimensional stall behaviour and the details of how the choice was made are given in Section 2.

Although the main point of interest in these tests was to verify the existence of the change in the stall pattern within the specified Reynolds number range, the opportunity was also taken of exploring more fully the behaviour of the aerofoil at Reynolds numbers higher than this range, in order to provide further comparative data for the swept-wing tests. The original values of the overall force coefficients derived from the integration of the measured pressure distributions showed a different relation between the normal and axial forces at positive and negative incidence which, it was found, could be reasonably accredited to the existence of camber in the model/airflow combination. A method for correcting the raw coefficients for the existence of this camber has been derived and is presented in Appendix A. Nevertheless, some scatter is still apparent in the values of form drag and quarter-chord pitching moments which have

been deduced from the corrected values of normal and axial force and pitching moment. This scatter appears to arise both from inaccuracies inherent in the method used to deduce the integrated coefficents and also from random inaccuracies in incidence setting. In order to provide better estimates of the force and moment coefficients the experimental data has been smoothed using the method described in Appendix B; the experimental data is presented and compared with the smoothed data in Section 6 and Figs. 17 to 28.

In addition, the experimental pressure distributions have been analysed by three methods which, although more particularly devised for use on the swept-wing results, have been used here in order to assess their relative merits and also to provide for a comparison with the results from the swept wing. Using these methods the experimental pressure distributions can be processed to yield values of certain parameters that feature prominently in thin wing potential-flow theory. In the case of a two-dimensional wing the difference between these derived values and the theoretical ones can be interpreted directly as a measure of the effect of the boundary-layer displacement thickness; in the case of a swept wing at high lift the situation is almost certainly more complex. The analysis methods are presented in Section 4.2 and the results are discussed in Section 6.2.

2. *The Choice of Aerofoil.*

It is now well known[1] that the stall patterns of two-dimensional aerofoil sections can be divided into at least three categories. These are

(a) trailing-edge stall
(b) leading-edge stall
(c) thin aerofoil stall.

It is fair to say that the category into which the stall pattern of any particular aerofoil will fall, at a given Reynolds number, depends, fundamentally upon the breakdown of the short separation bubble[1,5] that exists near the leading edge under high lift conditions. In case (a), the breakdown is delayed until after $C_{L\max}$, the stall being produced by separation of the turbulent boundary layer near the trailing edge; in case (b), breakdown occurs at $C_{L\max}$, the stall being caused by the breakdown; in case (c), the breakdown occurs prior to $C_{L\max}$, the stall being caused by the re-attachment point of the long bubble (which forms after breakdown of the short bubble) approaching the trailing edge. Unfortunately in spite of considerable amounts of research[3,5-12] no clearly defined fluid dynamic parameter has emerged which characterises the breakdown process, so that the conditions under which breakdown will occur still cannot be predicted with any degree of certainty.

However, Owen and Klanfer[3] have shown a strong correlation (at least on conventional aerofoils of small camber) between short bubble breakdown and the Reynolds number based upon the displacement thickness of the laminar boundary layer at separation ($R^*_{\delta_s}$). The correlation suggested that breakdown of the short bubble flow was likely to occur in the range

$$450 < R^*_{\delta_s} < 550$$

and this in turn suggests that the stall pattern of a particular aerofoil may change with Reynolds number, a suggestion which is corroborated by Gault's correlation of two-dimensional stalling characteristics (*see* Fig. 1). Now on any aerofoil on which bubble breakdown occurs, it is observed experimentally that the breakdown incidence increases, usually quite rapidly, with increase of Reynolds number, so that, in spite of the correlation shown by Owen and Klanfer, before much confidence can be expressed in the criterion it is necessary to demonstrate that it also indicates this trend with increasing Reynolds number. For this to be so, the ratio

$$\frac{R^*_{\delta_s}}{\sqrt{R_c}} = k$$

must decrease with increasing incidence, and the smaller the negative value of $dk/d\alpha$ the more rapid will be the rise of the breakdown incidence with Reynolds number. Curle and Skan[4] have performed laminar boundary layer calculations on the inviscid pressure distributions of the RAE sections 100, 101, 102, 103 and 104 of both 6 per cent and 10 per cent thickness/chord ratio, in order to evaluate k at a number of incidences in a range where short bubble breakdown is likely to occur. The results of these calculations are reproduced in Fig. 2 where it will be seen that k does indeed fall with increasing incidence at first as is required, but that, having reached a rather ill-defined minimum, it subsequently rises again (i.e. $dk/d\alpha$ becomes positive).

Now this behaviour is significant because it implies that if at a constant Reynolds number, short bubble breakdown has not occurred before the aerofoil has attained the incidence for which k is a minimum, then it can never occur and the aerofoil must, of necessity, have a trailing-edge stall pattern. Furthermore, using the numerical values of the criterion, we may simply calculate the range of values of R_c over which the criterion indicates that the stall pattern will change from the leading to the trailing-edge form. Finally in the same report Curle and Skan[4] show that the minimum values of k appear to correlate well with the nose radius, at least for this family of aerofoils, once again showing general agreement with the form of Gault's[2] correlation, but, more importantly, allowing the minimum values of k to be estimated for aerofoils other than those for which the calculations were performed.

In spite of the evidence presented in support of the Owen/Klanfer criterion, there is also considerable other evidence[5,7,8,9,10,12,25] suggesting that $R^*_{\delta_s}$ is not a fundamental parameter of the bursting process so that it is important to regard estimates of stall pattern based upon the use of the Owen/Klanfer criterion as no more than somewhat crude estimates which will be likely to indicate the correct order of magnitude of the Reynolds number at which the changes will take place. However, accepting these reservations it can be seen that the use of the criterion in conjunction with the Curle and Skan calculation allows an estimate to be made of the chordal Reynolds number at which a change from a leading-edge to a trailing edge stall pattern can be expected to occur for any aerofoil in the RAE 100–104 series within certain thickness limits. Nevertheless, since all the data reported above relates only to two-dimensional sections it is necessary to make further assumptions about the equivalence of two-dimensional and swept-wing sections and their associated chordal Reynolds numbers, before it can be used to enable a section to be selected for use in the swept-wing series.

Fig. 3 shows two alternative methods of relating the aerofoil geometry and the chordal Reynolds number on an infinite swept swing and the implications of both these definitions were examined in choosing the section, although, as will be seen, the differences were fairly small.

In this Report, it has been assumed that the yawed wing conditions correspond to the two-dimensional case, and although this fixes the geometry of the two-dimensional section it still permits two separate estimates to be made of the chordal Reynolds number at which the stall pattern will change; one derived from the sheared wing geometry and translated into a yawed wing value by the factor $\cos^2 \phi$ and the other derived directly from the yawed wing geometry. Now the original requirement for the swept wing series was for a section that, on a 35° swept back wing, would have a *sheared wing* chordal Reynolds number for stall pattern change in the range

$$0{\cdot}90 \times 10^6 < R_{\bar{c}} < 1{\cdot}0 \times 10^6.$$

The Curle and Skan[4] calculations and the upper and lower bounds of the Owen and Klanfer[3] criterion predict, for a 10 per cent thick RAE 100, a stall pattern change in the range

$$0{\cdot}84 \times 10^6 < R_{\bar{c}} < 1{\cdot}03 \times 10^6.$$

This leads immediately to an equivalent two-dimensional (or yawed wing) section of a 12·2 per cent thick RAE 100 having a predicted stall pattern change in the range

$$0{\cdot}57 \times 10^6 < R_c < 0{\cdot}69 \times 10^6.$$

If, in the same way as before, we estimate directly, for a 12·2 per cent thick RAE 100, the Reynolds number range in which the stall pattern can be expected to occur, we obtain

$$0{\cdot}50 \times 10^6 < R_c < 0{\cdot}61 \times 10^6.$$

Clearly the difference between the above two predictions is less that the uncertainty in the Owen and Klanfer[3] criterion and as such encourages one to believe that the salient features of the transformation from an infinite swept wing to a two-dimensional wing have been taken into account, and consequently the 12·2 per cent thick RAE 100 section was selected as the *yawed wing* section of the 35° swept-back series, and this two-dimensional investigation was carried out in order to check the predictions.

3. *Description of Model and Test Method.*

The model was constructed of laminations of teak arranged around a steel spar and centre sheet with a Tufnol trailing edge. The chord of the model was 20 in and it spanned the $8\frac{1}{2}$ ft height of either the No. 1 and No. 2 $11\frac{1}{2}$ ft × $8\frac{1}{2}$ ft tunnels at R.A.E. Farnborough, giving a geometric aspect ratio of 5·1. To avoid troubles with synchronising the movements of the upper and lower turntables, the model was fixed only to the lower turntable and was mounted in a separate pivot in the upper turntable; the model stiffness was such that even under the most severe stall conditions the calculated overall twist over the model span was less than 0·01 degree and at $C_{L\max}$ was of the order of 0·002 degree.

The pressure distribution on the aerofoil section was determined from 61 pressure tappings arranged in an approximately 3 in wide band along the tunnel centre line as shown in Fig. 5 and tabulated in Table 1. Each tapping consisted of a 0·50 mm (0·0197 in) diameter hole drilled into a 0·079 in O.D. × 0·053 in. I.D. cupro-nickel tube situated 0·02 in. below the model surface, which was then taken spanwise as shown in Fig. 5 to emerge below the tunnel floor. The spanwise staggering of the holes near the leading edge was adopted in an attempt to minimise the effects of the pressure holes upon the short separation bubble, since Bacon *et al*[13] have shown that cavities of this type can magnify acoustic disturbances sufficiently to materially alter, locally, the transition position in an attached boundary layer and have also indicated that a separated flow might be even more susceptible to this effect.

In addition to this main group of pressure tappings, seven tubes were run spanwise, each at a constant chordwise position, on both the upper and lower surfaces of the aerofoil, and on either side of the main group of pressure holes. These tubes had a number of holes drilled in them at intervals along their length corresponding to particular spanwise stations. By covering all except one hole in each tube with cellulose tape, and plotting local C_p against incidence over a small positive and negative range as shown in Fig. 6, the spanwise variations of incidence and camber could be explored. This part of the investigation was initially very much a sideline but in the final analysis the results from it assume a fair significance.

The pressure tubes forming the main group of pressure tappings were each connected to one tube of a 4 ft high multi-tube manometer, as were also the tunnel reference pressures. This manometer had eight 40 watt fluorescent tube lights mounted behind a translucent perspex panel which in turn, was situated immediately behind the manometer tubes. The strong diffused lighting thus produced, coupled with dyed manometric fluid, appropriate colour filters and very fine grain film, enabled 35mm photographs to be obtained of sufficiently good quality that accurate reading of the manometric heights could be subsequently carried out on a Benson-Lehner 'Boscar' film reader. The punched paper tape record of these manometric heights was then processed in a digital computer, giving a punched paper tape output of x/c, z/c, C_p etc. suitable for direct use on an automatic graph plotter. The overall forces were subsequently evaluated by using an Amsler moment/area integrator to measure the net areas contained within the curves plotted by the graph plotter. Study of the figures produced using this method suggests that the error involved in reading any one pressure is within the range ± 1 per cent of the dynamic head; whilst the integrated forces and moments also appear to be accurate to within ± 1 per cent (*see* Section 5.1). Movement of the liquid levels within the manometer tubes was kept to the maximum possible over a wide range of tunnel speeds and wing incidence by altering the inclination of the manometer to the vertical and by changing the density of the manometric fluid. Methyl alcohol (s.g. $\simeq$ 0·8) was used at the lower speeds and carbon tetrachloride (s.g. $\simeq$ 1·6) was used at the higher speeds.

In addition to the measurement of the overall pressure forces the total sectional drag (profile drag) was measured using a pitot rake to record the loss in total head within the wake; wake surveys were made with the rake situated at 0·5 and 1·0 chord downstream of the wing trailing edge, and, in addition to the surveys carried out with the rake aligned along the wind direction, surveys were also made with the rake inclined at half the wing incidence to the free stream direction. The total drags were determined from the loss in total head by the 'F method' of Young[14] described by Pankhurst and Holder[15]. In this method the static pressure is assumed constant across the wake but a factor is derived from the measured static pressure outside the wake by which the correct drag may be obtained from the integrated total head loss. In common with previously published measurements[16] it was found that the static pressure was essentially constant across the wake at both downstream positions but differed from the free stream static pressure at the 0·5 chord downstream station.

4. *Methods of Analysis.*

4.1. *Evaluation of Overall Characteristics from Local Pressure Measurements.*

Referring to Fig. 4 it is clear that the force in the direction of the z-axis, F_z can be written

$$F_z = \oint p\, dx$$

where the integral is taken completely round the surface of the aerofoil, so that the sectional normal-force coefficient

$$C_N = \frac{F_z}{\frac{1}{2}\rho U_0^2 c} = \oint \frac{p - p_0}{\frac{1}{2}\rho U_0^2} d\left(\frac{x}{c}\right)$$

$$= \oint C_p\, d\left(\frac{x}{c}\right), \tag{1}$$

where c = aerofoil chord
ρ = fluid density
U_0 = fluid velocity at infinity
p_0 = fluid static pressure at infinity.

Equation (1) may be re-written as

$$C_N = \oint C_p\, d\left(\sqrt{\frac{x}{c}}\right)^2 = 2\oint \left\{C_p \sqrt{\frac{x}{c}}\right\} d\left(\sqrt{\frac{x}{c}}\right), \tag{2}$$

this form being more convenient to use since it reduces the severity of the peaks of the integrand near the leading edge. In a similar fashion to above the sectional axial-force coefficient may be written

$$C_T = -\oint C_p\, d\left(\frac{z}{c}\right) \tag{3}$$

and this may be left in this form. The sectional pitching-moment coefficient about the leading edge (positive in the nose-up, or trailing edge down, sense) may be written

$$C_m = -\oint \left(C_p \frac{x}{c}\right) d\left(\frac{x}{c}\right) - \oint \left(C_p \frac{z}{c}\right) d\left(\frac{z}{c}\right) \tag{4}$$

and this is most conveniently split into the two components, the first being taken in conjunction with equation (2), in which case it may be written

$$C_{m_x} = -2\oint\left\{C_p\sqrt{\frac{x}{c}}\right\}\left\{\sqrt{\frac{x}{c}}\right\}^2 d\left(\sqrt{\frac{x}{c}}\right) \tag{5}$$

and the second being taken in conjunction with equation (3) and left in the form in which it is written in equation (4).

Thus it can be seen that C_N and C_{m_x} are twice the area and the second moment of area respectively of the region enclosed between the upper and lower surface plots of $C_p\sqrt{x/c}$ against $\sqrt{x/c}$, and, in a similar way, C_T and C_{m_z} are the area and first moment of area respectively of the enclosed figure formed by plotting C_p against z/c. Figs. 8 and 9 show two examples of the type of results sheet that was plotted to enable the forces and moments to be evaluated using an Amsler moment/area integrator and the above equations. The odd kink in the upper surface plot of $C_p\sqrt{x/c}$ against $\sqrt{x/c}$ in Fig. 9 is genuine and is caused by the local modifications to the pressure distribution produced by the presence of a short bubble.

4.2. *Analysis of Pressure Distributions.*

4.2.1. *Introduction.* For several reasons, one of the interesting facets of the tests on the swept wings using this 12·2 per cent t/c RAE 100 section, will be the comparison of the experimentally determined load distribution with those predicted by the standard R.A.E. method[17,18] for swept wings. However, as is usual, the prediction method is restricted to potential flow, so that the presence of the boundary layer in the experiments makes it extremely difficult to draw meaningful conclusions from the comparison.

Brebner and Bagley[19] have shown that, by measuring the boundary-layer displacement thicknesses on both surfaces of a two-dimensional aerofoil section and adding this to the basic shape, good predictions of the pressure distribution can be obtained using potential flow calculation methods. However, in the case of a swept wing the prospect of obtaining sufficient experimental boundary-layer measurements in order adequately to define the displacement surface[26] is daunting. Moreover present methods of calculating three-dimensional boundary-layer development are almost certainly inadequate, particularly under high lift conditions. Failing this complete method of accounting for the presence of the boundary layer, some more simple method needs to be devised, preferably one which allows simple graphical comparisons to be made between the effects due to the presence of the boundary layer on the pressure distributions of different aerofoils and which will also demonstrate the salient effects of changes in Reynolds number. In this Report, three simple methods are examined; in each of these, effective mean values of certain parameters which determine the load distributions in potential flow are derived from the experimental results. In the first method only one free parameter is used, but in the other two methods two free parameters are used, and, although they are the same parameters in both cases, the contexts from which they are obtained are different.

The basic assumption underlying all three methods is that the measured pressure loading on a thick aerofoil in a viscous fluid consists of three factors, thus

$$\begin{array}{l}\text{The chordwise loading}\\ \text{on a thick aerofoil}\\ \text{in a viscous fluid}\end{array} = \left[\begin{array}{l}\text{The chordwise}\\ \text{loading on a}\\ \text{thin wing in}\\ \text{potential}\\ \text{flow}\end{array}\right] \times \begin{array}{l}\text{Thickness effects}\\ \text{in potential flow}\end{array} \times \begin{array}{l}\text{Boundary layer}\\ \text{effects on}\\ \text{thick aerofoil}\end{array} \tag{6}$$

The expression within the square brackets represents the loading on a thick aerofoil in potential flow and is written in the same form as is used in the standard Weber[20] formula

$$\Delta C_p = -2 \sin 2\alpha \sqrt{\frac{1-x}{x}} \frac{(1+S_1(x))(1+S_3(x))}{1+[S_2(x)]^2}, \tag{7}$$

where

$2 \sin 2\alpha \sqrt{\frac{1-x}{x}}$ = the chordwise loading on a thin wing in potential flow.

$\frac{(1+S_1(x))(1+S_3(x))}{1+[S_2(x)]^2}$ = thickness effects in potential flow. The S-functions are functions of x obtained from integrals across the chord involving the aerofoil ordinates.

Therefore, this portion of the assumption in equation (6) is in accordance with well-established practice, so that the only part that remains to be justified is that which suggests the boundary-layer effects can be expressed as a multiplying function on the loading in potential flow rather than as an additional loading. This assumption is made merely in order to facilitate the analysis and no justification will be attempted here. However it will be seen below that in its simplest form it, also, is accepted practice.

4.2.2. *The reduced incidence method* (*Method* 1). This method is in common usage, and consists of re-defining the value of the incidence α to a new value, α_b say, so that the experimentally determined value of C_N, is given by

$$C_N = \int_0^1 -\Delta C_{p_b} \, d\left(\frac{x}{c}\right), \tag{8}$$

$$\Delta C_{p_b} = \frac{-2 \sin\left[2\alpha\left(\frac{\alpha_b}{\alpha}\right)\right](1+S_1)(1+S_3)}{1+(S_2)^2} \sqrt{\frac{1-x}{x}} \tag{9}$$

$$\simeq -\frac{\alpha_b}{\alpha} \frac{2 \sin 2\alpha (1+S_1)(1+S_3)}{1+(S_2)^2} \sqrt{\frac{1-x}{x}}$$

for small values of α

$$= \frac{\alpha_b}{\alpha} \Delta C_p \tag{10}$$

if S_1, S_2, S_3 are each obtained from the basic aerofoil shape ignoring the boundary-layer displacement thickness. Defined in this way, the parameter (α_b/α) becomes the third term in equation (6) and thus provides a measure of the boundary-layer effect upon the pressure distribution; it might be expected to tend to unity in the case of vanishingly small viscosity.

4.2.3. *The overall force method* (*Method* 2). The obvious step to improve the characterisation of the pressure distribution over that achieved by the previous method is to introduce another parameter

so that the experimental value of the pitching moment, C_{m_x}, may also be correctly simulated. Thus we may write

$$\left.\begin{aligned} C_{m_x} &= \int_0^1 \Delta C_{p_b}\left(\frac{x}{c}\right) d\left(\frac{x}{c}\right) \\ \text{and} \qquad C_N &= \int_0^1 \Delta C_{p_b}\, d\left(\frac{x}{c}\right) \end{aligned}\right\} \tag{11}$$

where now

$$\Delta C_{p_b} = -\frac{\alpha_b}{\alpha}\,\frac{2\sin 2\alpha\,(1+S_1)(1+S_3)}{1+(S_2)^2}\left(\frac{1-x}{x}\right)^n \tag{12}$$

$$= -\left(\frac{\alpha_b}{\alpha}\right)\left(\frac{1-x}{x}\right)^{n-\frac{1}{2}}\,\frac{2\sin 2\alpha\,(1+S_1)(1+S_3)}{1+(S_2)^2}\,\sqrt{\frac{1-x}{x}}$$

$$= \left(\frac{\alpha_b}{\alpha}\right)\left(\frac{1-x}{x}\right)^{n-\frac{1}{2}}\,\Delta C_p \tag{13}$$

if S_1, S_2, S_3 are again determined from the aerofoil section shape ignoring the boundary-layer displacement thickness. Defined in this way the function $(\alpha_b/\alpha)\,((1-x)/x)^{n-\frac{1}{2}}$ provides a measure of the boundary-layer effect upon the pressure distribution and will be seen to have two disposable parameters (α_b/α) and n.

From Equations (11) and (12) it can be seen that the chordwise centre of pressure

$$X = -\frac{C_{m_x}}{C_N}$$

is independent of α and α_b/α and dependent only on 'n' (for a given thickness distribution), so that the effective value of 'n' for the experimental pressure distribution may be deduced from the experimental pitching moment (C_{m_x}) and a graph linking X and n obtained from the potential flow formulae with varying n. Although, having deduced a value of n, it is fairly easy to calculate α_b/α directly, it is somewhat easier to proceed using the assumption of small α again to write

$$\frac{\alpha_b}{\alpha} = \frac{\left(\dfrac{C_N}{\alpha}\right)_{\text{experimental}}}{\left(\dfrac{C_N}{\alpha}\right)_{\text{potential}}}$$

so that the value of α_b/α may be obtained directly from a graph linking C_N/α and n obtained from the potential flow formulae as before, combined with the experimental value of C_N/α. The relations connecting X and C_N/α to n for the potential flow around a 12·2 per cent t/c RAE 100 thickness form are shown

in Fig. 35. Also shown in Fig. 35, for comparison, are the equivalent relations for an infinitely thin wing, given by Küchemann[17]

$$\left.\begin{aligned} X &= \frac{1-n}{2} \\ \frac{C_N}{\alpha} &= \frac{4\pi n}{\sin \pi n} \end{aligned}\right\} \tag{14}$$

thus showing the fairly considerable effect of the finite thickness.

4.2.4. *The direct pressure distribution method* (Method 3). In this method, instead of attempting to produce agreement between the experimental overall characteristics and those obtained from the theoretical expressions, we attempt to manipulate, mathematically, the measured pressure distribution so that the numerical values of the free parameters can be determined from it directly, and not seeking to obtain agreement between the overall characteristics, although the magnitude of the discrepancy thus introduced will need to be investigated ultimately.

If we assume that the multiplications in equation (6) can be regarded as commutative, then it may be re-written

The chordwise loading on a thick aerofoil in a viscous fluid	÷	Thickness effects in potential flow	=	The chordwise loading on a thin wing in potential flow	×	Boundary layer effects on thick aerofoil

(15)

If we choose the same parameters to define the boundary-layer effect as in the previous section, and let ΔC_{p_c} represent the experimentally measured pressure loading, then

$$\frac{-\Delta C_{p_c}(1+S_2^2)}{(1+S_1)(1+S_3)} = \frac{\alpha_b}{\alpha}\left(\frac{1-x}{x}\right)^{n-\frac{1}{2}} 2 \sin 2\alpha \sqrt{\frac{1-x}{x}}$$

which may also be written

$$\log\left[\frac{-\Delta C_{p_c}(1+S_2^2)}{(1+S_1)(1+S_3)}\right] = \log\left(2 \sin\left[2\alpha \frac{\alpha_b}{\alpha}\right]\right) + n \log\left(\frac{1-x}{x}\right) \tag{16}$$

so that the boundary-layer effect parameters (α_b/α) and n may be evaluated by drawing a mean straight line through a plot of the left hand side against $\log((1-x)/x)$ and evaluating the intercept and slope respectively. A typical set of such lines is shown in Fig. 36 from which it can be seen that the data points form reasonably good straight lines.

From equation (15) it can be seen that the term on the left hand side can be thought of as a quasi-thin wing loading derived from the experimental measurements which however still contains the effects of the thick wing boundary layer. It is felt that this may be a useful concept, especially in dealing with data from finite swept wings, in that it allows comparisons between theory and experiment to be conducted at the relatively simple thin wing level rather than at the more complex thick wing level. It should be pointed out that the previous methods can also be viewed in this light since the relations which were used to estimate the values of n and α_b/α were those which were obtained by calculating the values of X and C_N/α for the thick wing as the thin wing parameters were varied. However in the case of the previous methods there is no direct check that the assumed form of the boundary-layer effect resembles the observed changes in the pressure distribution such as is afforded by the analysis of Method 3.

4.2.5. *Additional comments.* The two parameters n and (α_b/α) may be loosely thought of as representing the camber and reduction in incidence which characterises the effect of the boundary-layer displacement thickness upon the pressure distribution on an aerofoil section. However, there are important differences in concept between the present analysis and that of Brebner and Bagley[19] which should not be overlooked. Firstly, allowing n to vary from its potential flow value also implies a variation in C_N/α as shown in Fig. 35 and equation (14); consequently the derived values of (α_b/α) depend, not only on the difference between the measured and potential-flow values of normal-force coefficient, but also on the differences between n and $\frac{1}{2}$, so that the values of (α_b/α) cannot be interpreted as being descriptive of the geometry of the displacement surface. Secondly, although n (and thus the effective camber shape) is allowed to vary with incidence, the magnitude of the camber is directly related to the incidence value as it is introduced as a modified incidence loading. Thus it can be seen that the concept underlying the present analysis is rather more restrictive than that of Brebner and Bagley[19] where the incidence and camber terms are independent and are added to obtain the final loading. Clearly, comparable analyses employing the previous concept could be devised using some type of pre-specified camber shape (e.g. parabolic) which might well be somewhat better, in fact allowing 'n' to vary is a step which is plainly open to criticism since there must be a square root singularity in the basic thin wing loading near the leading edge.

However, the connections of this work with the swept wing investigations call for analysis methods which are compatible with the best existing methods for predicting the loadings appearing on swept wings. Therefore, since the usefulness of the concept of a varying value of n has been convincingly demonstrated in the standard R.A.E. method for swept wings[17,18], it is felt that the present analysis methods may also be held to be justifiable.

5. *Corrections to Experimental Measurements.*

5.1. *Correction for Camber in the Tunnel Flow.*

The initial plotting of the uncorrected force coefficients derived from the graphical integrations showed a relatively large and consistent difference between positive and negative incidence as shown in Fig. 10. This difference was not altogether unexpected since the measurements of $\Delta\alpha^*$ (defined in Fig. 6), which were derived from the pressure measurements taken on the additional spanwise tubes, had shown that an appreciable amount of camber was present in the combination of wing and airflow as can be seen from Fig. 7; calculations based upon the measured ordinates of the model indicate that about 25 per cent of this camber can be attributed to inaccuracies in the manufacture of the model, and so it must be assumed that the remainder is inherent in the tunnel flow.

A method of correcting the force and moment coefficients for this camber effect was devised and is presented in detail in Appendix A together with further evidence in support of the general hypothesis and the magnitudes of the calculated effects. Comparison of Figs. 10 and 11 shows that this correction method results in an acceptable collapse of the normal and axial force data at both positive and negative incidences. However, it could be argued that in applying any method of correction for flow camber there is the possibility of severely distorting the basic data. Figs. 12, 13 and 14 compare the basic data (denoted by the suffix 'c') and the data corrected for flow camber (denoted by the superscript $\hat{}$) and show that the corrections to normal force and incidence (Fig. 12) have not changed the character of the variation of C_N/α with α in any way, nor have the corrections to C_{m_x} and C_N altered the variation of the centre of pressure with incidence (Fig. 13), whilst Fig. 14 shows the excellent collapse of the data at positive and negative incidences defining the variation of the point of action of the axial force with the magnitude of the axial force. In this figure the uncorrected data points (suffix 'c') have been respresented by the mean lines only, in the interests of clarity, but it should be pointed out that the scatter of the uncorrected data is of the same order as that shown by the corrected data. It is convenient at this point to comment on the apparently large scatter shown in Figs. 12 and 13. This scatter arises primarily because a large scale has been chosen in order to show the differences between the uncorrected and the corrected data, in fact, as shown in Appendix B, the errors in the overall characteristics which produce this scatter are by no means excessive being

Normal force C_N	$\pm 0{\cdot}7\%$
Pitching moment C_{m_x}	$\pm 1{\cdot}4\%$
Incidence α	$\pm$ 0·034 degree.

These errors are, however, somewhat greater than those reported by Brebner and Bagley[19] in a similar investigation particularly with respect to the accuracy of incidence setting where they report being able to obtain accuracies of $\pm 0{\cdot}01$ degree by using a light beam reflected from a small mirror set in the surface of the model. There appears to be no satisfactory reason why the scatter should appear to increase with decreasing Reynolds number.

Despite this scatter the variations are sufficiently well defined for mean lines to be drawn in and used with a fair degree of confidence as described below and in Appendix C.

5.2. *Further Corrections.*

The experimental results, when corrected for flow camber, were used in two ways. In the first, values of the lift, drag, and pitching-moment coefficients were calculated directly from the values of $\hat{C}_N$, $\hat{C}_T$, $\hat{C}_{m_x}$, $\hat{C}_{m_z}$ and $\hat{\alpha}$, after these had been further corrected for tunnel blockage and constraint, and all these fully corrected values are tabulated in Table 4. The fully corrected set of coefficients are still designated by the $\hat{}$ superscript, and, in practice, no confusion should arise between the values before and after correction for blockage and constraint, since the former are used only in Figs. 11, 12, 13 and 14 and the fact is noted on these figures. In the second, which is described in detail in Appendix C, smoothed values of the force and moment coefficients were generated by reading off values from the mean lines drawn in Figs. 11, 12, 13 and 14, and similar figures drawn for the post-stall regime which are not shown in this Report. These values were then corrected for tunnel blockage and constraint and the resulting values, designated by the superscript $-$, are tabulated in Table 5.

In the figures that follow, both the smoothed points ($\bar{C}_L$ etc.) and the corrected basic data points ($\hat{C}_L$ etc.) are plotted in order to show that the smoothing process was effective. It is felt that reasonable confidence can be placed in the smoothed values so obtained, particularly since only a small amount of feedback to the mean lines drawn in Figs. 11, 12, 13 and 14 was necessary in order to achieve smooth carpet plots of the data variation with Reynolds number and also to achieve full compatibility with the basic data ($\hat{C}_L$ etc.).

The constraint corrections applied were the conventional ones to incidence and pitching moment given by Pankhurst and Holder[15] for a two-dimensional wing in a solid-walled tunnel; the pitching-moment correction has been applied to the total pitching-moment values only ($C_{m_{c.4}}$). C_{m_x} and C_{m_z} values quoted are the measured values corrected only for blockage. Up to the stall, conventional solid and wake blockage corrections using the profile drag values were applied; after the stall the Maskell wake blockage correction[23] was applied to the increment in form drag over and above the form drag value at the stall, irrespective of the lift carried by the wing.

5.3. *Effects of Mach Number Variation.*

As the tunnel in which these tests were carried out has no facility for varying the air density, the variation of the forces and moments with Reynolds number was investigated by altering the windspeed in the usual manner. The method of altering the Reynolds number, of course, produces a simultaneous variation in Mach number, the effects of which are usually assumed to be small provided that the Mach number is reasonably small. However, recent experience has tended to suggest that, on wings developing high lift, this assumption may cease to be valid at much lower Mach numbers than hitherto had been expected.

In this Report an attempt has been made to indicate that the likely Mach number effects, within the range used in the tests, are small by calculating the pressure distributions that would be obtained on the 12·2 per cent t/c RAE 100 profile in potential flow over a range of incidence and Mach number, using the standard R.A.E. method. From Table 2 it can be seen that the overall loads predicted by this method

change very little within the Mach number range tested, however greater variation with Mach number of the pressure coefficient at specific points was noted, and so the predicted and experimental changes of local pressure coefficient at constant incidence with varying Mach number are compared in Figs. 15 and 16. These figures show quite clearly that the changes observed in the experimental results are much larger than those predicted theoretically and in Fig. 15—where the predicted changes are most marked—the experimental variation is of opposite sign to that predicted. It would therefore appear reasonable to assume that the changes in pressure distribution and overall loads measured in these tests due to changes in free stream speed are primarily a Reynolds number effect, the changes due to compressibility being very small. This opinion agrees with that expressed by L. R. Wootton in a recent paper[21], where some evidence was presented to indicate that significant Mach number effects do not occur below a Mach number of approximately 0·2 for aerofoil sections of moderate thickness exhibiting trailing edge stall characteristics.

6. *Presentation and Discussion of Results.*

6.1. *Overall Forces and Moments and their Relation to the Chordwise Pressure Distributions.*

Figs. 17 to 28 show the $C_L \sim \alpha$, $C_L \sim C_D$ and $C_{m_{c/4}} \sim C_L$ characteristics of the aerofoil over the Reynolds number range. These figures are primarily intended to present the fully corrected experimental results, but are also used to demonstrate the validity of the smoothing process by presenting the results from this as well.

In Figs. 17 to 19, prior to the stall, the agreement between the fully corrected experimental results obtained at both positive and negative incidences is excellent and consequently the lift curve is well defined. However the agreement deteriorates at the lower Reynods numbers shown in Fig. 20, and in some of these figures large variations between individual points are shown in the post-stall regime. There are two main reasons for the scatter in the post-stall region, one of which may be connected with the poor agreement between the pre-stall values at the lower Reynolds numbers.

Firstly, due to the camber in the wing/airflow combination, the stall is not identical at positive and negative incidences, and the difference between the two appears to be accentuated by reducing the Reynolds number (*see* for example Fig. 19). This could be interpreted as indicating that the short bubble (and through this the whole upper surface boundary layer) becomes increasingly sensitive to the local pressure distribution as the Reynolds number is reduced and bursting conditions are approached. It would then be reasonable to expect to find this reflected in differences between the measured coefficients at positive and negative incidences just before the stall, and this might explain the discrepancies shown in Fig. 20. Alternatively, of course, it may be that different camber corrections should be used at the lower tunnel speeds.

Secondly the flow in the post-stall condition is highly unsteady and, although an attempt was made to take the photographs at a sensible mean condition, it is quite clear, in a number of cases, that this was, in fact, not achieved.

The experimental form-drag results shown in Figs. 21 to 24 show a fairly appreciable scatter even in the pre-stall region; however this is not really surprising since the form drag is computed as the small difference between two relatively large numbers, one of which ($\hat{C}_N \sin \hat{\alpha}$) depends strongly on incidence, so that small errors in incidence setting will be revealed most strongly on these figures. In general the scatter is slightly worse than that shown by similar measurements by Brebner and Bagley[19] and the reasons for this are examined in Appendix B. The most notable feature of Figs. 21 to 23 is the intersection of the form drag (= integral of the pressure forces in the drag direction) curve and the profile drag (= total sectional drag) curve, implying a resultant forward thrust from the skin-friction forces. Possible ways in which this anomalous result may have arisen are discussed in Appendix D, and in view of this crossover of the two curves it is clearly not appropriate to discuss the variation of skin friction (= profile drag–form drag) over the incidence range.

Figs. 25 to 28 show the variation of the pitching moment about the quarter-chord point with lift and Reynolds number. A fair amount of scatter is again apparent even though these values are almost independent of the exact value of the incidence setting, therefore this scatter must be derived primarily from errors involved in the curve drawing and planimetry processes as discussed in Appendix B. The slightly

unstable pitching-moment variation up to the stall arises from the C_{m_x} component (i.e. the chordwise centre of pressure is forward of 0·25 c) and would be larger but for the opposing C_{m_z} component.

Throughout Figs. 17 to 28 it will have been seen that the smoothed results ($\bar{C}_L$, $\bar{C}_D$ etc.) form a sensible mean through the scatter of the experimental measurements, with the possible exception of some of the post-stall parts of the $C_L \sim \alpha$ relations. However, jumping ahead to Fig. 32, it will be seen there that the post-stall smoothed results show a consistent variation with Reynolds number, and this provides additional evidence for believing that the smoothed results, even in this region, provide an acceptable description of the aerofoil characteristics. In view of this the graphs summarising the aerofoil behaviour through the Reynolds number range have been plotted using only the smoothed results and the remainder of the discussion will be devoted to the consideration of the trends indicated by these graphs in relation to the chordwise pressure distributions of Fig. 30.

As was to be expected, the most significant variations with Reynolds number in this range occur in the lift coefficient, therefore these variations have been presented in detail by plotting the $C_L \sim \alpha$ curves in a carpet fashion, prior to the stall in Fig. 31 and post-stall in Fig. 32. The smooth variation of the lift coefficient with Reynolds number at constant incidence is notable in both Figs. 31 and 32, and the variation at $\alpha = 14°$ is particularly remarkable in that it appears to go through two critical regions, from fully separated flow at $R_c = 0{\cdot}55 \times 10^6$, through a partially separated flow region, to a fully attached flow condition at $R_c = 1{\cdot}78 \times 10^6$.

From the chordwise pressure distributions plotted in Fig. 30 and from the movement of the turbulent separation front plotted in Fig. 29, it will be clear that the stall pattern at $R_c = 1{\cdot}33 \times 10^6$ is of the trailing edge variety, and this is true also of the stall patterns at $R_c = 1{\cdot}78 \times 10^6$ and $R_c = 0{\cdot}91 \times 10^6$. However if we consider the incidence range between the first onset of boundary-layer separation at the trailing edge and the complete breakdown of the flow over the leading edge, it will be seen from Fig. 32 that, as the Reynolds number is reduced, this incidence range is also reduced, in fact, quite drastically reduced. This reduction indicates a growing tendency towards a leading-edge stall pattern, and it will be noted that, by the time the Reynolds number has been reduced to $R_c = 0{\cdot}55 \times 10^6$, the first loss in lift coincides with complete flow breakdown over the whole of the upper surface, as is predicted by the Owen/Klanfer[3] criterion from the calculations of Curle and Skan[4]. In terms of the three stall patterns discussed in Section 2, this stall can only be classified as a leading-edge stall, however Gault[2] in his correlation (*see* Fig. 1) introduces a fourth type, mixed leading- and trailing-edge stall pattern, which would seem to describe this pattern rather better, since the severe rounding of the lift curve just prior to the stall is indicative of a strongly deteriorating condition in the turbulent boundary layer near the trailing edge. The test conditions on this aerofoil have been marked in on Gaults correlation (Fig. 1) from which it can be seen that, at the three higher Reynolds numbers, the stall pattern is correctly predicted as being of the trailing-edge type (or possibly the mixed type). However, at the lower Reynolds numbers, where admittedly Gault's data is rather sparse, the stall is incorrectly predicted to be of the thin aerofoil type.

The sharpness of the trailing-edge stall at $R_c = 1{\cdot}78 \times 10^6$ is worthy of comment, particularly in relation to an analysis of sudden stall carried out by Evans and Mort[22]. Evans and Mort attempted to draw a distinction between the fluid dynamic mechanism causing short bubble breakdown suggested by Owen and Klanfer[3] and that suggested by Wallis[7], and to do this they estimated the separation conditions of the laminar boundary layer on a number of aerofoils whose force tests indicated sudden stalls (i.e. leading-edge or thin-aerofoil stalls). Two arbitrary requirements were placed upon the lift variation at the stall in order to define a sudden stall.

(a) the lift loss at the stall was to be greater than 0·1 in terms of C_L;

(b) the two data points defining the stall should indicate a slope $\Delta C_L/\Delta\alpha$ greater than 0·1 per degree.

It is quite obvious that the stall of this aerofoil at $R_c = 1{\cdot}78 \times 10^6$ satisfies both these requirements and yet is also manifestly a trailing-edge stall. For this reason, if for no other, the conclusions drawn by Evans and Mort[22] from their analysis cannot be accepted without reservations.

Figs. 29 and 30 show that it is perfectly possible (on this aerofoil at least) to have a stable short bubble

flow near the leading edge co-existing with a downstream turbulent boundary layer which separates before the trailing edge. Fig. 29 shows that, at $R_c = 1{\cdot}33 \times 10^6$, the separation point has moved forward as far as $0{\cdot}16\,c$ at $\alpha = 18°$ before the leading-edge flow finally breaks down, the initial stall having occurred at $\alpha = 13°{\cdot}5$. From Fig. 32, at $R_c = 1{\cdot}78 \times 10^6$, it can be seen that the incidence range over which this occurs is 7° ($\alpha = 14°$ to $\alpha = 21°$).

The form-drag curves at the different Reynolds numbers are compared in Fig. 33. An interesting feature of this figure is the unusual 'kink' which occurs in the curves for the two highest Reynolds numbers at round $C_L = 0{\cdot}8$ ($\alpha \simeq 8°$). From the chordwise pressure distributions in Fig. 30, and also from Fig. 29, it can be seen that the position of this 'kink' correlates quite well with the first occurrence of a noticeable short bubble near the leading edge, and thus with rapidly changing initial conditions of the turbulent boundary layer on the upper surface. It may be significant that this 'kink' seems to have disappeared by $R_c = 0{\cdot}91 \times 10^6$ and this may be connected with the increasing tendency towards a leading-edge stall pattern as the Reynolds number is reduced.

The variation of pitching moment about the quarter chord point up to and beyond the stall through the Reynolds number range is shown in Fig. 34. From Fig. 30 it can be seen that the strong nose down break in the pitching moment at the stall is due to the dual effects of the boundary-layer separation near the trailing edge. Firstly the suctions underneath the separated region are slightly increased and secondly the increased displacement surface of the separated region causes the suctions at the leading edge to be reduced, both effects contributing to a nose-down pitching moment. Also from Fig. 30 it can be seen ($\alpha = 19°$) that when the leading-edge flow breaks down the leading-edge suctions entirely collapse and there is a further small increase in the suction levels near the trailing edge, thus adding a further nose down contribution to the pitching moment.

6.2. *Analysis of Pressure Distributions*

The results of the three methods of pressure distribution analysis (Section 4.2) are plotted in carpet form in Figs. 37 to 41 inclusive. Fig. 37 shows the variation of the single parameter α_b/α used in Method 1, with incidence and Reynolds number. It will be seen that the value of this parameter is almost constant at about 0·88 over the first 5° of incidence. This behaviour is different to that found by Brebner and Bagley[19] on a 10 per cent t/c RAE 10 1 section where the value of α_b/α fell linearly from 0·92 at $\alpha = 0°$ to 0·88 at $\alpha = 5°$. If the pressure distributions on the two aerofoil sections at $\alpha = 0°$ are compared, it is found that the pressure distributions aft of 30 per cent chord are very similar, the pressure rise to the trailing edge being linear in each case; however forward of 30 per cent chord the pressure distribution on the RAE 101 is almost flat to a point close to the leading edge, whereas that on the RAE 100 continues the linear distribution forward to a point close to the leading edge. Since the measured transition positions are similar in each case, it seems almost certain from this that the present RAE 100 section has a thicker boundary layer at the trailing edge which would adequately explain the lower value of α_b/α. As the incidence is raised the peak suction on the RAE 101 section increases faster than on the present section because of its smaller nose radius, so that the boundary layer would be expected to thicken more rapidly with increase of incidence; this would explain the linear decrease of α_b/α on the RAE 101 section compared to the nearly constant value obtained in the present tests. From the figures presented above it would appear that conditions on the two aerofoils become very similar at about five degrees of incidence.

It is interesting to consider at this point, what kind of behaviour might be expected from the parameters (α_b/α) and n as either $\alpha \to 0$ or $R_c \to \infty$. Since the aerofoil section plus its boundary layer at $\alpha = 0°$ is still a symmetrical aerofoil, just slightly thicker, it might be argued that the initial lift-curve slope would be very close to the potential flow value (i.e. α_b/α close to unity). On the other hand the boundary layer must become asymmetric as soon as the aerofoil develops any lift and this would tend to depress the value of the lift-curve slope. Ultimately, the behaviour of α_b/α as $\alpha \to 0$ must depend on the balance between the rate at which boundary-layer asymmetry grows with incidence and the lift-curve slope in potential flow. As on neither the present aerofoil nor the RAE 101 of Brebner and Bagley[19], does there appear

to be any tendency for (α_b/α) to tend to unity as $\alpha \to 0$, it must be assumed that the boundary-layer asymmetry is a rather stronger function of incidence than the lift. Once the additional parameter 'n' is admitted to the characterisation of the boundary-layer effect it could be argued, in a similar way to before, that (α_b/α) should tend to unity and n to $\frac{1}{2}$ as $\alpha \to 0$, however, if, as seems to be the case from above, the boundary-layer asymmetry is dominant then the observed behaviour may well be different to this. With increasing Reynolds number, at any incidence, it is to be expected that the displacement effect of the boundary layer will diminish, so that there should be a well defined tendency for α_b/α to move towards unity and for n to move towards 0·5.

If we look now at the results from Method 2 shown in Figs. 38 and 39 it can be seen that as $\alpha \to 0$, n appears to tend to 0·5 (apart from the somewhat different behaviour at the highest Reynolds number) but that α_b/α still appears to tend to a value of about 0·88 as in the previous method. With increasing Reynolds number it can be seen that there is a distinct trend of n towards a value of 0·5 but the values of α_b/α still appear to tend to a value near 0·9. The results of Method 3, given in Figs. 40 and 41, show a very different behaviour to those of the previous method as $\alpha \to 0$, as, in this case, α_b/α tends to unity and n tends to 0·5. With increasing Reynolds number the variation of n is strongly towards 0·5 but, at least at the higher incidences, α_b/α seems to tend to a figure significantly less than unity. It will be seen that, although the shape of these Method 3 carpets is broadly similar to those of Method 2, their vertical extent is considerably greater, indicating, as was anticipated in Section 4.2.4, that the overall forces derived from the Method 3 values of α_b/α and n will differ from those obtained experimentally. The extent of these differences is shown in Figs. 42 and 43, from which it will be seen that the normal force calculated in this way is higher than that realised experimentally (although not very significantly between $\alpha = 4°$ and $\alpha = 11°$) whilst the centre of pressure is slightly aft of that obtained experimentally over most of the pre-stall range but moves forward more rapidly as the stall is approached.

However, the main point of interest centres around the representation of the measured pressure distribution, so that we need not be too concerned about discrepancies in the overall forces provided they are not too large, and, in the main, these predictions are reasonable. The predicted chordwise loadings from the three methods are compared with the measured loadings for two sample incidences in Figs. 44 and 45. The comparisons are conducted on a $\Delta C_p \sqrt{x/c}$ against $\sqrt{x/c}$ basis since this expands the critical leading edge region; the first incidence ($\alpha = 6°$ $R_c = 1{\cdot}33 \times 10^6$) is a case where the overall characteristics are reasonably well predicted, the second ($\alpha = 13°$ $R_c = 1{\cdot}33 \times 10^6$) is a case where the prediction of the overall characteristics is rather marginal. Nevertheless it will be seen that the load representations from Method 3 are superior in both cases at least between $0{\cdot}30 < \sqrt{x/c} < 1{\cdot}0$, i.e. over the rear 90 per cent of the chord. Over the forward 10 per cent of the chord there seems to be little to choose between Methods 2 and 3; the reduced incidence method does not give a very good representation in either case as might be expected. Finally in order to show how the pressure distributions on the upper and lower surfaces are represented, three incidences, at a lower Reynolds number, are plotted in Figs. 46 and 47. It will be seen that apart from the peak suction value and part of the lower-surface distribution, the representation is very reasonable. It would appear therefore that the two parameter methods of representing the boundary-layer effect upon the pressure distribution are both superior to the single parameter method, and, although Method 3 is likely to give a superior representation to Method 2, the values obtained from it may imply overall characteristics significantly different to those measured. Furthermore it remains to be seen whether the loadings obtained from other aerofoil sections will fall so easily into the simple linear form of Method 3.

Nevertheless the correspondence between the measured pressure distributions and those derived from either Method 2 or Method 3 is sufficiently good on this aerofoil section, in the two-dimensional case, to suggest that the two parameters involved provide a convenient first-order graphical indication of the effect of the boundary layer upon the pressure distribution, and, therefore, that they could be valuable tools with which to analyse the results from the swept wing.

If we accept the above suggestion then it is instructive to study Figs. 38 to 41 in order to see what overall changes take place in the pressure distribution with variation of incidence and Reynolds number. Since the 'n' values in Figs. 39 and 41 are all greater than 0·5, the effective camber on the section is negative,

which is as would be expected. Thus the camber effect of the boundary layer gives rise to higher suctions near the leading edge, at a given normal-force coefficient, than would be realised in inviscid flow. This can be seen in Figs. 44 and 45 by comparing the experimental loading with that obtained from the reduced incidence method. It also implies a normal force higher than the potential flow value at the same incidence. In method. It also implies a normal force higher than the potential flow value at the same incidence. In consequence, the associated incidence reduction required to recover the observed normal force, is greater than when the boundary-layer effect is regarded solely as a reduction of incidence, as can be seen by comparing Fig. 37 with Figs. 38 and 40. However this camber induced by the boundary layer can be seen to be relatively small up to an incidence of about 9°, but from then on it increases rapidly, resulting in the leading-edge loading becoming more and more severe so that there is an increasing tendency towards a leading-edge stall. On this section not only does the camber increase at a significant rate with increase of incidence, but it also increases rapidly with a reduction in Reynolds number, (if we take the results from Method 3) thus showing that the increased tendency towards leading-edge stalling results not only from the reaction of the short bubble flow to a reduction of the Reynolds number, but also from an increasingly severe pressure distribution brought about by the boundary-layer displacement surface over the remainder of the aerofoil.

7. *Conclusions.*

The 12·2 per cent t/c RAE 100 aerofoil section tested appears to have the characteristics desired for the high-lift swept-wing tests. It was found that the section has a trailing-edge stall pattern at chordwise Reynolds numbers greater than about $0{\cdot}60 \times 10^6$. Below this value, a leading-edge, or possibly a mixed leading/trailing-edge stall pattern is induced. The chordwise Reynolds number at which this change takes place appears to be well predicted by laminar boundary-layer calculations[4] and the Owen/Klanfer criterion[3].

Even in the trailing-edge stall regime (i.e. above $R_c = 0{\cdot}60 \times 10^6$), the variation of $C_{L\max}$ with Reynolds number is fairly rapid, whilst below this figure the indications are that the variation is even more rapid. At the highest test Reynolds number ($R_c = 1{\cdot}78 \times 10^6$) a $C_{L\max}$ of 1·37 was observed.

Analysis of the overall forces and moments and of the loading distributions suggests that a fair representation of the pressure distribution in viscous flow can be obtained by altering the effective incidence (α_b/α) and the exponent of the chordwise loading $((1-x)/x)^n$. This representation was reasonable over the rear 90 per cent of the chord, but not so good over the front 10 per cent.

LIST OF SYMBOLS

a	Lift-curve slope $(\partial C_L/\partial\alpha)$
B, C	Distances of pressure holes from the horizontal centreline of the tunnel
c	Aerofoil chord in two-dimensional flow
$\bar{c}$	Aerofoil chord in the stream direction when the wing is swept
C_p	Pressure coefficient $(p-p_0/\frac{1}{2}\rho\, U_0^2)$
C_L	Lift coefficient (lift/unit span $\div \frac{1}{2}\rho\, U_0^2\, c$)
C_D	Drag coefficient (drag/unit span $\div \frac{1}{2}\rho\, U_0^2\, c$)
C_m	Pitching-moment coefficient (pitching moment/unit span $\div \frac{1}{2}\rho\, U_0^2\, c^2$)
C_N	Normal-force coefficient (positive in the lift sense)
C_T	Axial-force coefficient (positive in the drag sense)
ΔC_p	Net non-dimensional pressure difference across the aerofoil section at a fixed value of x
ΔC_N	Increment in normal-force coefficient due to camber in the airflow
ΔC_T	Increment in axial-force coefficient due to camber in the airflow
ΔC_m	Increment in pitching-moment coefficient due to camber in the airflow
k	$R\delta_s^*/\sqrt{R_c}$
p	Local pressure
p_0	Free-stream static pressure
r	Aerofoil nose radius
R_c	$\dfrac{U_0\, c}{\nu}$
$R\delta_s^*$	$\dfrac{U_0\, \delta_s^*}{\nu}$
U_0	Free-stream velocity
S_1, S_2, S_3	Standard integrals involved in the calculation of aerofoil pressure distributions by the Weber[20] method
x	Distance chordwise from the leading edge (positive rearwards)
X	Distance of the point of action of the normal force from the leading edge
z	Distance normal to the aerofoil chord (positive upwards)
Z	Distance of the point of action of the axial force from the chord line
α	Angle of incidence
α_0	Angle of incidence for zero lift
$\Delta\alpha$	Error in setting incidence datum, or error in set incidence
$\Delta\alpha^*$	Angle of incidence for zero local ΔC_p
δ_s^*	Displacement thickness of laminar boundary layer at separation
ρ	Fluid density
ν	Fluid kinematic viscosity

Suffixes

x	Moment due to pressures acting on the projection of the aerofoil surface in the chordal plane, measured about the leading edge
z	Moment due to pressures acting on the projection of the aerofoil surface in a plane normal to the chord
$c/4$	Moment evaluated about the $\frac{1}{4}$ chord point
b	Force, moment, incidence or pressure distribution including the effect of the boundary layer in a calculation assuming potential flow
c	Uncorrected coefficients (as measured in the tunnel)
$+$	Force, moment or incidence taken at a positive value of α (Appendix A only)
$-$	Force, moment or incidence taken at a negative value of α (Appendix A only)

Superscripts

$\hat{}$	Measured coefficients and incidence corrected for airflow camber and swirl, blockage and constraint, and incidence datum error
$-$	Smoothed values of force and moment coefficients or incidence corrected for blockage and constraint

REFERENCES

No.	Author(s)	Title, etc.
1	B. Thwaites (Ed.)	*Incompressible aerodynamics.* (A.R.C. Fluid Motion Memoirs) Oxford University Press (1960).
2	D. E. Gault	A correlation of low speed aerofoil section stalling characteristics with Reynolds number and aerofoil geometry. NACA Technical Note 3963 (1957).
3	P. R. Owen and L. Klanfer	On the laminar boundary layer separation from the leading edge of a thin aerofoil. A.R.C., C.P. 220 (1953).
4	N. Curle and S. W. Skan	Calculated leading-edge laminar separations from some R.A.E. aerofoils. A.R.C., C.P. 504 (1959).
5	L. F. Crabtree	Effects of leading edge separation. Thin wings in two-dimensional incompressible flow. *Journal Aero Sci*, Vol. 24, No. 8, pp. 597–604 (1957).
6	A. E. von Doenl.off	A preliminary investigation of boundary-layer transition along a flat plate with an adverse pressure gradient. NACA Technical Note 639 (A.R.C. 3655), (1938).
7	R. A. Wallis and N. Ruglen	Note on the breakdown of the laminar separation bubble on the nose of a thin wing. A.R.C. 19685 (1957).
8	I. McGregor	Regions of localised boundary layer separation and their role in the nose stalling of thin aerofoils. Ph.D. Thesis, London University (1954).
9	M. Gaster	The structure and behaviour of laminar separation bubbles. A.R.C., R. & M. 3595 (1966).
10	D. S. Woodward	An investigation of the parameters controlling the behaviour of laminar separation bubbles. R.A.E. Technical Memo Aero 1003 (A.R.C. 29446), (1967).
11	A. D. Young and H. Horton	Some results of investigations of separation bubbles. AGARD C.P. No. 4, Separated Flows, Pt. 2, May 1966.
12	H. P. Horton	A semi-empirical theory for the growth and bursting of laminar separation bubbles. A.R.C., C.P. 1073 (1967).
13	J. W. Bacon, W. Pfenniger and C. R. Moore	Influence of acoustical disturbances on the behaviour of a swept laminar suction wing. Northrop Corp. Norair Div. Report NOR-62-124 (BLC-141), (1962).

14 A. D. Young .. .. .. Note on a method of measuring profile drag by means of an integrating comb.
A.R.C., R. & M. 2257 (1938).

15 R. C. Pankhurst and D. W. Holder .. .. *Wind tunnel technique.*
PITMAN.

16 The Cambridge University Aeronautics Laboratory. .. The measurement of profile drag by the pitot-traverse method.
A.R.C., R. & M. 1688 (1936).

17 D. Küchemann .. .. A simple method for calculating the span- and chordwise loadings on straight and swept wings of any given aspect ratio at subsonic speeds.
A.R.C., R. & M. 2935 (1952).

18 Method for predicting the pressure distribution on swept wings with subsonic attached flow.
Roy. Aero. Soc. Transonic Data Memorandum 6312.

19 G. G. Brebner and J. Bagley .. .. Pressure and boundary layer measurements on a two-dimensional wing at low speed.
A.R.C., R. & M. 2886 (1952).

20 J. Weber .. .. .. The calculation of the pressure distribution over the surface of two-dimensional and swept wings with symmetrical aerofoil sections.
A.R.C., R. & M. 2918 (1953).

21 L. R. Wootton .. .. .. The effect of compressibility on the maximum lift coefficient of aerofoils at subsonic speeds.
Journal Roy. Aero. Soc., pp. 468–478, July, 1967.

22 W. T. Evans and K. W. Mort .. .. Analysis of computed flow parameters for a set of sudden stalls in low speed two-dimensional flow.
NASA Technical Note D-85 (1959).

23 E. C. Maskell .. .. .. A theory of the blockage effects on bluff bodies and stalled wings in a closed wind tunnel.
A.R.C., R. & M. 3400 (1963).

24 R. A. Mendelsohn and J. F. Polhamus .. Effect of the tunnel-wall boundary layer on test results of a wing protruding from the tunnel wall.
NACA Technical Note 1244 (1947).

25 I. Tani .. .. Low speed flows involving bubble separations.
Progress in Aeronautical Sciences, Vol. 5, Pergamon Press.

APPENDIX A

The Method for Correcting Measured Coefficients for Camber in the Tunnel Flow.

A.1. *Derivation of Formulae.*

Küchemann[17] quotes the following equation connecting the normal and axial forces on a cambered aerofoil section.

$$C_T = -\frac{C_N^2}{a} - C_N \alpha_0 \tag{A.1}$$

where a = lift curve slope

α = wing incidence for zero lift.

This equation may be derived in the following way. Firstly, consider any symmetrical aerofoil set at an angle α to the free stream direction; in which case we may write

$$C_L = C_N \cos\alpha - C_T \sin\alpha \tag{A.2}$$

$$C_D = C_T \cos\alpha + C_N \sin\alpha\,. \tag{A.3}$$

For small values of α, these become

$$C_L = C_N - C_T \alpha \tag{A.4}$$

$$C_D = C_T + C_N \alpha \tag{A.5}$$

furthermore, in this condition it can be seen that the pressure drag is very small, (*see* Figs. 21 to 24), so that we may assume, as in inviscid flow

$$C_D \equiv 0\,.$$

Therefore from equation (A.5)

$$\alpha = -\frac{C_T}{C_N}\,. \tag{A.6}$$

Inserting equation (A.6) in equation (A.4) leads to

$$\frac{C_L}{\alpha} = a = -\frac{C_N}{C_T/C_N} - C_T$$

i.e.

$$C_T = -\frac{C_N^2}{a} - \frac{C_T^2}{a} = -\frac{C_N^2}{a} \tag{A.7}$$

to the first order on thin aerofoil sections.

However for a cambered aerofoil section

$$a = \frac{C_L}{\alpha - \alpha_0}$$

so that equation (A.4) may be written

$$\frac{C_L}{\alpha-\alpha_0} = a = \frac{C_N}{\alpha-\alpha_0} - C_T \left\{ \frac{\alpha}{\alpha-\alpha_0} \right\}$$

which, upon inserting equation (A.6) again, leads to

$$a = -\frac{C_N}{\left[\frac{C_T}{C_N}+\alpha_0\right]} - \frac{C_T (C_T/C_N)}{\left[\frac{C_T}{C_N}+\alpha_0\right]}$$

i.e.

$$C_T = -\frac{C_N^2}{a} - C_N \alpha_0 - \frac{C_T^2}{a}$$

$$\simeq -\frac{C_N^2}{a} - C_N \alpha_0 \qquad \text{(A.8)}$$

to the first order on thin aerofoil sections.

If we assume that

$$\Delta C_N \simeq \Delta C_L$$

where ΔC_N and ΔC_L are the increments in the normal force and lift coefficients respectively, that occur at $\alpha = 0°$ due to the addition of camber, then we may write

$$\alpha_0 = -\frac{\Delta C_L}{a} \simeq -\frac{\Delta C_N}{a}. \qquad \text{(A.9)}$$

Inserting this into equation (A.8) leads to

$$C_T = -\frac{C_N^2}{a} + \frac{C_N \Delta C_N}{a}. \qquad \text{(A.10)}$$

A.2. *Method of Applying Corrections.*

We have established the form of the $C_N \sim C_T$ relationships for a symmetrical aerofoil and for a cambered aerofoil; these relationships may now be used to estimate the characteristics of the symmetrical aerofoil in a symmetrical airflow from the experimental measurements which were obtained in a cambered airflow. Using the suffix c to denote coefficients prior to correction for camber and the superfix ^ to denote coefficients after correction as in Section 5, we may write

$$\left.\begin{aligned} \hat{C}_N &= C_{N_c} - \Delta C_N \\ \hat{C}_T &= C_{T_c} - \Delta C_T \\ \hat{C}_m &= C_{m_c} - \Delta C_{m_x} - \Delta C_{m_z} \end{aligned}\right\} \qquad \text{(A.11)}$$

where ΔC_N and ΔC_{m_x} are respectively the increments in normal force and pitching moment at $\alpha = 0°$ due to the addition of camber and are assumed to be constants over the incidence range; ΔC_T and ΔC_{m_z} are the corresponding increments in axial force and pitching moment except that it will be shown that these are functions of the normal force and so vary through the incidence range.

Using equations (A.7) and (A.10) we may write

$$\hat{C}_T = -\frac{\hat{C}_N^2}{a}$$

$$C_{T_c} = -\frac{C_{N_c}^2}{a} + \frac{\Delta C_N C_{N_c}}{a}$$

where we make the plausible assumption that the value of the lift curve slope 'a' is not altered by the addition of camber.

Then

$$C_{T_c} - \hat{C}_T = \Delta C_T = -\frac{C_{N_c}^2}{a} + \frac{\Delta C_N C_{N_c}}{a} + \frac{(C_{N_c} - \Delta C_N)^2}{a}$$

therefore

$$\Delta C_T = -\frac{\Delta C_N C_{N_c}}{a} + \frac{\Delta C_N^2}{a}$$

$$= -\frac{\Delta C_N C_{N_c}}{a} \qquad \text{(A.12)}$$

to the first order.

It should be noted in passing that we can make ΔC_T equal to zero (to the first order) by writing

$$\hat{C}_N = C_{N_c} - \frac{\Delta C_N}{2}.$$

This indicates that an apparent collapse of the $C_N \sim C_T$ data at positive and negative incidences can be achieved by making a single correction to the normal force, of magnitude $\Delta C_N/2$. Although this may seem an obscure point to make, nevertheless, when working solely from experimental data, there is a strong tendency to feel that an adequate correction has been made once a good collapse of such basic data as normal and axial force, has been obtained, which, in this case, would be wholly unjustified.

A.3. *Method of Calculating the Magnitude of the Corrections.*

Of all the main parameters with which we are concerned, only the incidence α, is dependent for its numerical value upon some arbitrary datum, therefore, in attempting to evaluate the increments in C_N, C_T etc., due to camber in the flow, we shall be aiming to use formulae which are independent of the incidence. Thus, although the lift curve slope 'a' may be expected to be a function of α, in order to estimate the normal force increment ΔC_N we assume that it is only a slowly varying function of $|\alpha|$, so that we may write

$$C_{T_{c+}} = -\frac{C_{N_{c+}}^2}{a} + \frac{\Delta C_N C_{N_{c+}}}{a}$$

$$C_{T_{c-}} = -\frac{C_{N_{c-}}^2}{a} + \frac{\Delta C_N C_{N_{c-}}}{a}$$

where the subscripts + and − refer to a positive and negative incidence respectively, having approximately the same value of $|\alpha|$. By eliminating 'a' between the two equations we obtain

$$\Delta C_N = \frac{C_{T_{c+}} C_{N_{c-}}^2 - C_{T_{c-}} C_{N_{c+}}^2}{C_{N_{c-}} C_{T_{c+}} - C_{N_{c+}} C_{T_{c-}}}. \tag{A.13}$$

Using this expression, values of ΔC_N were calculated for each pair of positive and negative incidence values on the three highest Reynolds number runs; the average value and the standard deviation for each run are shown plotted against R_c in Fig. 48. Since most of this normal-force increment is due to camber in the airflow, and this could conceivably vary with windspeed in an unusual fashion, it is possible that ΔC_N is a non-monotonic function of R_c, as is suggested by the average values in Fig. 48. However, bearing in mind the relatively large values of standard deviation also shown in Fig. 48, it was felt that the only justifiable course was to take a constant value for ΔC_N over the whole Reynolds number range. The average constant value used was

$$\Delta C_N = 0{\cdot}016\,. \tag{A.14}$$

Having obtained a value for ΔC_N, ΔC_T for each experimental point may be estimated using the effective value of 'a' implied by the experimental values of C_N and C_T, namely

$$a = -\frac{C_{N_c}^2 + \Delta C_N C_{N_c}}{C_{T_c}}$$

so that

$$\Delta C_T = \frac{\Delta C_N C_{N_c} C_{T_c}}{C_{N_c}^2 - \Delta C_N C_{N_c}}$$

$$= \frac{\Delta C_N C_{T_c}}{\hat{C}_N}. \tag{A.15}$$

In order to evaluate the chordwise pitching moment increment ΔC_{m_x}, we again require an expression that is independent of α, and this may be obtained by writing

$$\hat{C}_{m_x} = \hat{C}_N X = (C_{N_c} - \Delta C_N) X \tag{A.16}$$

where X is the centre of pressure position on the symmetrical aerofoil/flow combination, and, in a similar way to before, is assumed to be only a slowly varying function of $|\alpha|$.

Thus we may write (dropping the suffix 'x')

$$C_{m_{c+}} = (C_{N_{c+}} - \Delta C_N) X + \Delta C_{m_x}$$

$$C_{m_{c-}} = (C_{N_{c-}} - \Delta C_N) X + \Delta C_{m_x}$$

where the subscripts + and − have the same significance as before. Then eliminating X leads to

$$\Delta C_{m_x} = \frac{C_{m_{c+}} C_{N_{c-}} - C_{m_{c-}} C_{N_{c+}} - \Delta C_N (C_{m_{c+}} - C_{m_{c-}})}{C_{N_{c-}} - C_{N_{c+}}}$$

$$= \frac{C_{m_{c+}} \hat{C}_{N-} - C_{m_{c-}} \hat{C}_{N+}}{C_{N_{c-}} - C_{N_{c+}}}. \tag{A.17}$$

As for ΔC_N, ΔC_{m_x} was evaluated from the above equation for each pair of positive and negative incidences in the three highest Reynolds number runs and, from these figures, the average value and the standard deviation were calculated and are shown plotted in Fig. 49. In contrast to the figures for ΔC_N, these values show a fairly strong monotonic trend with Reynolds number, indicating that the flow conditions in the tunnel do depend on windspeed. In this case it was felt that the trend with Reynolds number was sufficiently strong for the corrections to take account of it, so the linear variation shown in Fig. 49 was used resulting in the following values of ΔC_{m_x}

R_c	ΔC_{m_x}
$0{\cdot}55 \times 10^6$	$-0{\cdot}00045$
$0{\cdot}66 \times 10^6$	$-0{\cdot}00080$
$0{\cdot}91 \times 10^6$	$-0{\cdot}00155$
$1{\cdot}33 \times 10^6$	$-0{\cdot}00280$
$1{\cdot}78 \times 10^6$	$-0{\cdot}00415$

(A.18)

The same method cannot be used to estimate the correction to the axial force component of the pitching moment, since the point of action of the axial force Z is a rapidly varying function of C_T (*see* Fig. 12), however, experimentally C_m appears to be very nearly proportional to the normal force C_{N_c} (*see* Fig. 51) so C_{m_z} was corrected simply by multiplying by the ratio $(\hat{C}_N/C_{N_c})$.

The original incidence datum ($\alpha = 0°$) was established by changing the wing incidence until there was zero pressure difference across a chordwise station close to the leading edge. In view of the camber which has been shown to be present in the flow, this is unlikely to be the correct datum for the data once it has been corrected for the flow camber. Therefore it is necessary also to calculate a correction to the incidence datum, which can be done by writing

$$\hat{C}_N = a(\alpha - \Delta\alpha)$$

so that

$$\hat{C}_{N_+} = a\alpha_+ - a\Delta\alpha$$

$$\hat{C}_{N-} = a\alpha_- - a\Delta\alpha$$

where the nomenclature is as before. In this way

$$\Delta\alpha = \frac{\hat{C}_{N-}\alpha_+ - \hat{C}_{N_+}\alpha_-}{\hat{C}_{N-} - \hat{C}_{N_+}}. \tag{A.19}$$

In the same way as before the average value and the standard deviation were calculated for each of the three highest Reynolds number runs, and are plotted in Fig. 50. As with ΔC_N there does not appear to be any well defined trend with Reynolds number, and the assumption of a constant value over the Reynolds number range would appear to be in order.

Thus the correction of the measured coefficients for flow camber may be summarised as follows

$$\left.\begin{aligned} \hat{C}_N &= C_{N_c} - 0{\cdot}016 \\ \hat{\alpha} &= \alpha_c - 0{\cdot}17 \text{ degrees} \\ \hat{C}_T &= C_{T_c} - \frac{0{\cdot}016\, C_{T_c}}{\hat{C}_N} \\ \hat{C}_m &= C_{m_{xc}} - \Delta C_m(R_c) + \frac{C_{m_{zc}} \hat{C}_N}{C_{N_c}}. \end{aligned}\right\} \tag{A.20}$$

The values derived from the above formulae were then treated as the usual tunnel uncorrected results and were further corrected for tunnel constraint and blockage and are presented in Table 4.

It is interesting to compare the figures for ΔC_N and ΔC_{m_x} obtained from this analysis with those obtained from a direct integration of the camber shown in Fig. 7. The integration of Fig. 7 gives

$$\Delta C_N = 0{\cdot}0090$$

$$\Delta C_{m_x} = -0{\cdot}0037$$

whilst at the same Reynolds number the analysis gives

$$\Delta C_N = 0{\cdot}0130$$

$$\Delta C_{m_x} = -0{\cdot}0030$$

which, considering the accuracies involved, would seem to be a reasonable correlation supporting the hypothesis that camber in the model/airflow combination is responsible for the differences shown in Fig. 10.

APPENDIX B

Analysis of the Accuracies Achieved.

The scatter on the values of X plotted in Fig. 13 provides the most convenient point at which to start an analysis of accuracies. The value of X is obtained as the ratio C_{m_x}/C_N, both of which parameters are evaluated from a single traverse of the integrator round the same figure—the plot of $C_p\sqrt{x/c} \sim \sqrt{x/c}$ —by compounding the readings of the three integrating wheels on the Amsler integrator. Therefore it is clear that the values of X obtained will not be affected by systematic errors, such as those in the incidence setting, reading of the tunnel reference pressures, graph plotter scaling and/or graph paper shrinkage; so that such scatter as does occur should be primarily due to random errors in the reading of individual pressures, drawing the mean lines through the plotted points, and tracing the figure with the point of the integrator.

If we now suppose that 2δ is the random error in the evaluation of an area, 3δ the error in the evaluation of a first moment of area, and 4δ that on the evaluation of a second moment of area, and if further we suppose that e is half the width of the scatter band on X, then we may write

$$\frac{C_{m_x}(1\pm 4\delta)}{C_N(1\pm 2\delta)} = X(1\pm e).$$

By expanding and ignoring terms in δ^2 and higher powers, we obtain finally

$$\delta = \pm\frac{e}{6}.$$

Inspection of the camber corrected values of X in Fig. 13 shows that the maximum half width of the scatter band is approximately 0·005 in an X value of 0·235 giving

$$e = \pm 0{\cdot}0210$$

and

$$\delta = \pm 0{\cdot}0035.$$

In this way, the estimated errors on normal force and pitching moment become

$$C_N \quad \pm 0{\cdot}7\%$$

$$C_{m_x} \quad \pm 1{\cdot}4\%.$$

The errors in the evaluation of C_T and C_{m_z} are almost impossible to assess as the final results are obtained as the algebraic sum of the positive and negative regions, although the above assessment might be expected to apply to the sum of the moduli of the various component regions.

Having obtained an estimate of the errors involved in the evaluation of C_N, we may now proceed to estimate the likely error in incidence setting, noting first that this error is more likely to be of a certain magnitude than a percentage of the set incidence. If again e is used to represent the half width of the scatter band, we may write

$$\frac{C_N(1\pm 0{\cdot}007)}{\alpha\pm\Delta\alpha} = \left(\frac{C_N}{\alpha}\right)(1\pm e)$$

therefore

$$\frac{\Delta\alpha}{\alpha} = \pm(e-0{\cdot}007)$$

ignoring squares and products of errors.

Inspection of Fig. 12 shows that the scatter band decreases in width as the incidence is increased, thus reinforcing the suggestion that $\Delta\alpha$ is an error of given magnitude rather than a percentage error, however this makes it difficult to estimate the value of e. By concentrating attention on the lower incidences where the error will show up most, a tentative figure of 0·0025 in a C_N/α value of 0·105 at an average incidence of 2 degrees was taken as being representative; using these values gives

$$\Delta\alpha = \pm 0{\cdot}034 \text{ degrees}.$$

The *mean* error values quoted by Brebner and Bagley[19] in a similar investigation were

$$C_N \quad \pm 0{\cdot}3\%$$

$$\alpha \quad \pm 0{\cdot}01 \text{ degrees}.$$

These values are somewhat better than those obtained here even allowing for the fact that the present values are near to the maximum observed.

It is instructive to proceed a little further and evaluate the maximum form-drag increment implied by the errors evaluated above. Now

$$C_D = C_N \cos\alpha + C_T \sin\alpha$$

therefore

$$(C_D \pm \Delta C_D) = C_N (1 \pm 0{\cdot}007)(\sin\alpha \pm \Delta\alpha) + C_T (1 \pm 0{\cdot}007)\cos\alpha$$

assuming small α and the same errors on C_T as on C_N.

Therefore

$$C_D \pm \Delta C_D = C_N \sin\alpha \pm 0{\cdot}007\, C_N \sin\alpha \pm C_N \Delta\alpha + C_T \cos\alpha \pm 0{\cdot}007\, C_T \cos\alpha$$

neglecting products of errors.

Assuming small α again, this leads to

$$\Delta C_D = \pm(0{\cdot}007\, C_N \alpha + C_N \Delta\alpha + 0{\cdot}007\, C_T).$$

Thus for a typical case

$$\alpha = 0{\cdot}175 \text{ radian}$$

$$\left.\begin{aligned} \Delta\alpha &= 0{\cdot}006 \text{ radian} \\ C_N &= 1{\cdot}032 \\ C_T &= -0{\cdot}165 \end{aligned}\right\} \quad R_c = 0{\cdot}91 \times 10^6 \text{ (Table 5)}.$$

$$\Delta C_D = \pm\{0{\cdot}00126 + 0{\cdot}00062 + 0{\cdot}00116\}$$

$$= \pm 0{\cdot}00304$$

which, as can be seen from Fig. 23, represents an extremely large possible scatter band around the lines drawn, almost large enough to account for the crossover between the form and profile drag curves if all the errors happened to be combined in one direction for most of the points near the stall. It is interesting to note from the above calculation that the term involving the error due to incidence setting is the smallest of the three, so that to achieve better measurements of the form drag it is necessary to radically improve the accuracy of the integration methods.

APPENDIX C

Method of Obtaining Fully Smoothed Results.

Having applied the corrections for camber to the normal and axial forces, a good collapse of data at positive and negative incidences was obtained as shown in Fig. 11. Then, having drawn mean lines through the $C_N/\alpha \sim \alpha$ relationship (Fig. 12), new values of C_N, $\bar{C}_N$, were generated appropriate to particular values of α; these values of $\bar{C}_N$ were marked on the $C_N \sim C_T$ carpet (Fig. 11) and lines of constant α drawn, giving a double check as to the smoothing of the C_N/α figures; from the $C_N \sim C_T$ curves, knowing the values of $\bar{C}_N$, smoothed values of C_T, $\bar{C}_T$, were obtained. In order to obtain smoothed values of C_m, the chordwise centre of pressure X was plotted against α, and mean lines drawn as in Fig. 13; using the figures from these mean lines and the values of $\bar{C}_N$, smoothed values of $\bar{C}_{m_x}$ were obtained; smoothed values of $\bar{C}_{m_z}$ were obtained by multiplying $\bar{C}_T$ by values of Z read from the mean lines drawn through the $\hat{Z}$ against $\hat{C}_T$ points shown in Fig. 14. Finally smoothed values of the lift coefficient and form drag were calculated from

$$\bar{C}_L = \bar{C}_N \cos \bar{\alpha} - \bar{C}_T \sin \bar{\alpha}$$

$$\bar{C}_D = \bar{C}_T \cos \bar{\alpha} + \bar{C}_N \sin \bar{\alpha}$$

and the smoothed value of pitching moment from

$$\bar{C}_m = \bar{C}_{m_x} + \bar{C}_{m_z}.$$

The same procedure was adopted for smoothing both the post- and the pre-stall figures, although the scatter in the post-stall figures made the relationships poorly defined in some areas.

APPENDIX D

Consideration of the Apparent Anomalies in the Profile and Form-Drag Measurements Observed near the Stall.

When the original surface pressure measurements were made in the No. 2 tunnel, all the attention was focussed on the determination of the stall pattern, and no profile drag measurements were made. Later, it was decided that profile drag measurements were necessary in order to present a complete picture of the sectional characteristics, and so these were measured in the No. 1 tunnel because of availability of the tunnel. When it was found that the measured profile drag near the stall was less than the derived form drag, arrangements were made to repeat the measurements in the No. 2 tunnel in case differences in turbulence level were the cause. The repeat tests in the No. 2 tunnel confirmed the profile-drag values obtained in the No. 1 tunnel as shown in Figs. 21 to 24, and showed that the values obtained were not sensitive to the inclination of the rake nor to the distance behind the aerofoil provided the correction was made for the static pressure at the rake position. However, it must be admitted that this agreement is not conclusive since the condition of the No. 2 tunnel had been radically altered between the time of the two tests by the removal of two screens and other modifications in the return circuit, nevertheless it cannot necessarily be assumed that these changes are primarily responsible since the stalling angles repeated well, and hot wire turbulence measurements do not show an inordinate rise in the turbulence level—from a probable u-fluctuation level of approximately 0·06% to 0·1%.

It is to be expected that the overall skin friction on the section will become very small as the stall is approached, since

(a) the turbulent boundary layer on the upper surface will be close to separation over most of its length and so will have only a small skin friction;

(b) the stagnation point on the lower surface occurs at about 3 per cent of the chord from the leading edge, so the skin friction on the portion of the section between the stagnation point and the nose produces a thrust on the section and the skin friction on this portion will be relatively high, even though the layer is laminar, because of the strong accelerating pressure gradient;

(c) the boundary layer from the stagnation point aft will be laminar over most of its length but the skin friction will be very much less than in the layer discussed under (b) because the pressure gradients are so much less severe.

Because the skin friction *is* likely to be small, some small degree of crossover between the profile and form drag curves might have been expected due to experimental error, but the magnitude of the differences shown in Figs. 21 and 23 is so large and so strongly confirmed by the very different trends of the two curves, that it is hard to see how these discrepancies can be adequately explained away by experimental error even allowing in full for the inaccuracies shown in Appendix B. However in view of the confirmation of the profile-drag measurements it was felt to be necessary also to investigate the derivation of the form drag to see where errors could arise.

Firstly, careful study of the $C_p \sim z/c$ plots showed that there were sufficient pressure points around the suction peak adequately to define the curve, (*see* Fig. 9) so there was no chance that the C_T figures were significantly in error due to the curves being incorrectly drawn. Secondly, having noted that the difference between the profile and form-drag measurements is large at $R_c = 1{\cdot}78 \times 10^6$, non-existent at $R_c = 1{\cdot}33 \times 10^6$, and of moderate magnitude at $R_c = 0{\cdot}91 \times 10^6$, it was noticed that this appeared to correlate with the differences between the overall mean value of ΔC_N and the individual average value of ΔC_N for each run shown in Fig. 48, which led to the consideration of whether the discrepancies could have originated in the correction procedure for the flow camber. However, it will be clear, even if ΔC_N is allowed to vary with Reynolds number, that this will not materially affect the shape of the $C_N \sim C_T$ relationship since ΔC_T depends on ΔC_N. So the only variable remaining which can affect the calculation of the form drag is the incidence, and here there are two possibilities of error.

(i) The magnitude of the incidence correction $\Delta\alpha$ is incorrect.

(ii) Loss in wing lift within the boundary layer on the tunnel walls, due to the lower total head there, is causing a downwash at the centre similar to that experienced on a finite wing.

In the first of these the error in the incidence correction would have to be sufficient to justify a noticeable modification in the $C_N/\alpha \sim \alpha$ relationship, whilst it would be just about possible to justify such a modification on the basis of the present figures, there is still the problem of securing a comparable change in the values of the basic data $\hat{C}_L$ and $\hat{C}_D$.

The second possibility was investigated in detail during the time when the second set of profile-drag measurements was being taken, since recent measurements had shown that the wall boundary layers in the No. 2 tunnel were unusually thick. The results agreed remarkably well with those of Mendelsohn and Polhamus[24] the load falling only about 10 per cent very close to the wall (0·025 c from the wall in a boundary layer thickness of approximately 0·6 c), so that this effect is negligible as is usually the case in two-dimensional tests involving dimensions similar to those of the present test.

Thus there appears to be no simple explanation of why this crossover should exist and so the data has been presented as it stands, but clearly little reliance can be placed upon the form drag values near the stall.

TABLE 1

Distribution of Main Set of Pressure Tappings 12·2% *t/c RAE* 100.

Upper surface		
x/c	*B* (in)	*C* (in)
0·0022	0·50	
0·0060	1·50	
0·0100		0·079
0·0122	0·579	
0·0142	1·079	
0·0164	1·579	
0·0184	2·079	
0·0200	0·079	
0·0264	2·000	
0·0302		0·158
0·0410	0·158	
0·0506		0·237
0·0753	0·237	
0·1004	0·316	
0·1504		0·316
0·2009		0·395
0·2508	0	0
0·3008	0	0
0·3506		0·553
0·4007		0·474
0·4508	0·395	
0·5011		0·395
0·5507	0·316	
0·6009		0·316
0·6504	0·237	
0·7006		0·237
0·7508	0·158	
0·8006		0·158
0·8504	0·079	
0·9004		0·079
0·9504	0	0

Lower surface		
x/c	*B* (in)	*C* (in)
0·0004	0·579	
0·0015	2·000	
0·0033	1·000	
0·0050	1·500	
0·0088	0	
0·0111	0·500	
0·0132	1·079	
0·0154	1·579	
0·0202	2·079	
0·0404	0·079	
0·0504		0·158
0·0603	0·158	
0·1001		0·237
0·1254	0·237	
0·2002		0·316
0·3006	0	0
0·3508		0·553
0·4012		0·474
0·4508	0·395	
0·5008		0·395
0·5508	0·316	
0·6008		0·316
0·6504	0·237	
0·7007		0·237
0·7506	0·158	
0·8007		0·158
0·8506	0·079	
0·9008		0
0·9508		0·079

TABLE 2

Theoretical Mach Number Effects on Lift 12·2% *t/c RAE* 100.

α	$M = 0{\cdot}047$	0·076	0·112	0·150
2	–	0·243	0·244	0·245
4	–	0·485	0·486	0·488
6	–	0·724	0·726	0·729
8	0·956	0·960	0·962	0·964
10	1·190	1·191	1·192	1·194
12	1·414	1·415	1·416	1·417
14	1·632	1·632	1·632	1·631

TABLE 3

Summary of Test Conditions and Measurements Made.

R_c	M	Incidence range	Presssure plotted	Integrated for overall forces	Wake traverse	Wake traverse incidence range	Pressure distributions analysed
$1{\cdot}78 \times 10^6$	0·150	−22° to +22°	Yes	Yes	Yes	+3° to −13°	Yes up to stall
$1{\cdot}33 \times 10^6$	0·112	−19° to +19°	Yes	Yes	Yes	+3° to −13°	Yes up to stall
$0{\cdot}91 \times 10^6$	0·076	−18° to +15°	Yes	Yes	Yes	+3° to −13°	Yes up to stall
$0{\cdot}66 \times 10^6$	0·056	10° to 15° −10° to −15°	Yes	Yes	No	—	Yes up to stall
$0{\cdot}55 \times 10^6$	0·047	10° to 14° −10° to −14°	Yes	Yes	No	—	Yes up to stall

TABLE 4

Fully Corrected Experimental Results 12·2% *t/c RAE* 100.

$R_c = 1{\cdot}78 \times 10^6$ $M = 0{\cdot}15$ Positive incidence

α	C_L	C_D	$C_{m_{c/4}}$	C_N	C_T	C_{m_x}	C_{m_z}	X	Z
0·83	0·090	0·0002	0·0018	0·090	−0·0011	−0·0202	−0·00046	+0·226	0·429
1·84	0·195	0·0008	0·0024	0·195	−0·0055	−0·0457	−0·00092	0·234	0·168
2·84	0·302	0·0007	0·0037	0·301	−0·0143	−0·0705	−0·00144	0·234	0·101
3·85	0·409	0·0014	0·0038	0·408	−0·0260	−0·0966	−0·00202	0·237	0·077
4·85	0·515	0·0034	0·0062	0·514	−0·0402	−0·1203	−0·00244	0·234	0·061
5·86	0·619	0·0039	0·0048	0·616	−0·0592	−0·1469	−0·00302	0·238	0·051
6·86	0·720	0·0070	0·0081	0·716	−0·0790	−0·1680	−0·00348	0·235	0·044
7·86	0·832	0·0096	0·0060	0·826	−0·1044	−0·1974	−0·00396	0·239	0·038
8·87	0·929	0·0106	0·0085	0·920	−0·1328	−0·2179	−0·00443	0·237	0·033
9·87	1·030	0·0131	0·0071	1·017	−0·1637	−0·2433	−0·00497	0·239	0·030
10·87	1·117	0·0165	0·0097	1·100	−0·1946	−0·2612	−0·00525	0·237	0·027
11·88	1·200	0·0204	0·0117	1·179	−0·2271	−0·2785	−0·00577	0·236	0·025
12·88	1·283	0·0295	0·0141	1·258	−0·2574	−0·2956	−0·00602	0·235	0·023
13·88	1·337	0·0370	0·0136	1·307	−0·2849	−0·3081	−0·00636	0·236	0·022
14·87	1·057	0·1026	−0·0631	1·048	−0·1722	−0·3217	−0·00453	0·307	0·026
15·87	1·016	0·1274	−0·0537	1·012	−0·1553	−0·3034	−0·00446	0·300	0·029
16·87	1·000	0·1441	−0·0607	0·998	−0·1523	−0·3070	−0·00432	0·307	0·028
17·87	0·977	0·1605	−0·0611	0·979	−0·1471	−0·3029	−0·00409	0·309	0·028
18·87	0·945	0·1765	−0·0652	0·951	−0·1387	−0·3001	−0·00382	0·316	0·028
19·87	0·881	0·1973	−0·0669	0·896	−0·1140	−0·2885	−0·00329	0·322	0·029
20·87	0·822	0·2017	−0·0663	0·840	−0·1042	−0·2740	−0·00300	0·326	0·029
21·86	0·739	0·2159	−0·0693	0·766	−0·0747	−0·2594	−0·00230	0·339	0·031

TABLE 4—*continued*

Fully Corrected Experimental Results 12·2% *t/c RAE* 100.

$R_c = 1{\cdot}78 \times 10^6$ $M = 0{\cdot}15$ Negative incidence

α	C_L	C_D	$C_{m_{c/4}}$	C_N	C_T	C_{m_x}	C_{m_z}	X	Z
−1·17	−0·124	0·0012	−0·0004	−0·124	−0·0014	0·0301	0·00062	0·242	−0·458
−2·18	−0·231	0·0016	−0·0010	−0·231	−0·0072	0·0560	0·00103	0·242	−0·142
−3·18	−0·337	0·0020	−0·0060	−0·337	−0·0167	0·0769	0·00164	0·228	−0·098
−4·19	−0·445	0·0025	−0·0018	−0·444	−0·0300	0·1073	0·00220	0·242	−0·074
−5·19	−0·549	0·0033	−0·0033	−0·547	−0·0464	0·1313	0·00266	0·240	−0·057
−6·20	−0·655	0·0045	−0·0046	−0·652	−0·0662	0·1559	0·00313	0·239	−0·047
−7·20	−0·754	0·0049	−0·0076	−0·749	−0·0896	0·1765	0·00369	0·236	−0·041
−8·20	−0·863	0·0091	−0·0046	−0·855	−0·1141	0·2060	0·00417	0·241	−0·037
−9·21	−0·950	0·0103	−0·0088	−0·940	−0·1419	0·2224	0·00469	0·237	−0·033
−10·21	−1·053	0·0138	−0·0062	−1·038	−0·1730	0·2493	0·00530	0·240	−0·031
−11·21	−1·134	0·0151	−0·0095	−1·115	−0·2057	0·2647	0·00572	0·237	−0·028
−12·22	−1·221	0·0230	−0·0121	−1·198	−0·2359	0·2824	0·00612	0·236	−0·026
−13·22	−1·296	0·0270	−0·0139	−1·268	−0·2702	0·2977	0·00677	0·235	−0·025
−14·22	−1·374	0·0421	−0·0175	−1·342	−0·2968	0·3126	0·00680	0·233	−0·023
−15·20	−0·831	0·1191	0·0649	−0·833	−0·1030	0·2708	0·00327	0·325	−0·032
−16·20	−0·826	0·1371	0·0723	−0·831	−0·0989	0·2777	0·00324	0·334	−0·033
−17·21	−1·024	0·1487	0·0601	−1·023	−0·1611	0·3123	0·00443	0·305	−0·027
−18·21	−0·977	0·1659	0·0636	−0·980	−0·1479	0·3056	0·00416	0·312	−0·028
−19·21	−0·918	0·1861	0·0691	−0·929	−0·1265	0·2986	0·00360	0·322	−0·028
−20·20	−0·797	0·1985	0·0773	−0·817	−0·0890	0·2795	0·00278	0·342	−0·031
−21·20	−0·793	0·2194	0·0760	−0·818	−0·0822	0·2788	0·00260	0·341	−0·032
−22·20	−0·636	0·3054	0·0920	−0·704	0·0424	0·2675	0·00122	0·380	−0·029

TABLE 4—*continued*

Fully Corrected Experimental Results 12·2% *t/c RAE* 100.

$R_c = 1{\cdot}33 \times 10^6$ $M = 0{\cdot}11$ Positive incidence

α	C_L	C_D	$C_{m_{c/4}}$	C_N	C_T	C_{m_x}	C_{m_z}	X	Z
0·83	0·092	0·0004	0·0001	0·092	−0·0010	−0·0225	−0·00046	0·245	0·464
1·84	0·191	0·0016	0·0025	0·191	−0·0046	−0·0445	−0·00098	0·233	0·216
2·84	0·293	0·0017	−0·0160	0·293	−0·0128	−0·0881	−0·00149	0·300	0·117
3·85	0·403	0·0010	0·0048	0·402	−0·0260	−0·0940	−0·00203	0·234	0·078
4·85	0·500	0·0037	0·0064	0·499	−0·0386	−0·1165	−0·00240	0·233	0·062
5·85	0·606	0·0034	0·0080	0·603	−0·0584	−0·1403	−0·00308	0·233	0·053
6·86	0·714	0·0074	0·0077	0·710	−0·0780	−0·1671	−0·00344	0·235	0·044
7·86	0·833	0·0100	0·0119	0·826	−0·1040	−0·1915	−0·00397	0·232	0·038
8·87	0·918	0·0144	0·0096	0·909	−0·1273	−0·2144	−0·00427	0·236	0·034
9·87	1·015	0·0123	0·0092	1·002	−0·1620	−0·2376	−0·00484	0·237	0·030
10·87	1·105	0·0182	0·0144	1·088	−0·1906	−0·2534	−0·00545	0·233	0·029
11·88	1·168	0·0204	0·0120	1·148	−0·2205	−0·2705	−0·00560	0·236	0·025
12·88	1·241	0·0255	0·0172	1·216	−0·2518	−0·2819	−0·00599	0·232	0·024
13·88	1·130	0·0748	−0·0349	1·115	−0·1985	−0·3059	−0·00894	0·274	0·045
14·87	1·060	0·1098	−0·0576	1·053	−0·1659	−0·3172	−0·00465	0·301	0·028
15·87	1·038	0·1291	−0·0680	1·033	−0·1596	−0·3197	−0·00764	0·309	0·048
16·87	0·994	0·1391	−0·0607	0·992	−0·1555	−0·3055	−0·00418	0·308	0·027
17·87	0·954	0·1470	−0·0560	0·953	−0·1527	−0·2909	−0·00418	0·305	0·027
18·85	0·547	0·2314	−0·0761	0·592	0·0422	−0·2234	−0·00124	0·377	−0·029

TABLE 4—*continued*

Fully Corrected Experimental Results 12·2% *t/c RAE* 100.

$R_c = 1{\cdot}33 \times 10^6$ $M = 0{\cdot}11$ Negative incidence

α	C_L	C_D	$C_{m_{c/4}}$	C_N	C_T	C_{m_x}	C_{m_z}	X	Z
−1·17	−0·126	0·0008	−0·0005	−0·126	−0·0018	0·0305	0·00057	0·242	−0·318
−2·18	−0·231	0·0022	−0·0024	−0·231	−0·0066	0·0546	0·00109	0·236	−0·165
−3·18	−0·336	0·0020	−0·0031	−0·336	−0·0167	0·0796	0·00163	0·237	−0·098
−4·19	−0·445	0·0036	−0·0039	−0·444	−0·0289	0·1053	0·00215	0·237	−0·074
−5.19	−0·551	0·0043	−0·0060	−0·549	−0·0456	0·1293	0·00255	0·236	−0·056
−6·20	−0·652	0·0054	−0·0087	−0·649	−0·0650	0·1510	0·00319	0·233	−0·049
−7·20	−0·769	0·0073	−0·0072	−0·764	−0·0891	0·1808	0·00368	0·237	−0·041
−8·20	−0·866	0·0124	−0·0120	−0·859	−0·1113	0·1994	0·00414	0·232	−0·037
−9·21	−0·964	0·0105	−0·0101	−0·953	−0·1439	0·2246	0·00465	0·236	−0·032
−10·21	−1·045	0·0139	−0·0125	−1·031	−0·1716	0·2413	0·00505	0·234	−0·029
−11·21	−1·131	0·0207	0·0422	−1·113	−0·1996	0·3160	0·00559	0·284	−0·028
−12·22	−1·213	0·0231	−0·0166	−1·190	−0·2341	0·2762	0·00594	0·232	−0·025
−13·22	−1·278	0·0253	−0·0198	−1·250	−0·2677	0·2876	0·00650	0·230	−0·024
−14·22	−1·170	0·0783	−0·0044	−1·153	−0·2114	0·2795	0·00545	0·242	−0·026
−15·21	−0·904	0·1045	0·0506	−0·899	−0·1362	0·2723	0·00409	0·303	−0·030
−16·22	−1·126	0·1887	0·0279	−1·134	−0·1334	0·3087	0·00381	0·272	−0·029
−17·21	−1·029	0·1421	0·0445	−1·024	−0·1686	0·2976	0·00406	0·291	−0·024
−18·20	−0·837	0·1612	0·0676	−0·846	−0·1084	0·2767	0·00318	0·327	−0·029
−19·20	−0·821	0·1697	0·0650	−0·831	−0·1098	0·2706	0·00302	0·326	−0·027

TABLE 4—*continued*

Fully Corrected Experimental Results 12·2% *t/c RAE* 100.

$R_c = 0{\cdot}91 \times 10^6$ $M = 0{\cdot}076$ Positive incidence

α	C_L	C_D	$C_{m_{c/4}}$	C_N	C_T	C_{m_x}	C_{m_z}	X	Z
0·83	0·085	0·0012	−0·0027	0·085	0·0000	−0·0237	−0·00045	0·278	–
1·84	0·197	0·0017	0·0024	0·197	−0·0046	−0·0504	−0·00100	0·256	0·217
2·84	0·311	0·0037	0·0029	0·311	−0·0117	−0·0736	−0·00157	0·237	0·134
3·85	0·392	0·0026	0·0048	0·391	−0·0237	−0·0915	−0·00201	0·234	0·085
5·86	0·622	0·0068	0·0038	0·620	−0·0567	−0·1487	−0·00304	0·240	0·054
6·86	0·719	0·0074	0·0058	0·715	−0·0786	−0·1702	−0·00341	0·238	0·043
7·86	0·784	0·0080	0·0033	0·778	−0·0994	−0·1882	−0·00373	0·242	0·038
8·87	0·907	0·0149	0·0113	0·898	−0·1251	−0·2099	−0·00434	0·234	0·035
9·87	0·990	0·0171	0·0119	0·978	−0·1529	−0·2288	−0·00474	0·234	0·031
10·87	1·058	0·0140	0·0161	1·041	−0·1857	−0·2400	−0·00530	0·230	0·029
11·88	1·133	0·0223	0·0158	1·113	−0·2113	−0·2581	−0·00547	0·232	0·026
12·88	1·171	0·0376	0·0151	1·150	−0·2244	−0·2679	−0·00576	0·233	0·026
13·87	0·991	0·0814	0·0525	0·981	−0·1585	−0·2911	−0·00769	0·297	0·048
14·85	0·493	0·1736	−0·0099	0·521	0·0413	−0·1396	−0·00118	0·268	−0·029

$R_c = 0{\cdot}91 \times 10^6$ $M = 0{\cdot}076$ Negative incidence

α	C_L	C_D	$C_{m_{c/4}}$	C_N	C_T	C_{m_x}	C_{m_z}	X	Z
−1·17	−0·123	0·0009	−0·0023	−0·123	−0·0016	0·0279	0·00055	0·227	−0·349
−2·18	−0·230	0·0013	−0·0029	−0·230	−0·0075	0·0538	0·00107	0·233	−0·144
−3·18	−0·339	0·0034	−0·0031	−0·338	−0·0155	0·0802	0·00160	0·237	−0·104
−4·19	−0·432	0·0038	−0·0058	−0·431	−0·0277	0·1003	0·00211	0·233	−0·076
−6·20	−0·653	0·0045	−0·0040	−0·650	−0·0660	0·1561	0·00317	0·240	−0·048
−7·20	−0·766	0·0106	−0·0057	−0·761	−0·0855	0·1818	0·00359	0·239	−0·042
−8·20	−0·826	0·0101	−0·0065	−0·819	−0·1079	0·1951	0·00408	0·238	−0·038
−9·21	−0·952	0·0117	−0·0076	−0·942	−0·1408	0·2241	0·00471	0·238	−0·033
−10·21	−1·025	0·0212	−0·0099	−1·013	−0·1609	0·2393	0·00504	0·236	−0·031
−11·21	−1·102	0·0237	−0·0123	−1·085	−0·1910	0·2548	0·00542	0·235	−0·028
−12·22	−1·173	0·0250	−0·0142	−1·152	−0·2238	0·2689	0·00594	0·233	−0·027
−13·22	−1·206	0·0321	−0·0148	−1·182	−0·2445	0·2756	0·00628	0·233	−0·026
−14·21	−1·107	0·0880	0·0411	−1·095	−0·1866	0·3108	0·00520	0·284	−0·028
−15·21	−1·067	0·1094	0·0436	−1·059	−0·1745	0·3041	0·00524	0·287	−0·030
−17·21	−1·091	0·1383	0·0421	−1·083	−0·1908	0·3088	0·00517	0·285	−0·027
−18·20	−0·609	0·2475	0·0850	−0·656	0·0448	0·2485	0·00114	0·379	0·026

TABLE 4—*continued*

Fully Corrected Experimental Results 12·2% *t/c* RAE 100

$R_c = 0{\cdot}66 \times 10^6$ $M = 0{\cdot}056$ Postive and negative incidences

α	C_L	C_D	$C_{m_{c/4}}$	C_N	C_T	C_{m_x}	C_{m_z}	X	Z
9·87	0·941	0·0157	0·0177	0·929	−0·1457	−0·2110	−0·00460	0·227	0·032
10·87	1·008	0·0166	0·0170	0·993	−0·1738	−0·2273	−0·00499	0·229	0·029
11·87	1·053	0·0218	0·0208	1·035	−0·1953	−0·2337	−0·00540	0·226	0·028
12·87	1·068	0·0532	−0·0070	1·053	−0·1861	−0·2660	−0·00539	0·253	0·029
13·87	1·008	0·0790	0·0318	0·998	−0·1650	−0·2138	−0·00488	0·214	0·030
14·85	0·491	0·1767	−0·0698	0·520	0·0450	−0·1991	−0·00110	0·383	−0·025
−10·21	−1·004	0·0254	−0·0136	−0·993	−0·1530	0·2310	0·00466	0·233	−0·030
−11·21	−1·082	0·0301	−0·0148	−1·067	−0·1808	0·2 81	0·00506	0·233	−0·028
−12·21	−1·082	0·0305	−0·0214	−1·064	−0·1991	0·2402	0·00554	0·226	−0·028
−13·21	−1·118	0·0571	+0·0138	−1·101	−0·2851	0·2851	0·00521	0·259	−0·026
−14·21	−1·009	0·0973	0·0473	−1·002	−0·1533	0·2943	0·00438	0·294	−0·029
−15·19	−0·540	0·1924	0·0710	−0·571	0·0442	0·2131	0·00118	0·373	0·027

$R_c = 0{\cdot}55 \times 10^6$ $M = 0{\cdot}047$ Positive and negative incidences

α	C_L	C_D	$C_{m_{c/4}}$	C_N	C_T	C_{m_x}	C_{m_z}	X	Z
10·87	0·995	0·0180	0·0011	0·981	−0·1700	−0·2402	−0·00498	0·245	0·029
11·87	1·050	0·0246	0·0213	1·033	−0·1920	−0·2328	−0·00525	0·225	0·027
12·87	1·068	0·0513	0·0020	1·052	−0·1879	−0·2569	−0·00530	0·244	0·028
13·85	0·476	0·1626	−0·0670	0·501	0·0439	−0·1916	−0·00107	0·383	−0·024
−10·21	−1·007	0·0169	−0·0128	−0·994	−0·1619	0·2317	0·00506	0·233	−0·031
−11·21	−1·062	0·0285	−0·0142	−1·047	−0·1785	0·2435	0·00526	0·233	−0·029
−12·21	−1·101	0·0348	−0·0168	−1·084	−0·1989	0·2496	0·00555	0·230	−0·028
−13·21	−1·084	0·0495	0·0028	−1·066	−0·1995	0·2649	0·00566	0·248	−0·028
−14·19	−0·539	0·1792	0·0700	−0·566	0·0416	0·2109	0·00105	0·372	0·025

TABLE 5

Fully Smoothed and Corrected Results 12·2% *t/c RAE* 100.

$R_c = 1{\cdot}78 \times 10^6 \quad M = 0{\cdot}150$

α	C_L	C_D	$C_{m_{c/4}}$	C_N	C_T
1·00	0·107	0·0009	0·0010	0·107	−0·0010
2·01	0·213	0·0010	0·0018	0·213	−0·0065
3·01	0·320	0·0014	0·0025	0·320	−0·0155
4·02	0·427	0·0020	0·0034	0·426	−0·0279
5·02	0·531	0·0026	0·0042	0·529	−0·0439
6·03	0·639	0·0041	0·0052	0·636	−0·0631
7·03	0·744	0·0054	0·0060	0·739	−0·0847
8·03	0·846	0·0077	0·0069	0·839	−0·1091
9·04	0·946	0·0097	0·0076	0·935	−0·1380
10·04	1·041	0·0123	0·0083	1·027	−0·1684
11·04	1·129	0·0157	0·0096	1·111	−0·2002
12·05	1·213	0·0206	0·0121	1·190	−0·2330
13·05	1·289	0·0291	0·0146	1·262	−0·2627
14·05	1·359	0·0388	0·0173	1·328	−0·2923
15·03	1·079	0·1046	−0·0539	1·070	−0·1789
16·03	1·033	0·1262	−0·0590	1·028	−0·1641
17·03	1·003	0·1454	−0·0613	1·001	−0·1547
18·03	0·968	0·1634	−0·0642	0·971	−0·1442
19·03	0·931	0·1806	−0·0658	0·939	−0·1329
20·03	0·888	0·1969	−0·0675	0·902	−0·1193
21·02	0·814	0·2123	−0·0706	0·836	−0·0938
22·02	0·635	0·3006	−0·0897	0·702	0·0405

$R_c = 1{\cdot}33 \times 10^6 \quad M = 0{\cdot}112$

α	C_L	C_D	$C_{m_{c/4}}$	C_N	C_T
1·00	0·106	0·0009	0·0008	0·106	−0·0010
2·01	0·212	0·0015	0·0019	0·211	−0·0060
3·01	0·317	0·0022	0·0034	0·317	−0·0145
4·02	0·423	0·0025	0·0046	0·422	−0·0271
5·02	0·528	0·0034	0·0057	0·527	−0·0429
6·03	0·634	0·0049	0·0069	0·631	−0·0618
7·03	0·738	0·0078	0·0080	0·734	−0·0827
8·03	0·840	0·0104	0·0092	0·834	−0·1071
9·04	0·938	0·0126	0·0102	0·929	−0·1350
10·04	1·032	0·0147	0·0112	1·018	−0·1654
11·04	1·118	0·0161	0·0134	1·100	−0·1982
12·05	1·194	0·0201	0·0160	1·172	−0·2295
13·05	1·258	0·0261	0·0190	1·232	−0·2587
14·03	1·148	0·0739	−0·0200	1·132	−0·2068
15·03	1·062	0·1034	−0·0540	1·053	−0·1756
16·03	1·010	0·1231	−0·0596	1·005	−0·1609
17·03	0·961	0·1407	−0·0606	0·960	−0·1469
18·02	0·884	0·1576	−0·0632	0·889	−0·1236
19·01	0·599	0·2480	−0·0811	0·647	0·0394

TABLE 5—*continued*

Fully Smoothed and Corrected Results 12·2% *t/c RAE* 100.

$R_c = 0{\cdot}91 \times 10^6 \quad M = 0{\cdot}076$

α	C_L	C_D	$C_{m_{c/4}}$	C_N	C_T
1·00	0·105	0·0008	0·0007	0·105	−0·0010
2·01	0·211	0·0016	0·0024	0·211	−0·0058
3·01	0·316	0·0027	0·0034	0·316	−0·0140
4·02	0·422	0·0031	0·0046	0·421	−0·0264
5·02	0·527	0·0043	0·0058	0·525	−0·0419
6·03	0·631	0·0061	0·0070	0·628	−0·0603
7·03	0·733	0·0081	0·0081	0·728	−0·0817
8·03	0·830	0·0100	0·0091	0·823	−0·1061
9·04	0·922	0·0135	0·0102	0·912	−0·1315
10·04	1·006	0·0178	0·0114	0·994	−0·1579
11·04	1·082	0·0208	0·0130	1·066	−0·1867
12·04	1·145	0·0264	0·0151	1·125	−0·2130
13·05	1·197	0·0340	0·0179	1·168	−0·2357
14·03	1·088	0·0844	−0·0427	1·076	−0·1820
15·03	1·027	0·1069	−0·0465	1·019	−0·1631
16·03	0·976	0·1240	−0·0473	0·973	−0·1505
17·01	0·553	0·2142	−0·0757	0·592	0·0429

$R_c = 0{\cdot}66 \times 10^6 \quad M = 0{\cdot}056$

α	C_L	C_D	$C_{m_{c/4}}$	C_N	C_T
10·04	0·980	0·0167	0·0125	0·968	−0·1504
11·04	1·048	0·0215	0·0137	1·033	−0·1782
12·04	1·094	0·0300	0·0156	1·077	−0·1990
13·04	1·108	0·0430	0·0171	1·089	−0·2078
14·03	1·010	0·0826	−0·0408	1·000	−0·1647
15·01	0·512	0·1822	−0·0699	0·542	0·0435

$R_c = 0{\cdot}55 \times 10^6 \quad M = 0{\cdot}047$

α	C_L	C_D	$C_{m_{c/4}}$	C_N	C_T
10·04	0·962	0·0158	0·0126	0·951	−0·1424
11·04	1·024	0·0213	0·0143	1·009	−0·1712
12·04	1·066	0·0291	0·0153	1·049	−0·1940
13·04	1·069	0·0423	0·0165	1·050	−0·2000
14·01	0·507	0·1709	−0·0683	0·533	0·0429

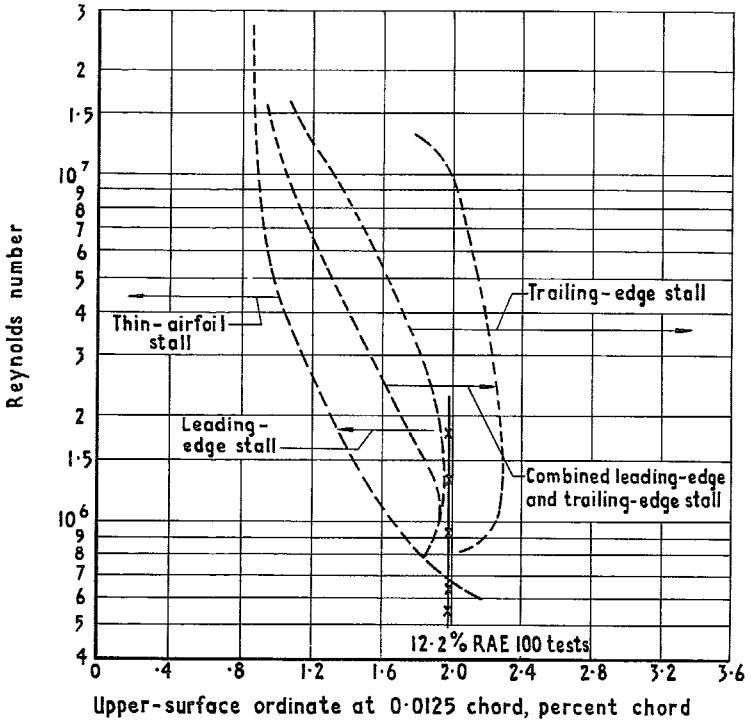

FIG. 1. The low-speed stalling characteristics of airfoil sections correlated with Reynolds number and the upper-surface ordinates of the airfoil sections at the 0·0125-chord station.

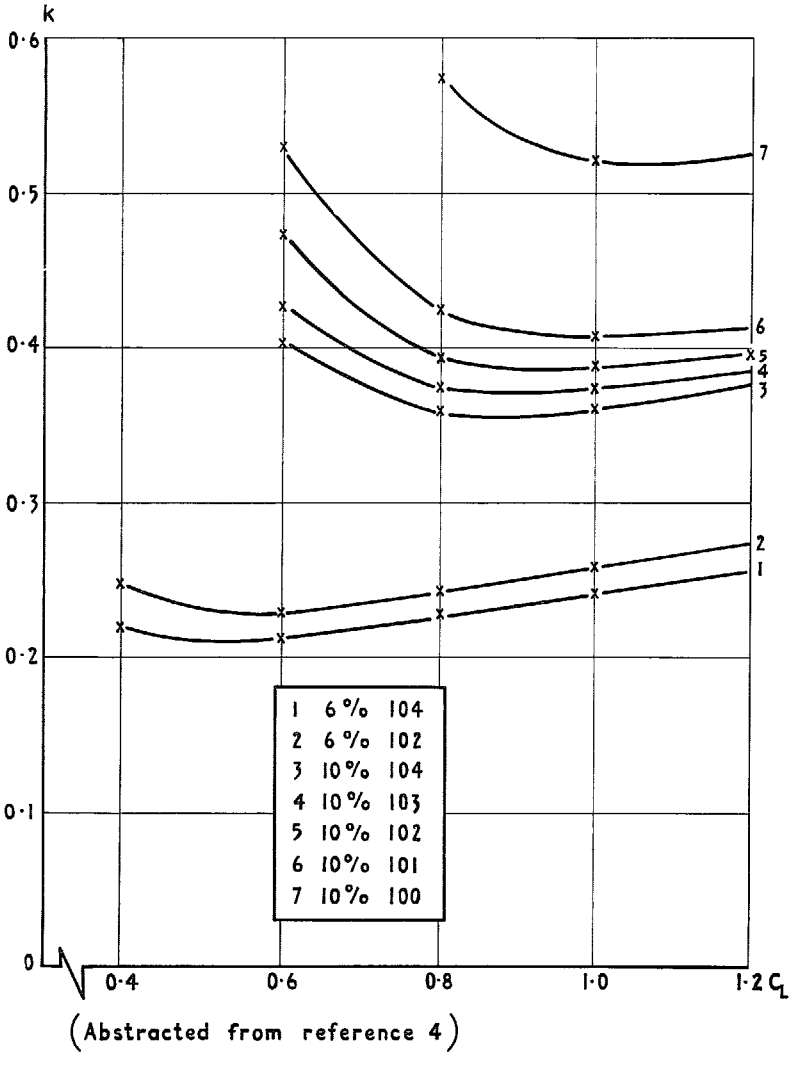

FIG. 2. Variation of k with C_L.

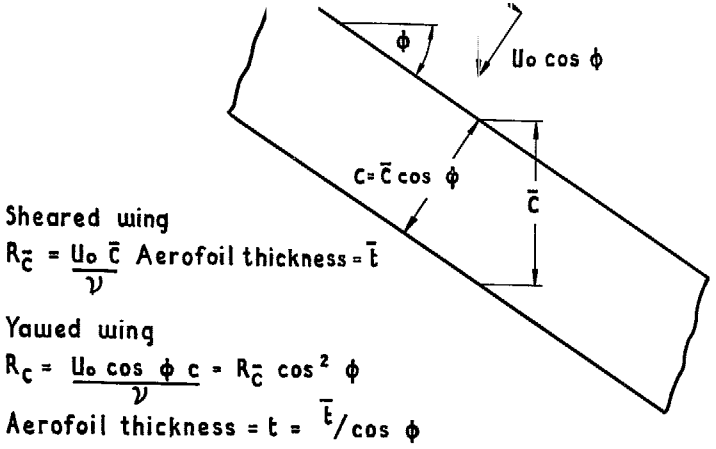

FIG. 3. Alternative definitions of chordal Reynolds number on a swept wing.

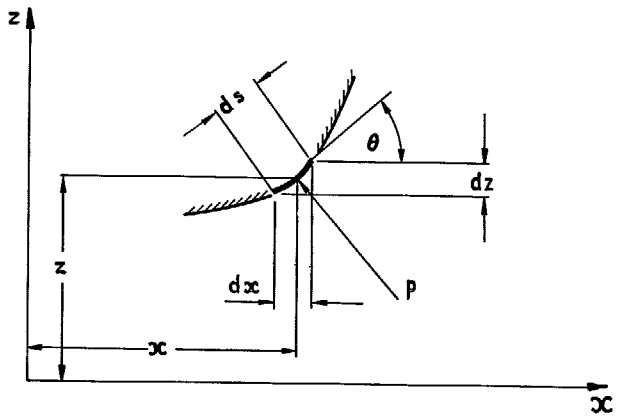

FIG. 4. Pressure forces acting on an element of the aerofoil surface.

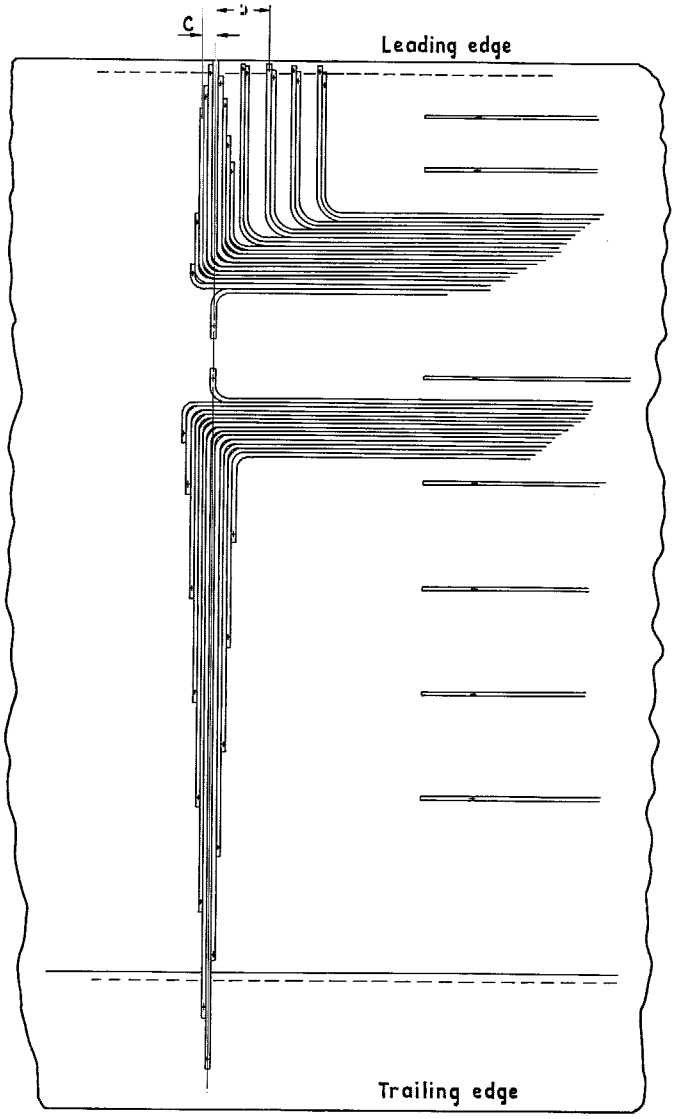

FIG. 5. Details of pressure tube layout.

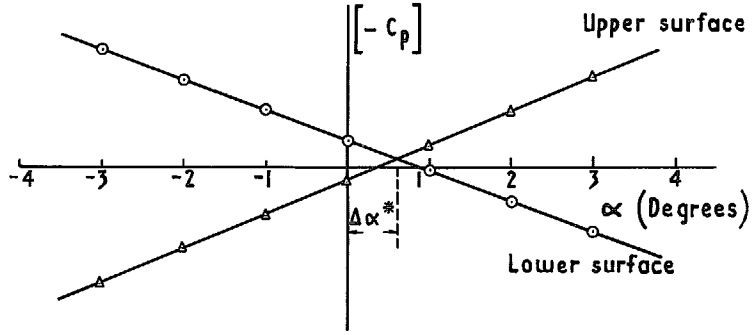

FIG. 6. Typical plot of C_p against α for two pressure holes on opposite sides of the aerofoil

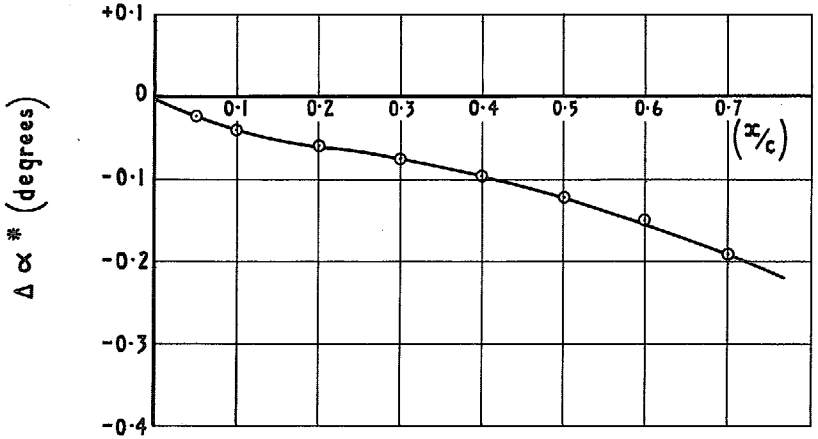

FIG. 7. Chordwise variation of wing incidence for which the local pressure difference across the wing is zero. Evaluated at the mid-span section of the wing.

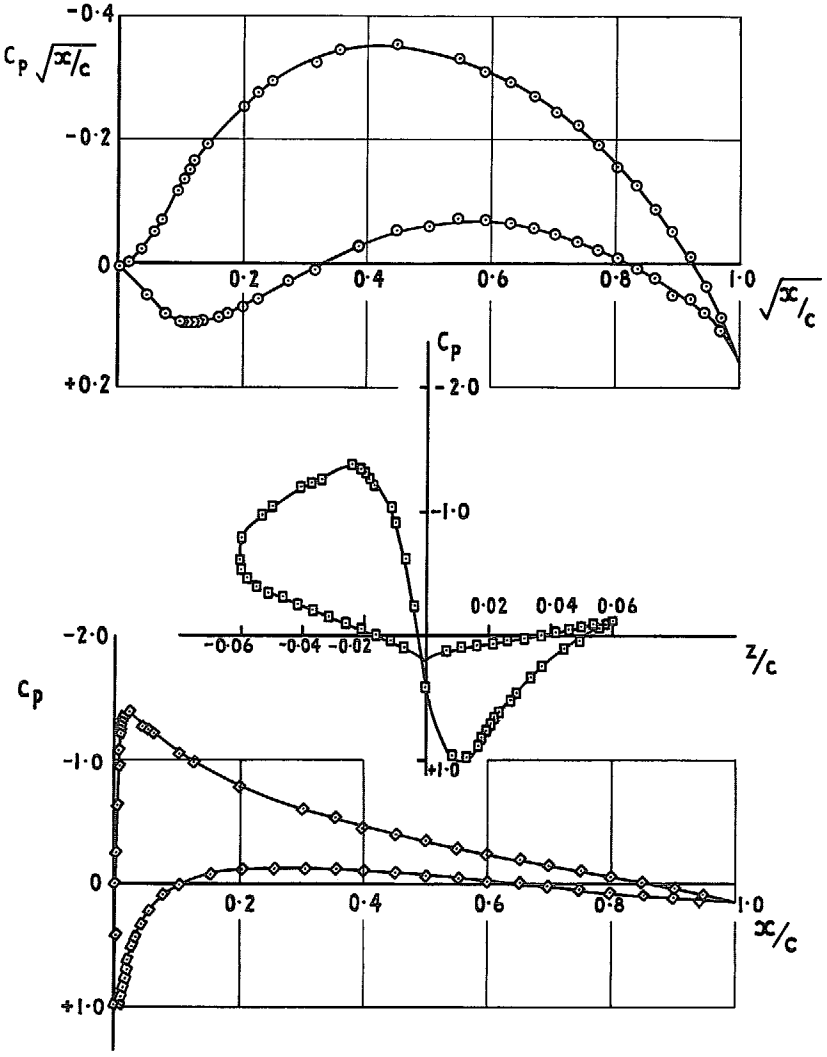

FIG. 8. Typical results sheet for integration ($\alpha = -3°$).

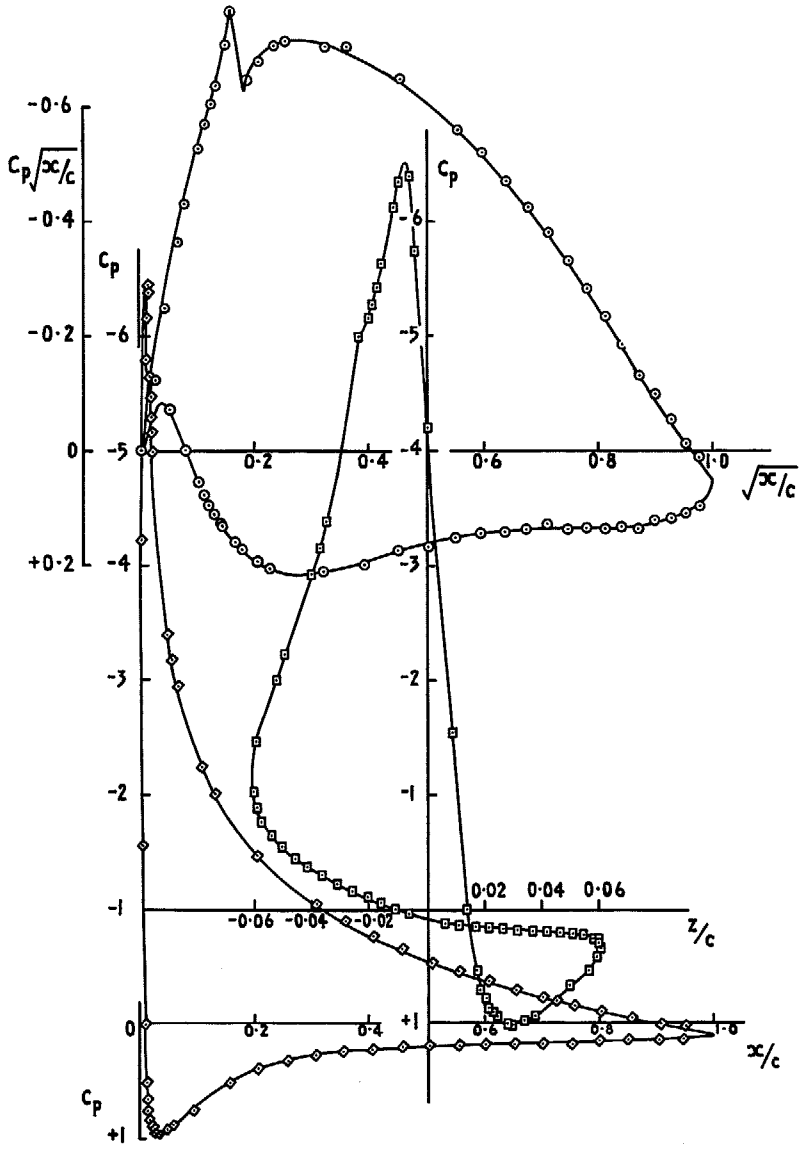

FIG. 9. Typical results sheet for integration ($\alpha = -11°$).

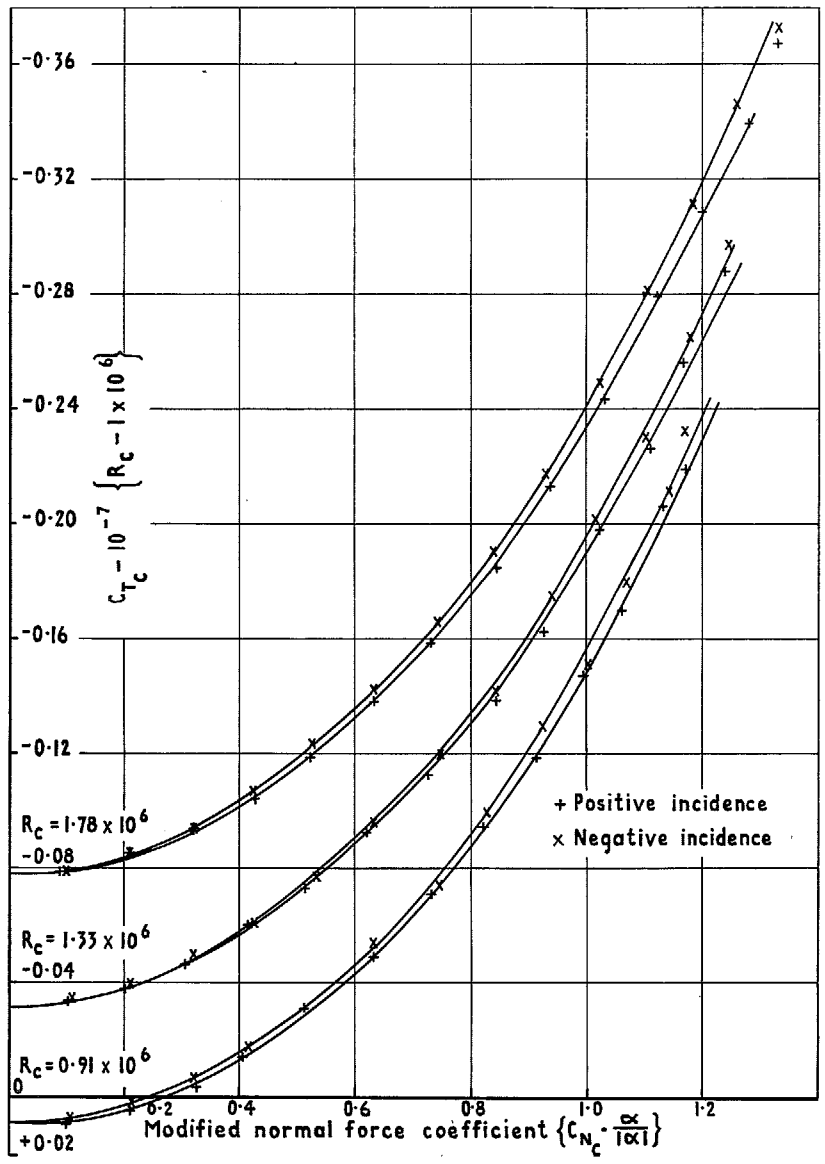

FIG. 10. Variation of uncorrected force coefficients at positive and negative incidences.

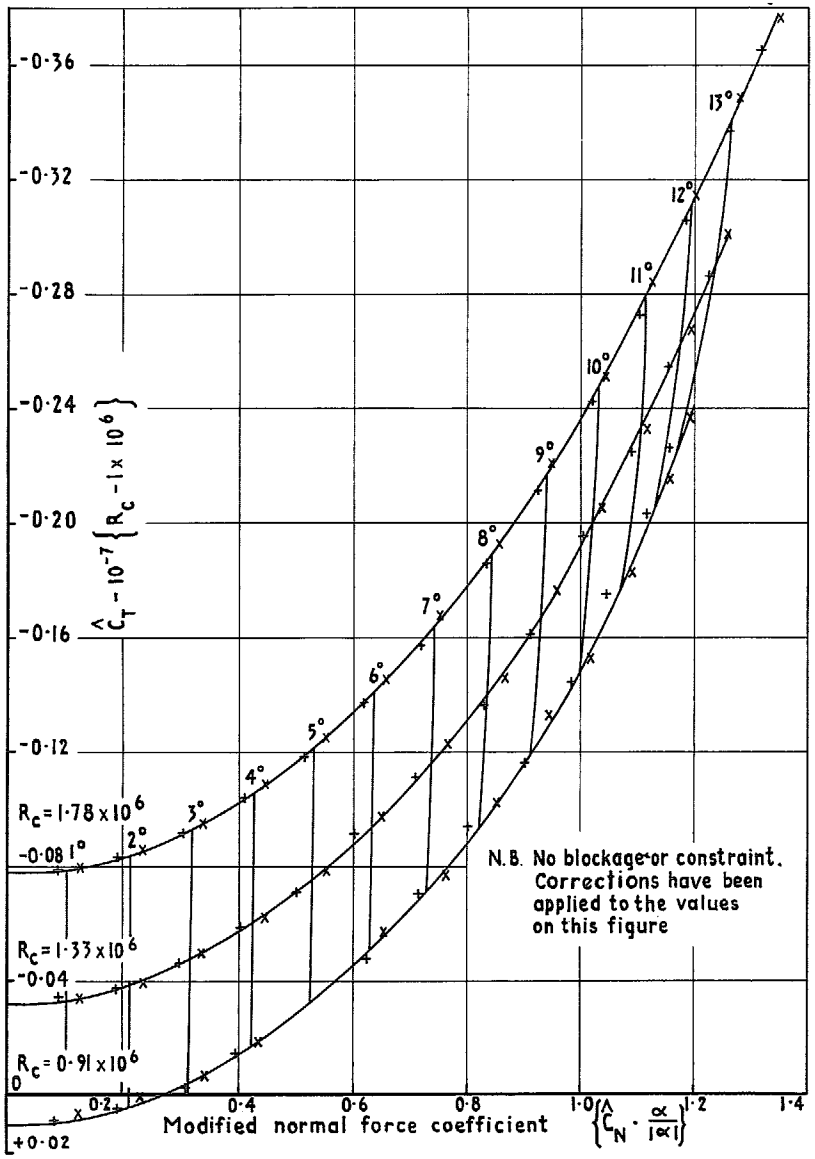

FIG. 11. Variation of corrected force coefficients at positive and

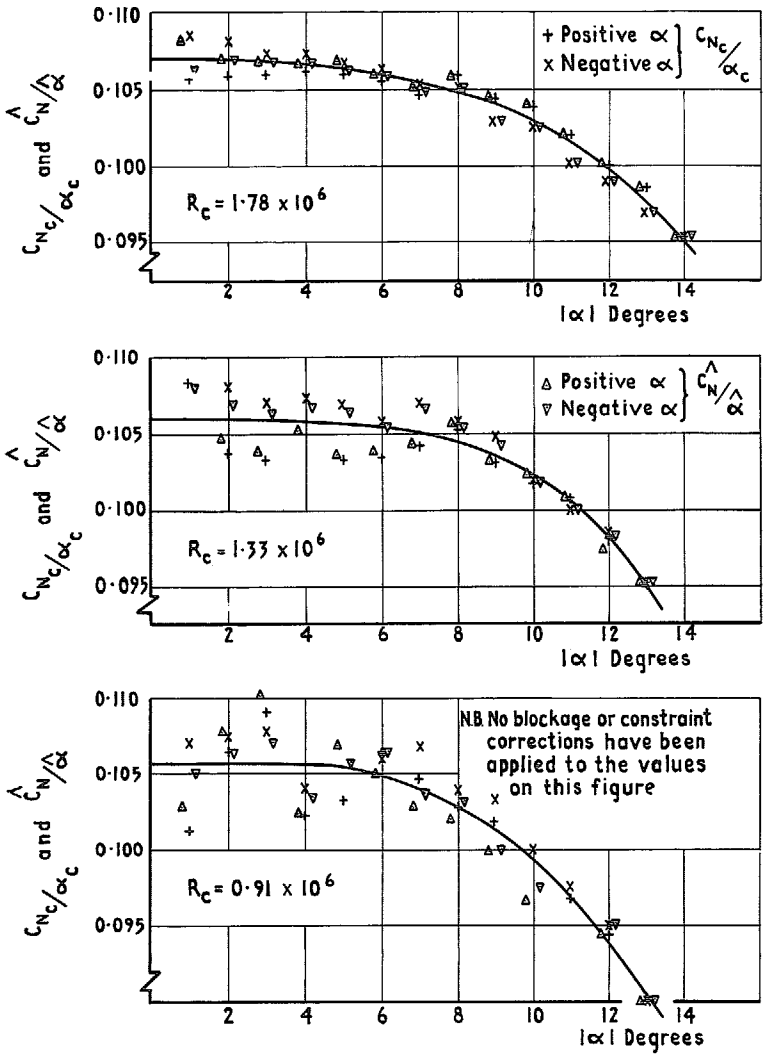

FIG. 12. Variation of C_N/α with incidence and Reynolds number before and after camber correction.

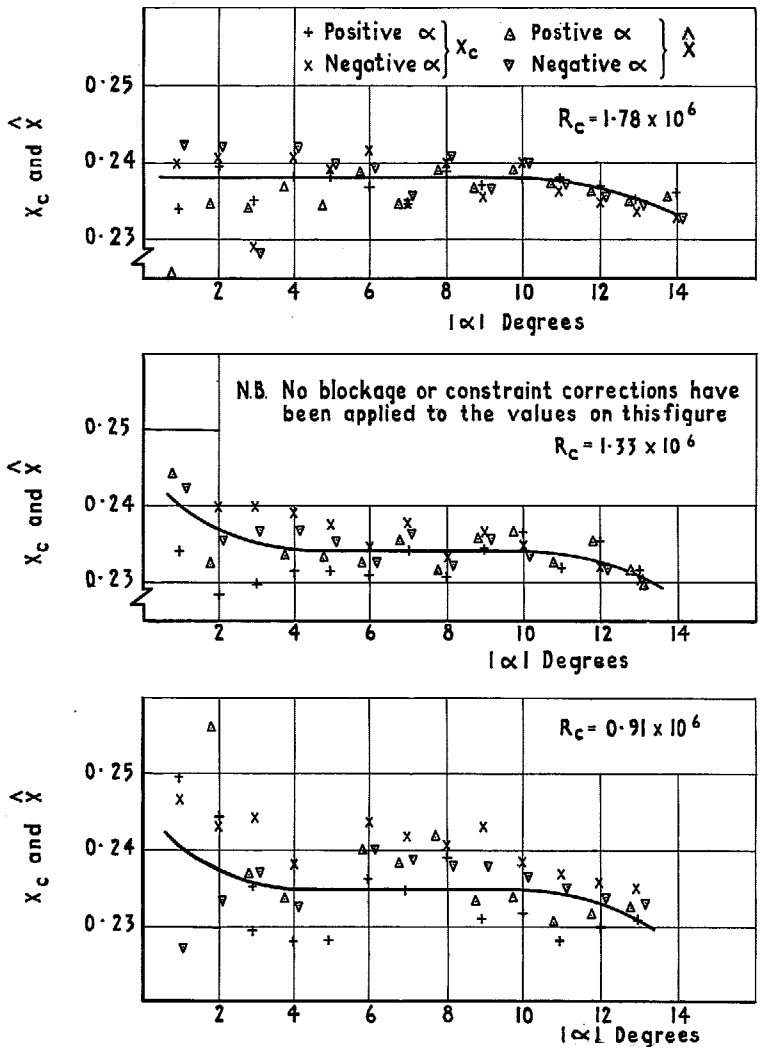

FIG. 13. Variation of chordwise centre of pressure with incidence and Reynolds number before and after camber correction.

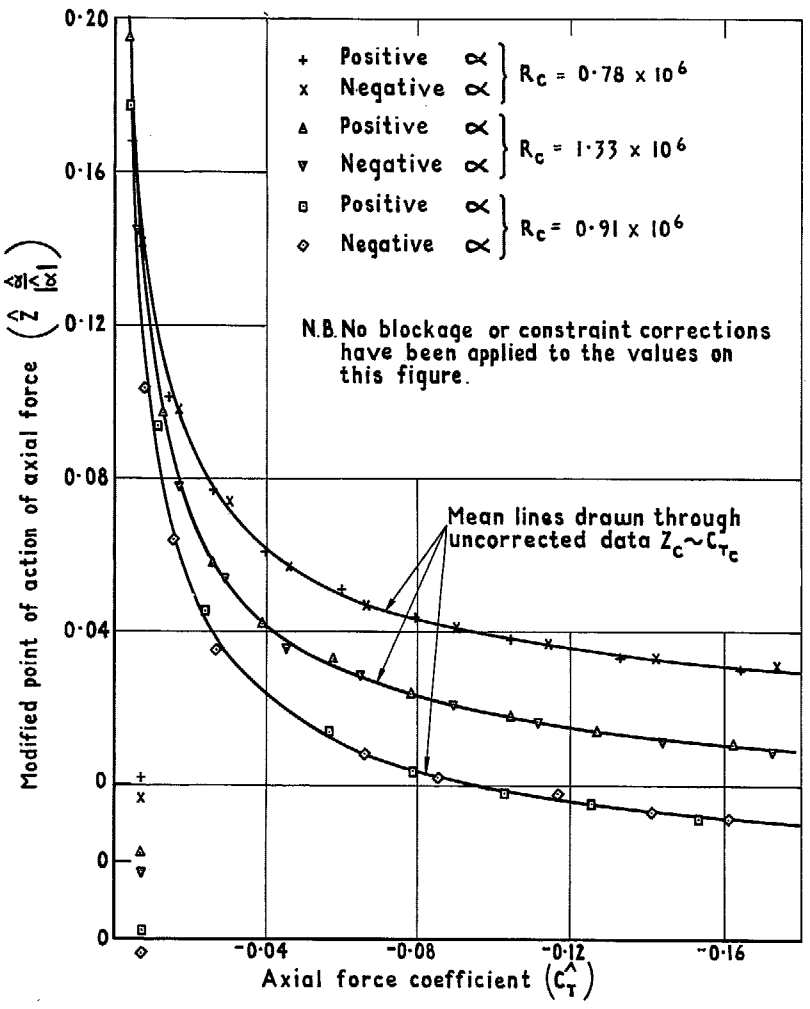

FIG. 14. Variation of axial force centre of pressure with incidence and Reynolds number before and after camber correction.

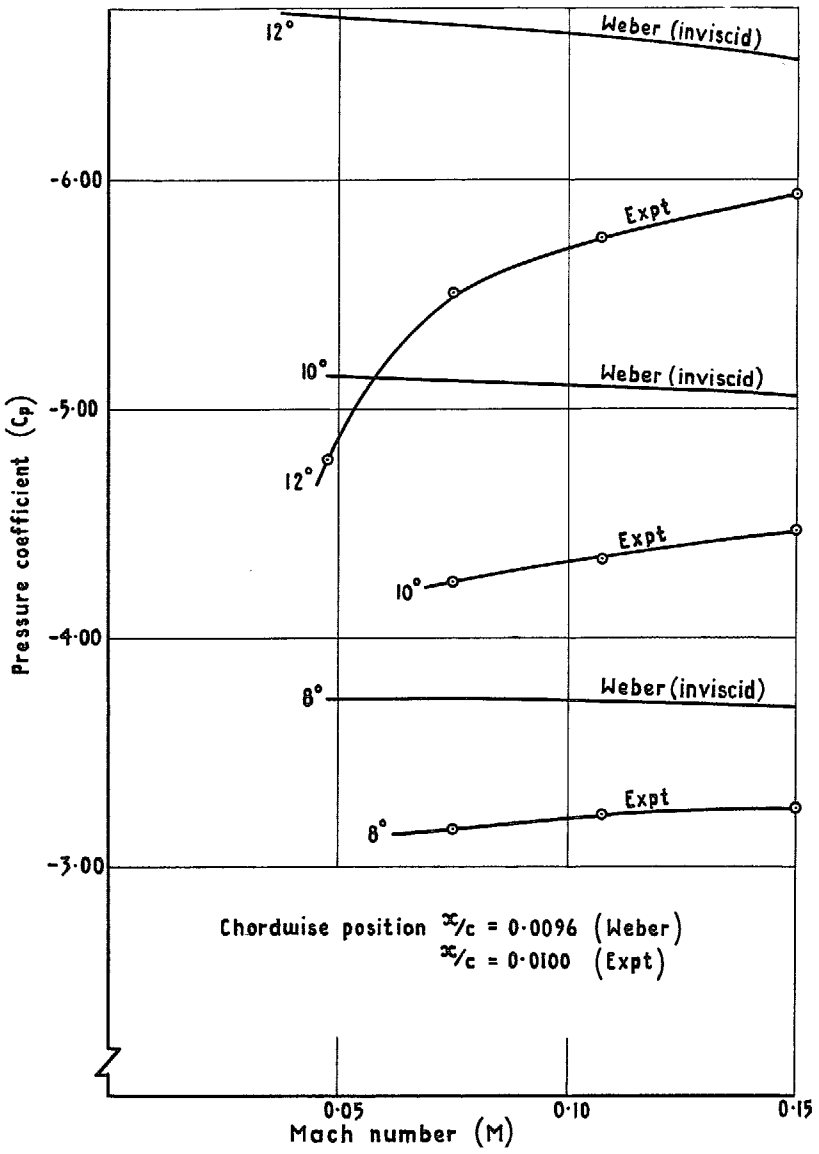

FIG. 15. Comparison of theoretical and experimental variation of local

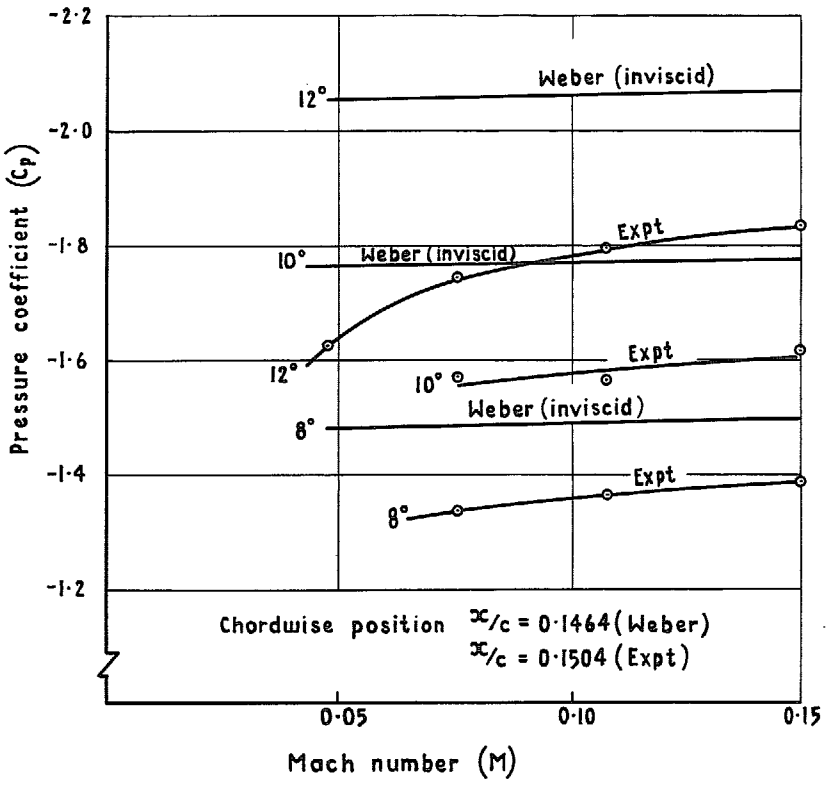

FIG. 16. Comparison of theoretical and experimental variation of local pressure with Mach number.

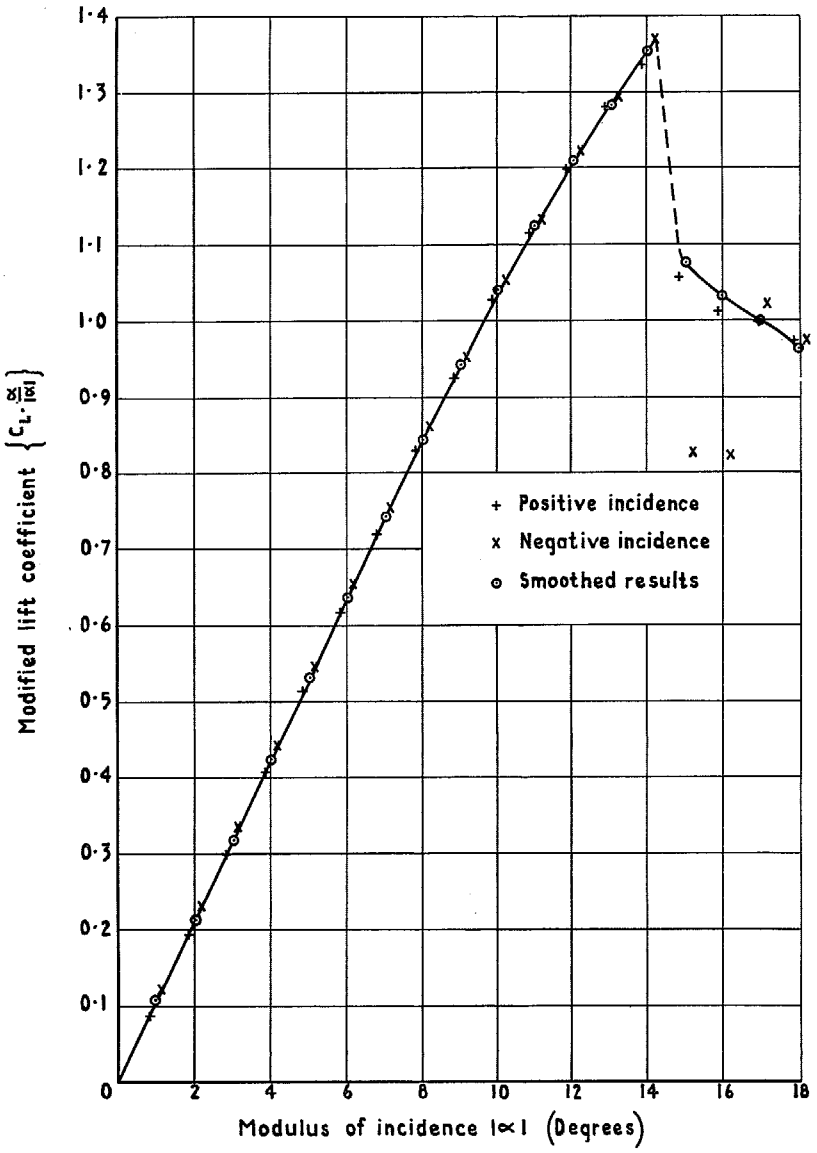

FIG. 17. Lift variation with incidence $R_c = 1{\cdot}78 \times 10^6$.

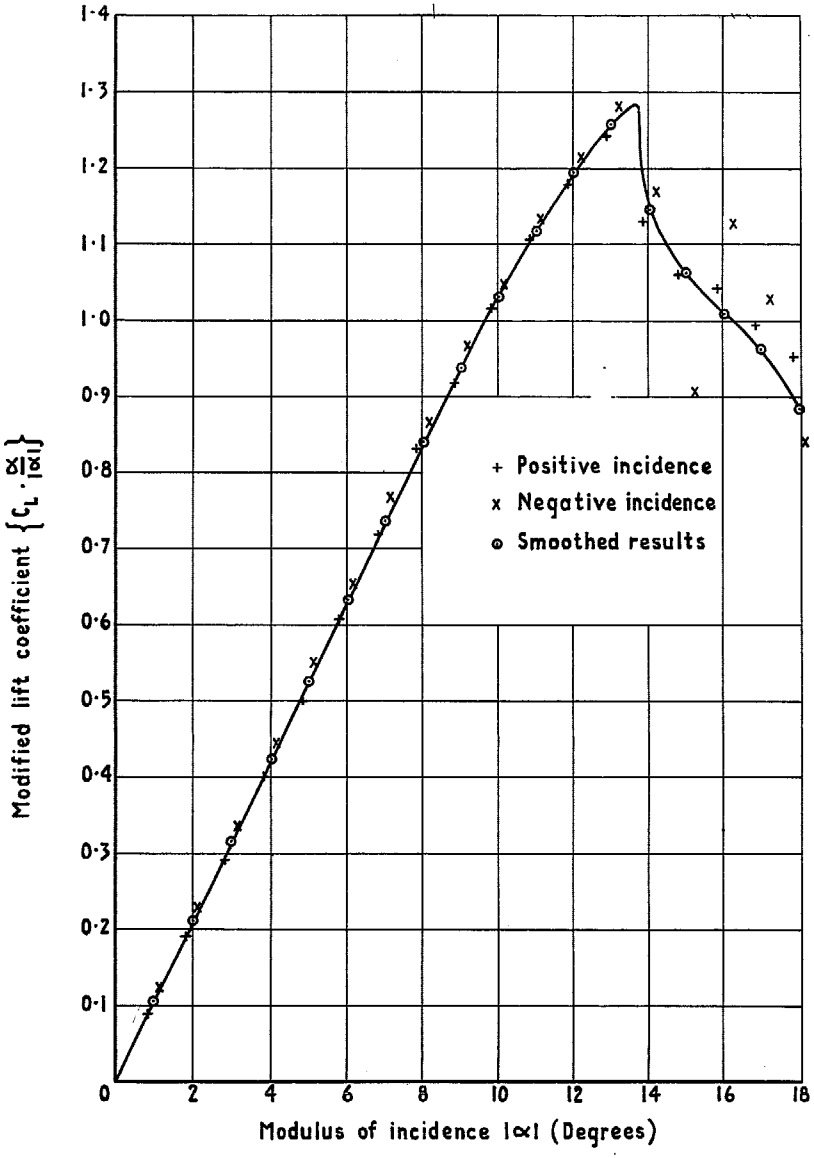

FIG. 18. Lift variation with incidence $R_c = 1{\cdot}33 \times 10^6$.

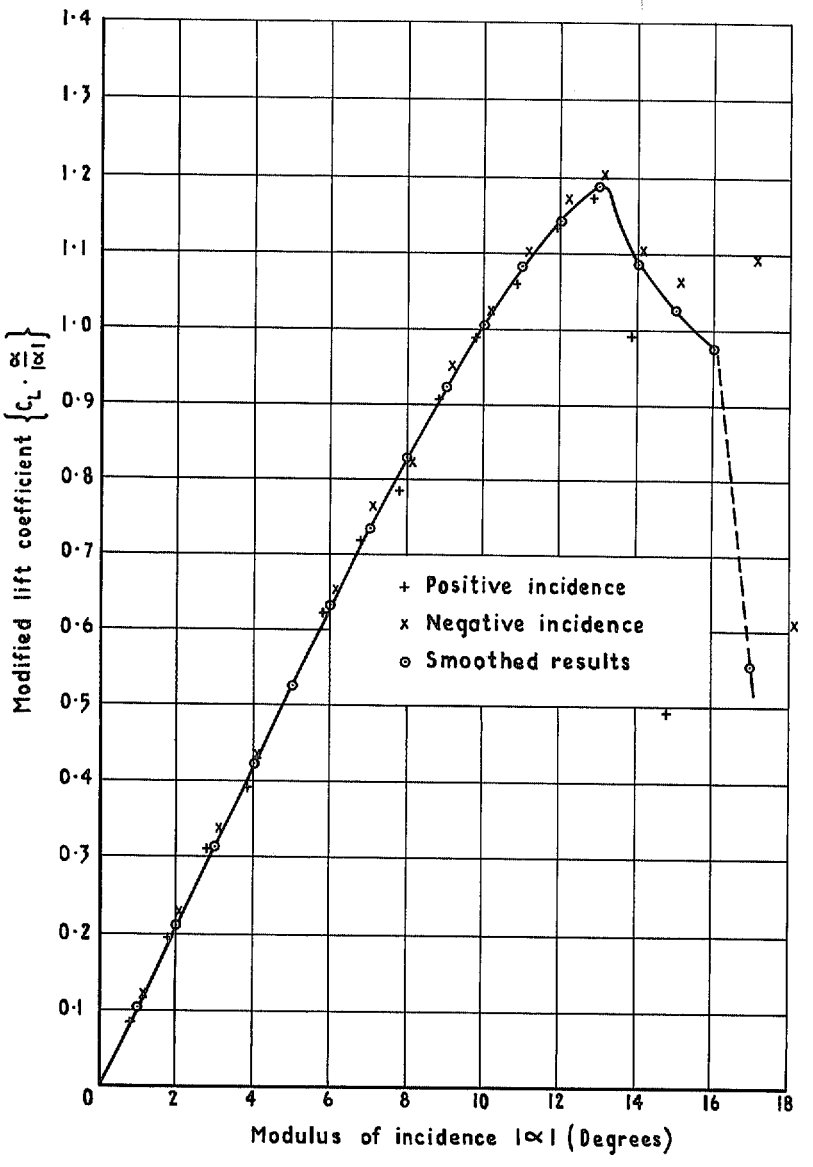

FIG. 19. Lift variation with incidence $R_c = 0{\cdot}91 \times 10^6$.

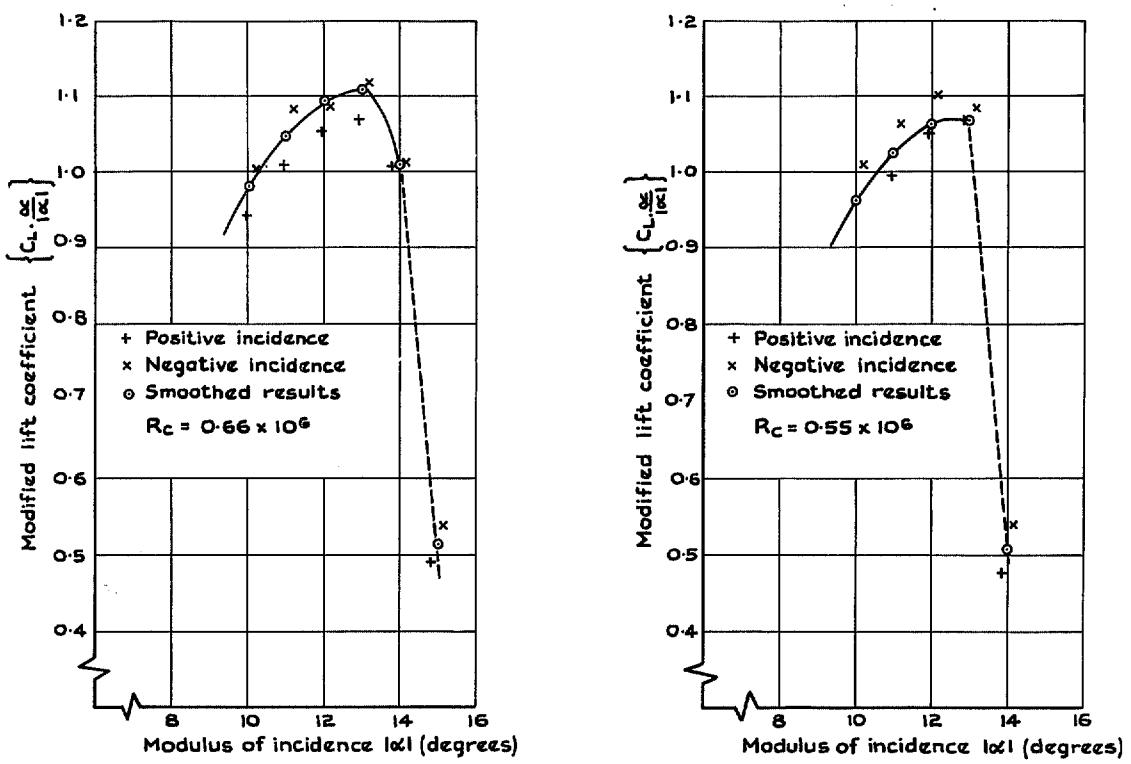

FIG. 20. Variation of lift with incidence near the stall at low Reynolds number.

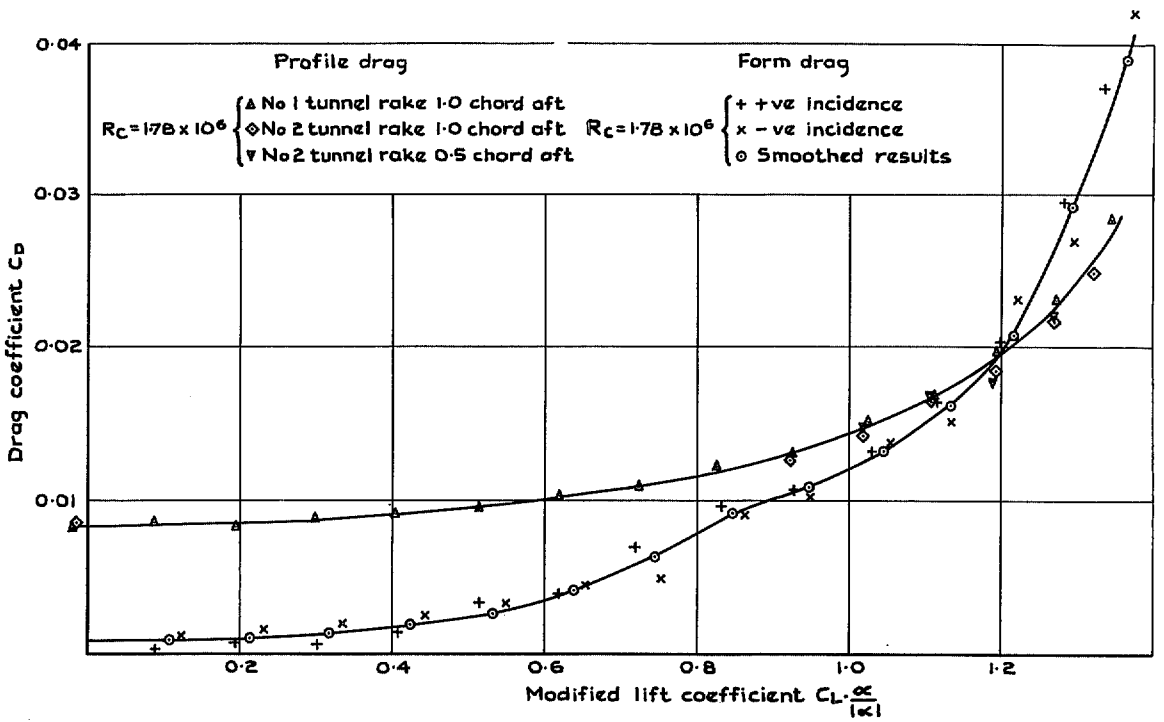

FIG. 21. Pre-stall variation of profile and form drag $R_c = 1{\cdot}78 \times 10^6$.

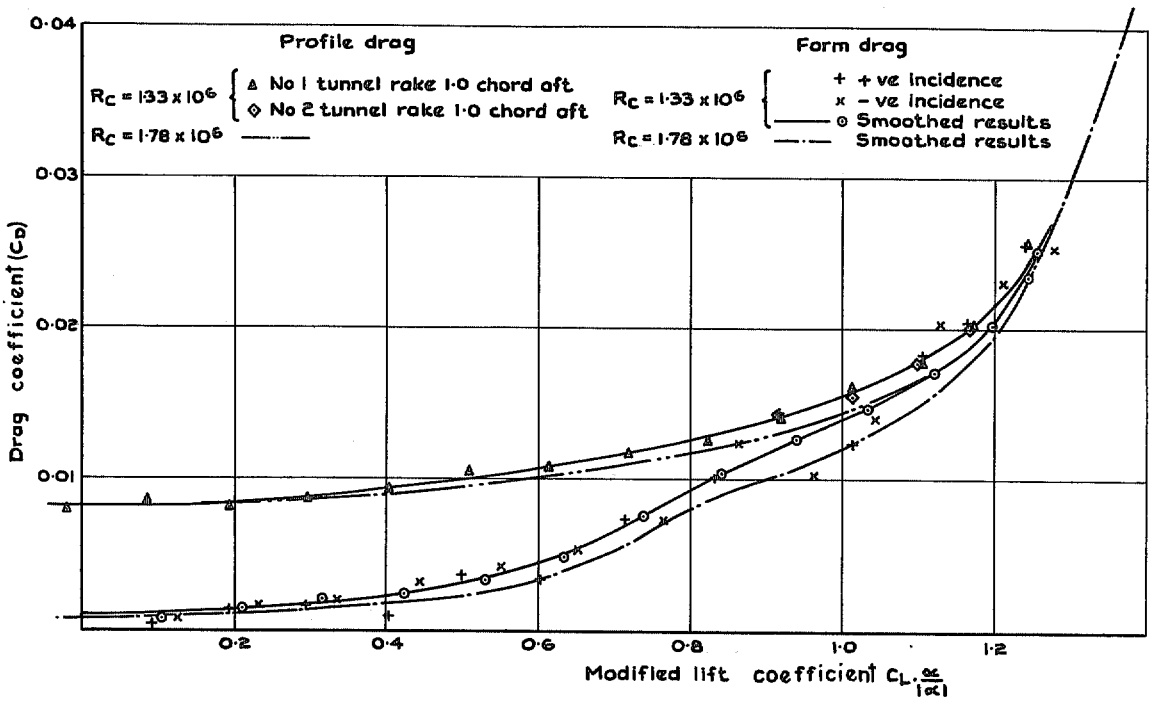

FIG. 22. Pre-stall variation of profile and form drag $R_c = 1{\cdot}33 \times 10^6$.

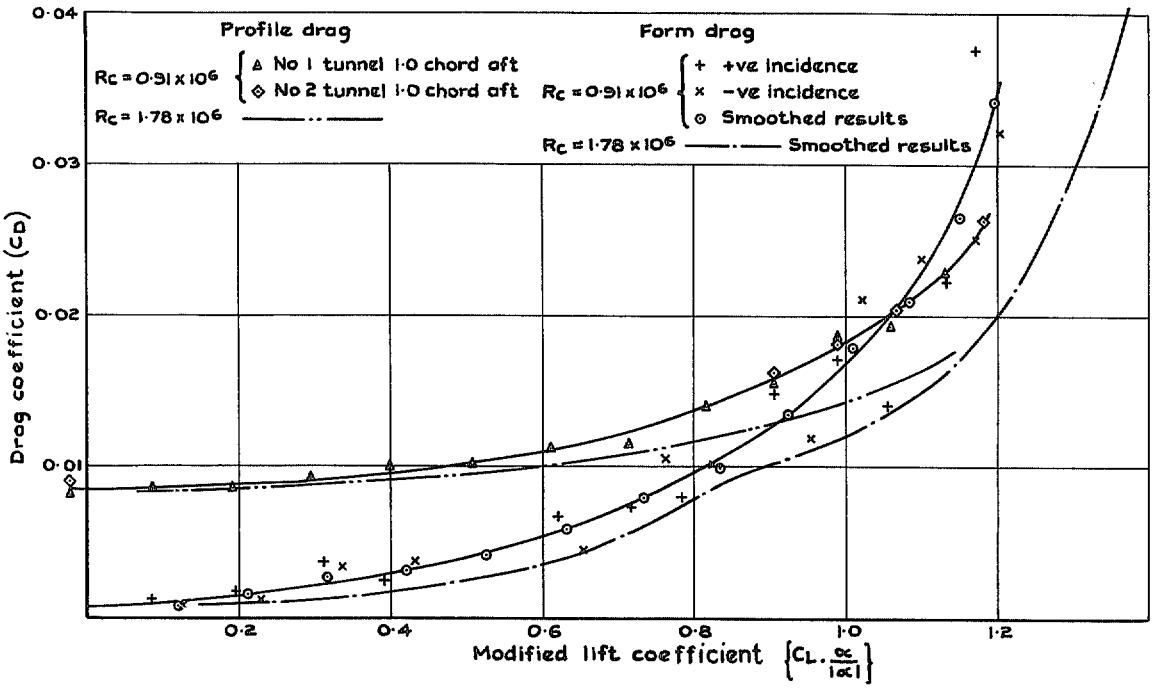

FIG. 23. Pre-stall variation of profile and form drag $R_c = 0{\cdot}91 \times 10^6$.

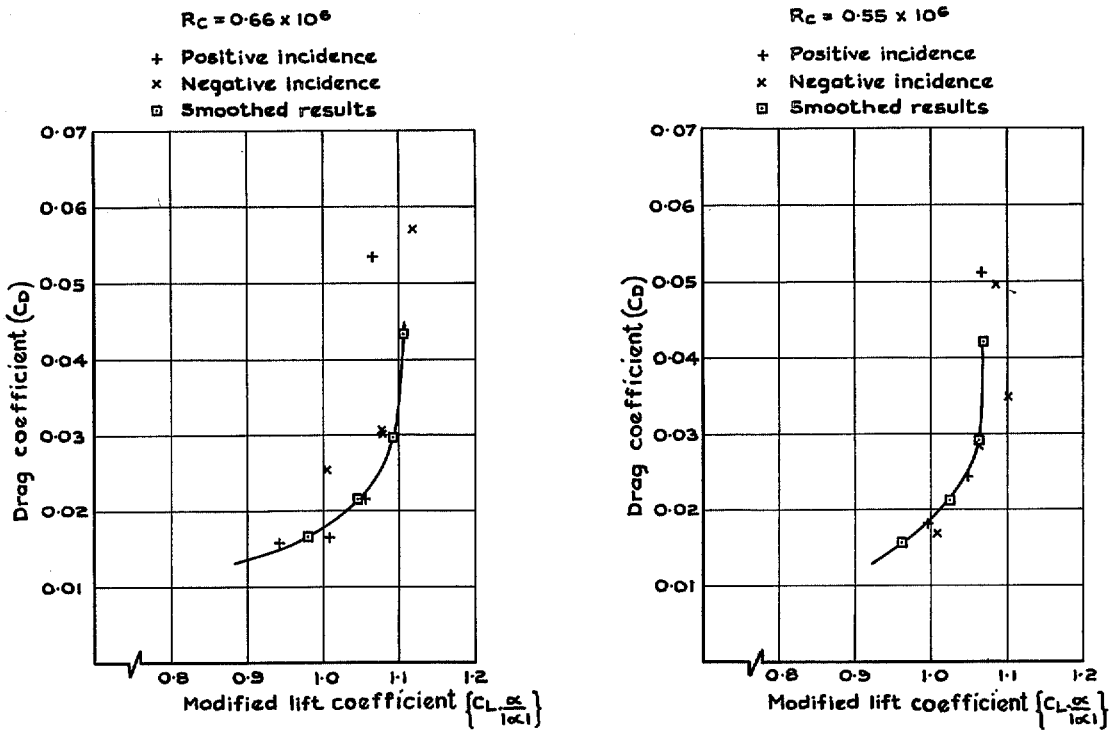

FIG. 24. Pre-stall variation of form drag at low Reynolds number.

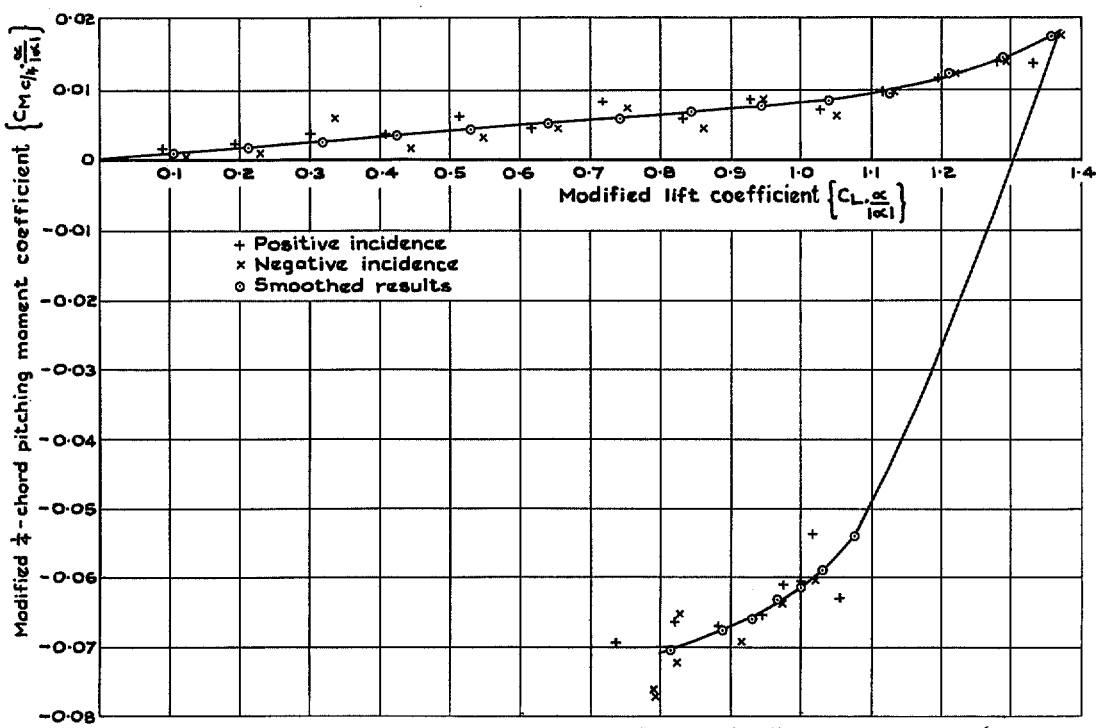

FIG. 25. Quarter-chord pitching moment variation with lift $R_c = 1{\cdot}78 \times 10^6$.

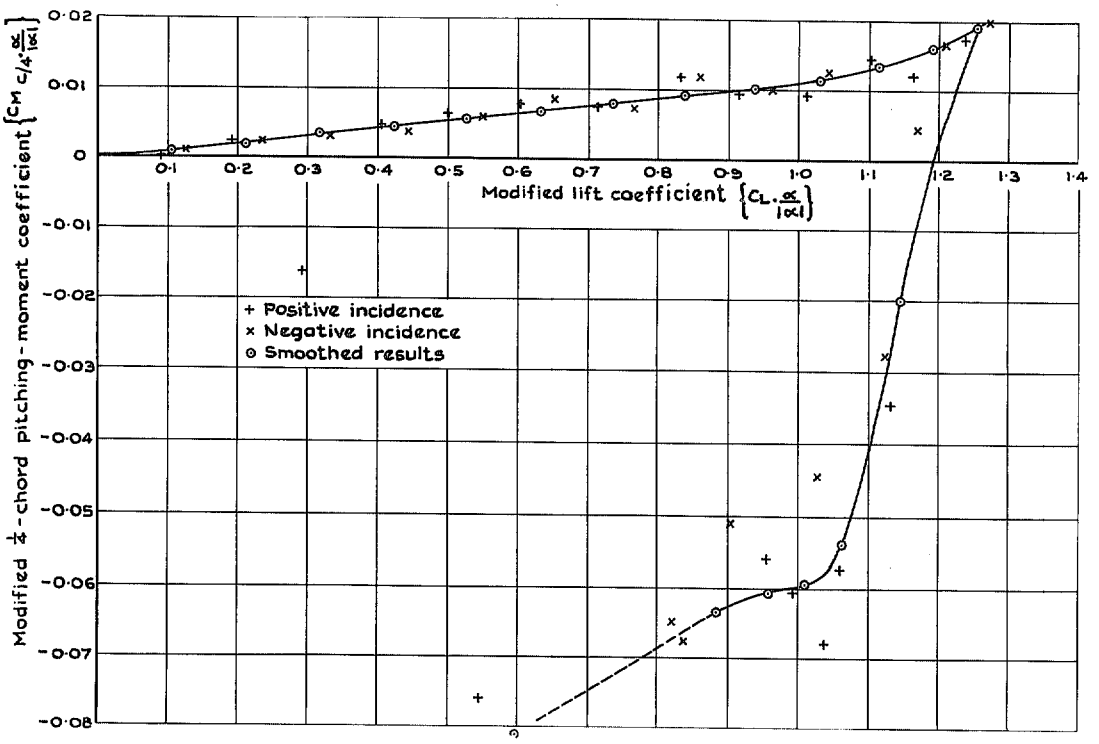

FIG. 26. Quarter-chord pitching moment variation with lift $R_c = 1{\cdot}33 \times 10^6$.

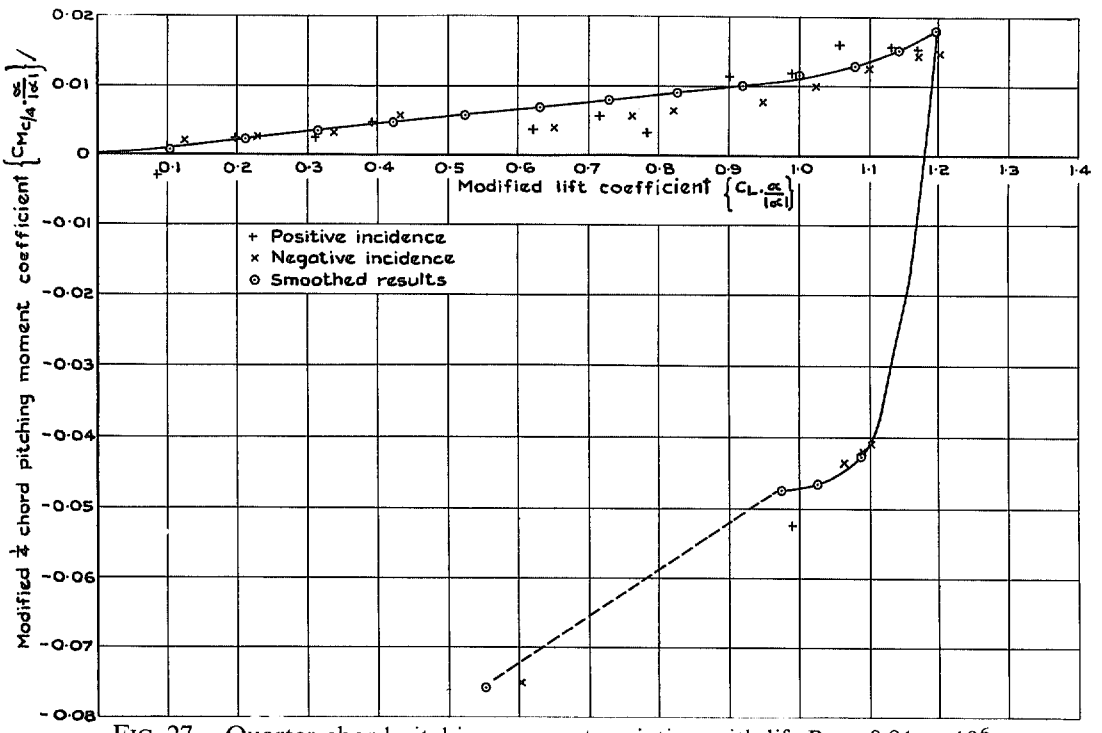

FIG. 27. Quarter-chord pitching moment variation with lift $R_c = 0{\cdot}91 \times 10^6$.

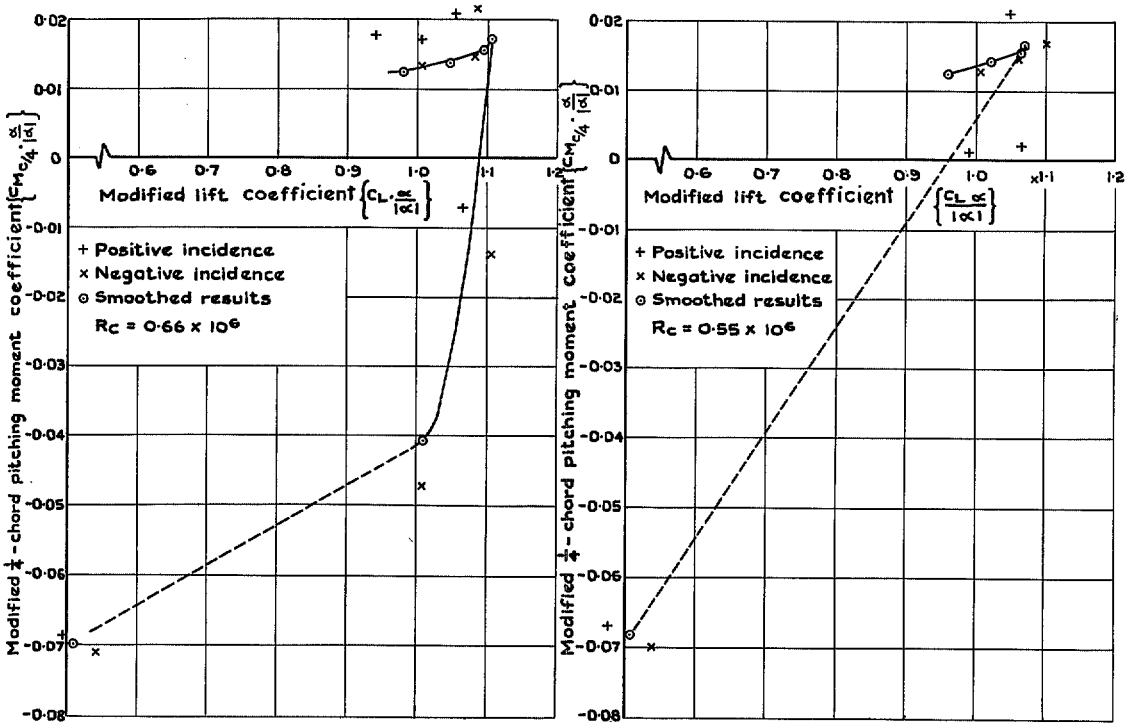

FIG. 28. Variation of $\frac{1}{4}$-chord pitching-moment coefficient with lift at low Reynolds number.

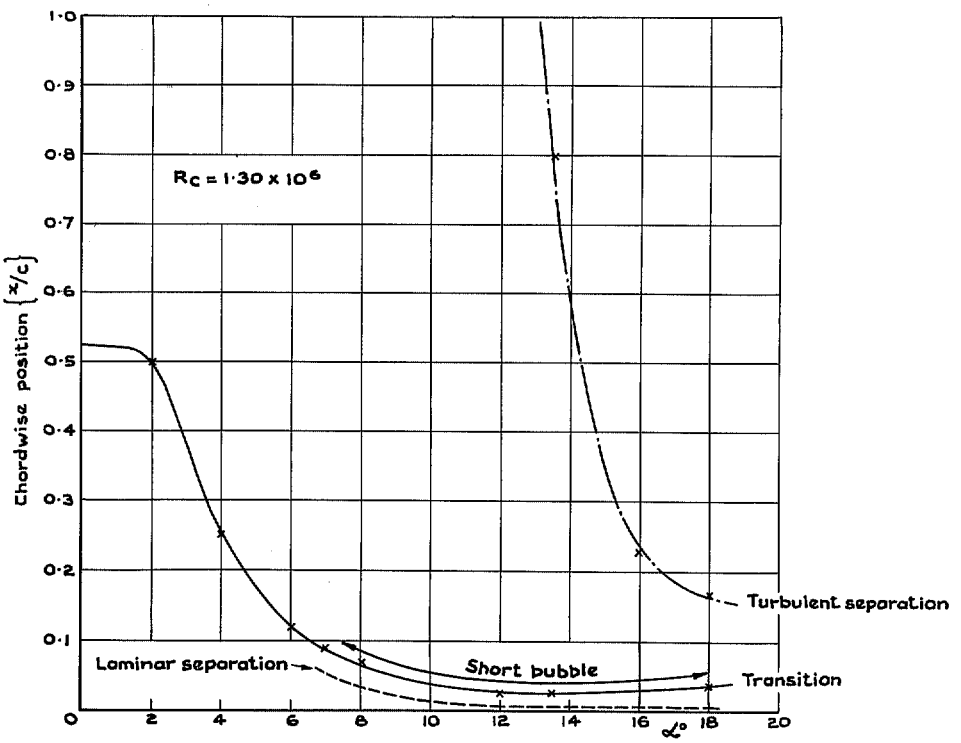

FIG. 29. Movement of significant boundary-layer fronts over an incidence range.

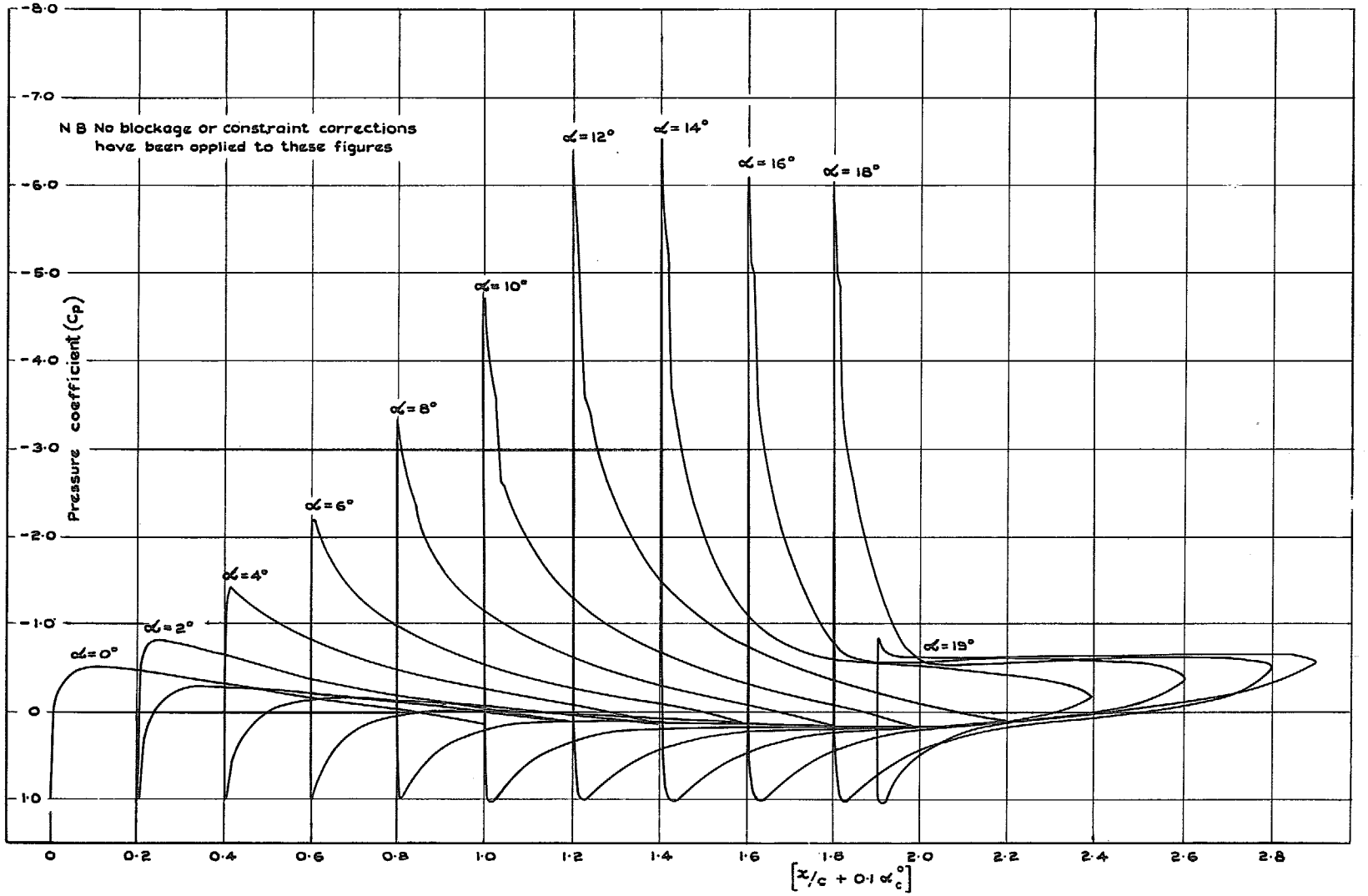

FIG. 30. Chordwise pressure distribution-incidence carpet $R_c = 1{\cdot}33 \times 10^6$, 12·2% t/c RAE 100.

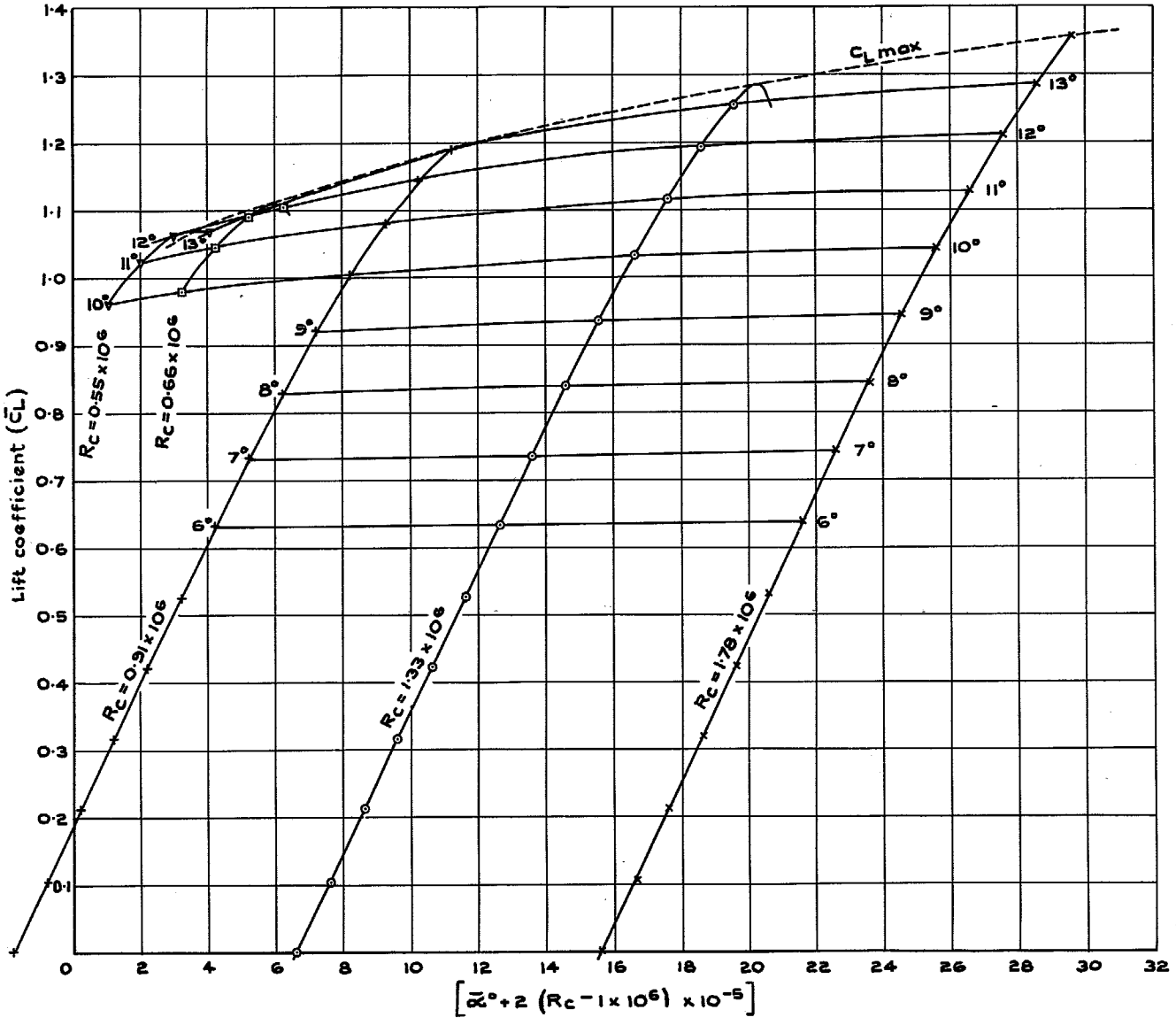

FIG. 31. Pre-stall variation of lift coefficient with incidence and Reynolds number.

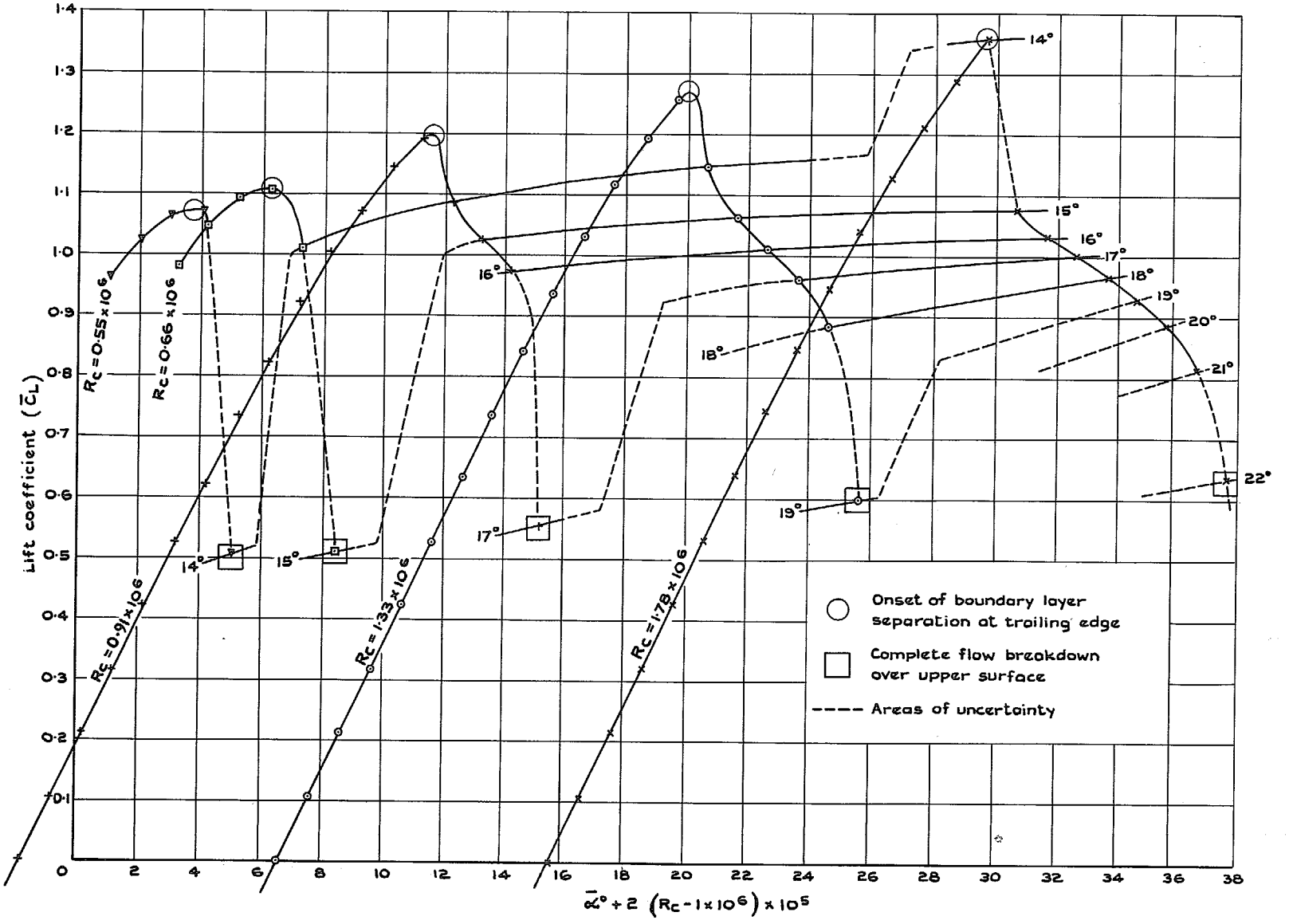

FIG. 32. Post-stall variation of lift coefficient with incidence and Reynolds number.

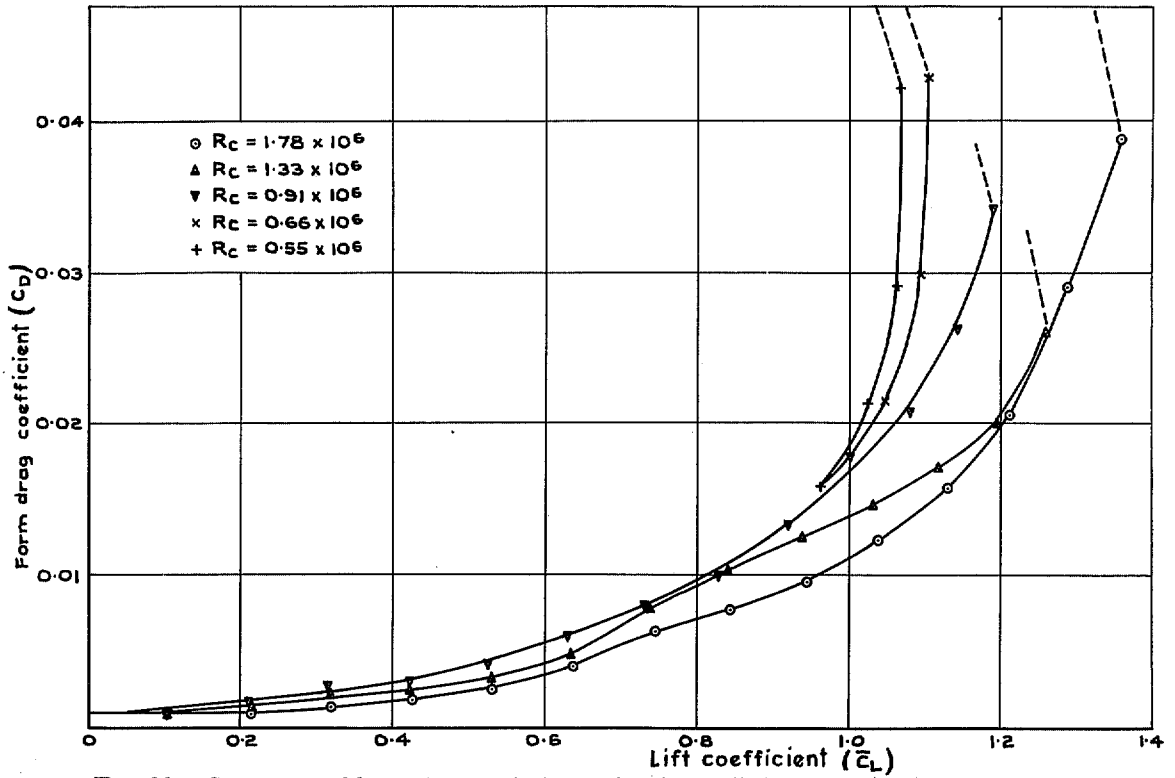

FIG. 33. Summary of form-drag variations with lift coefficient and Reynolds number.

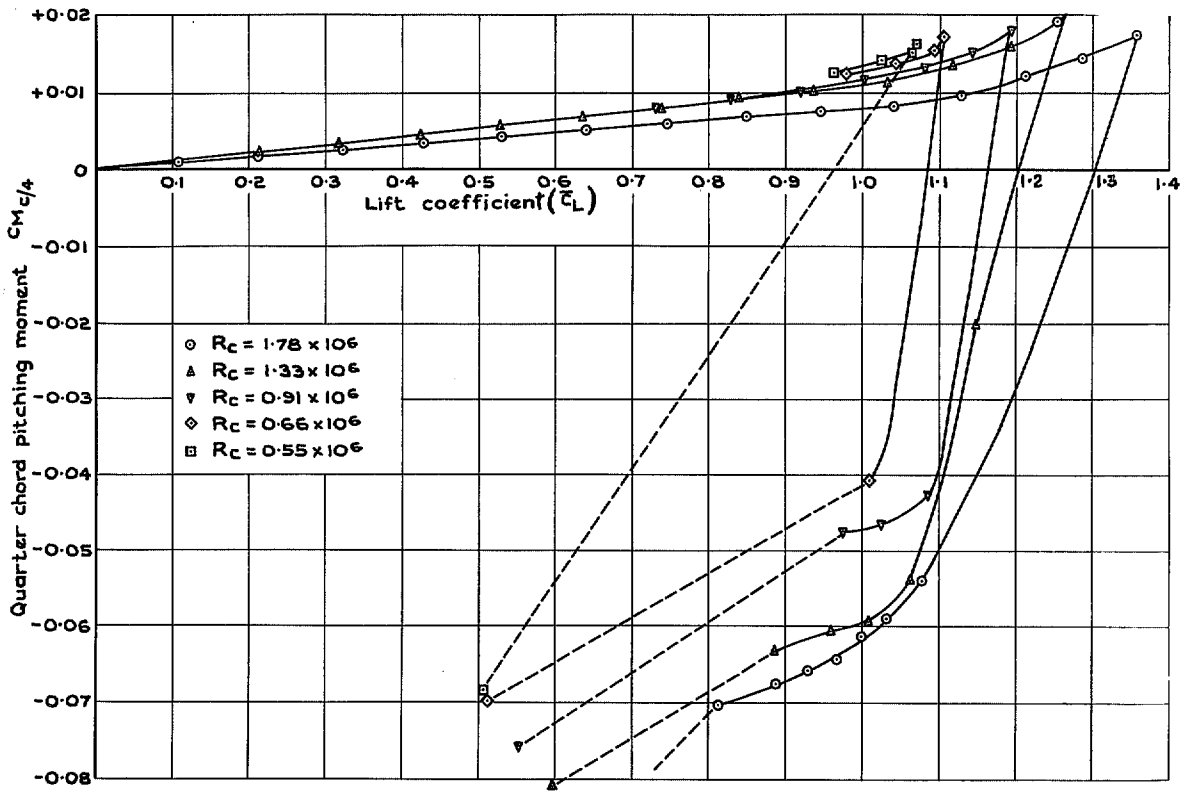

FIG. 34. Summary of $\frac{1}{4}$-chord pitching-moment variations with lift and Reynolds number.

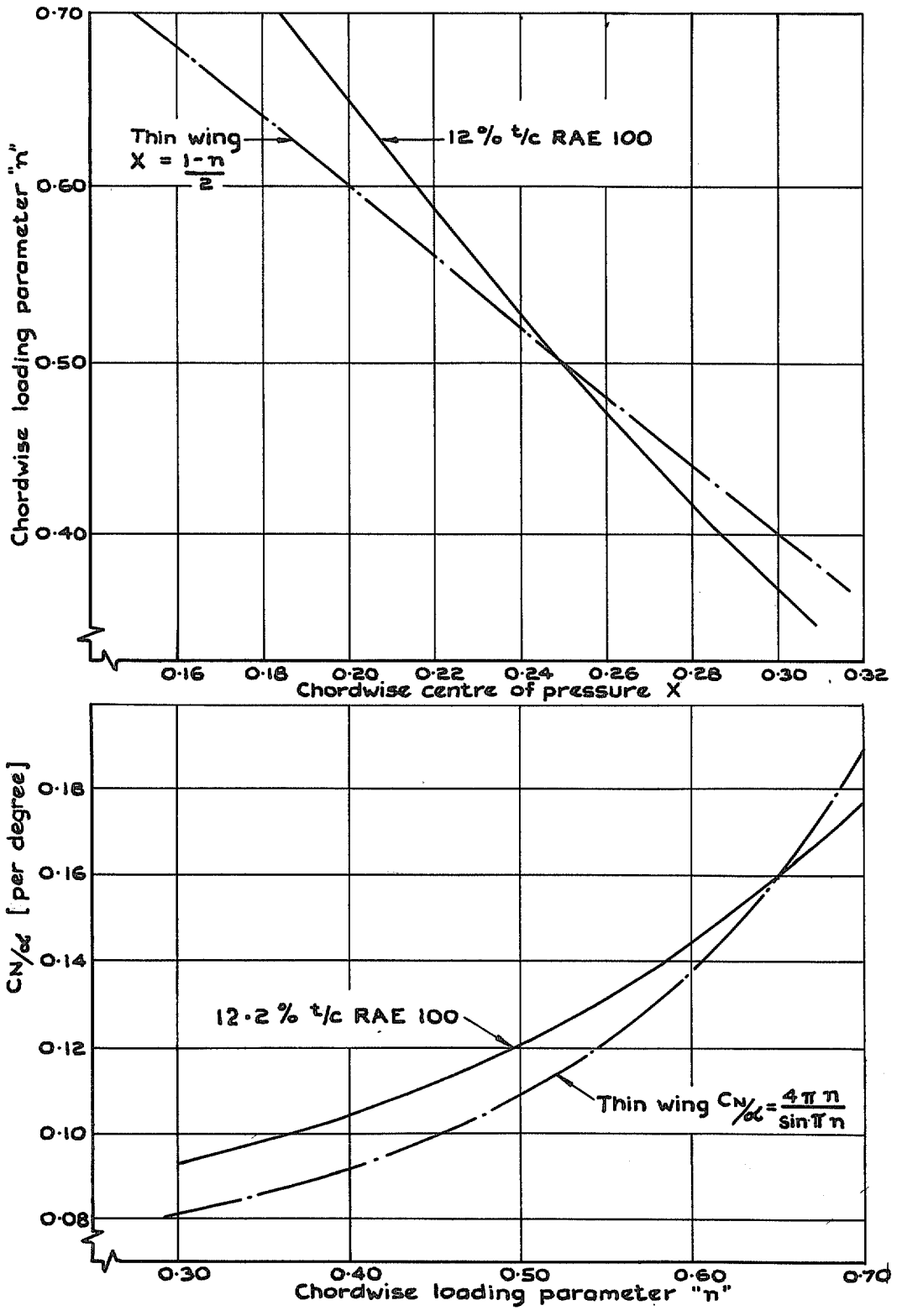

FIG. 35. Profile thickness effects on centre of pressure and normal-force/incidence slope.

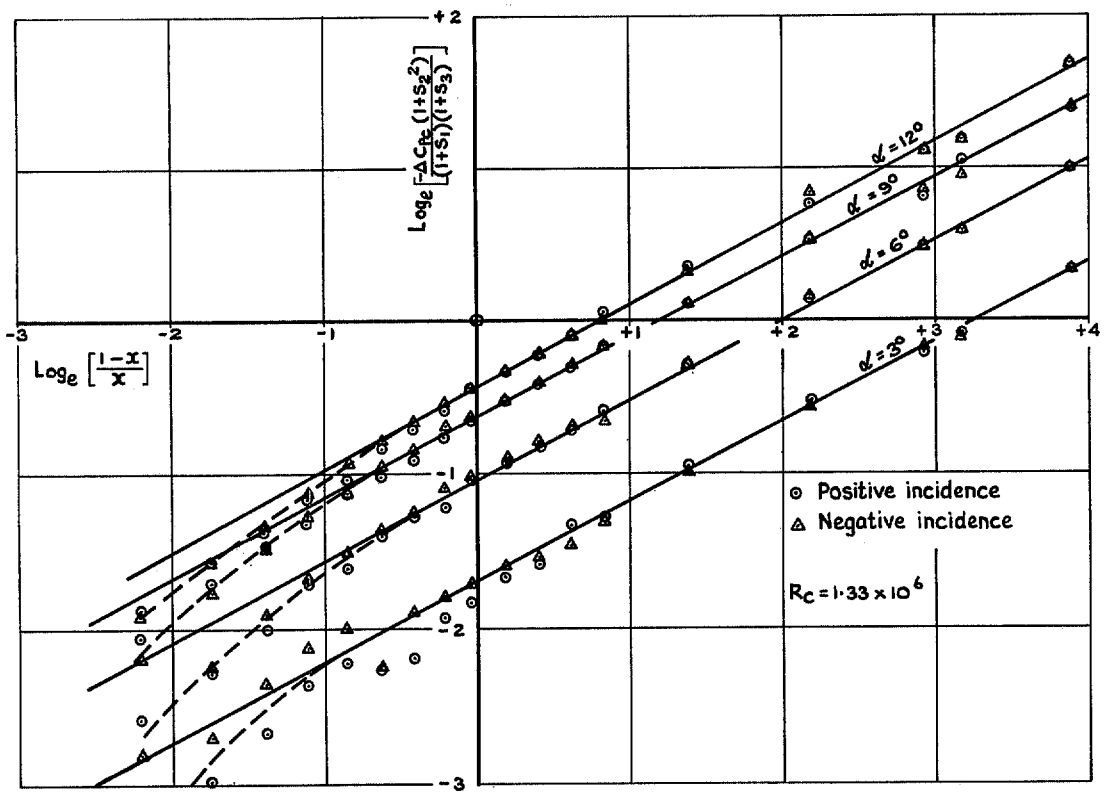

FIG. 36. Typical equivalent thin wing incidence loading analysis 12·2% thick RAE 100 aerofoil.

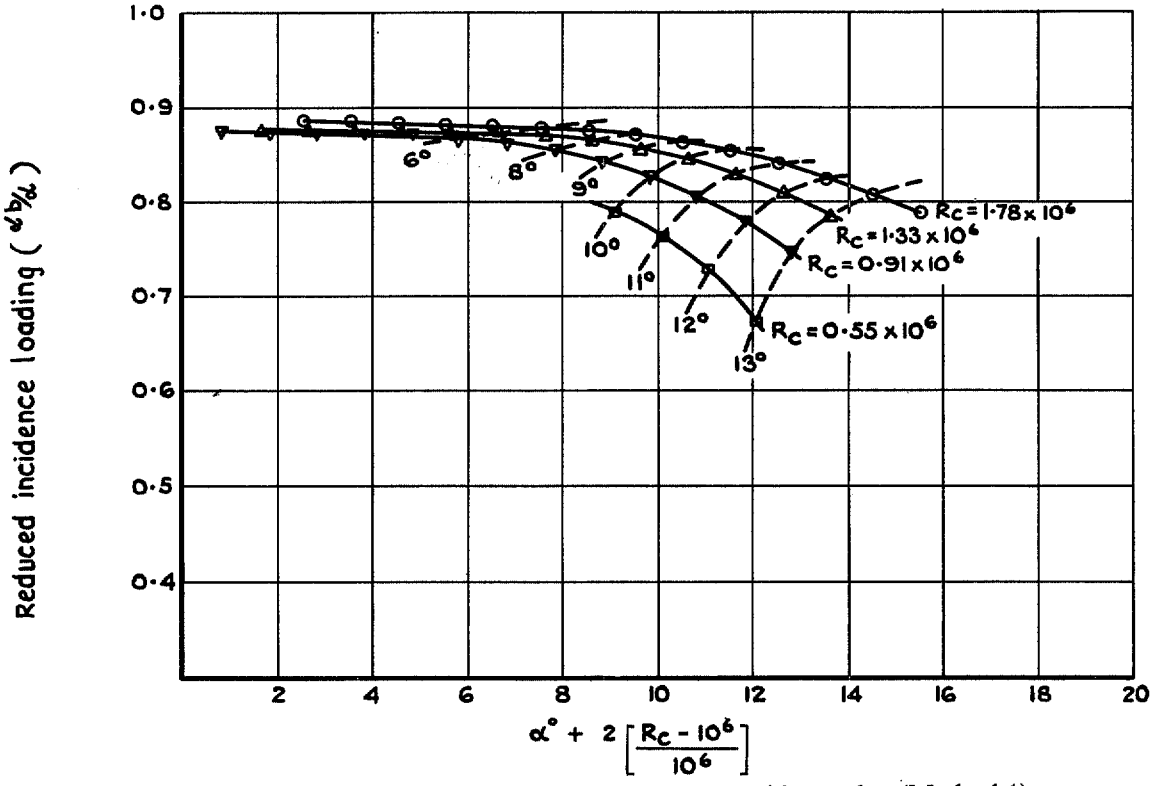

FIG. 37. Variation of reduced incidence and Reynolds number (Method 1).

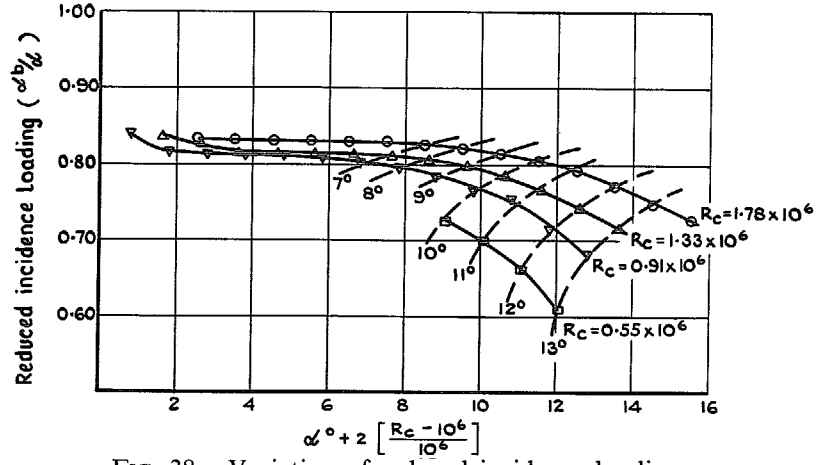

FIG. 38. Variation of reduced incidence loading with incidence and Reynolds number (Method 2).

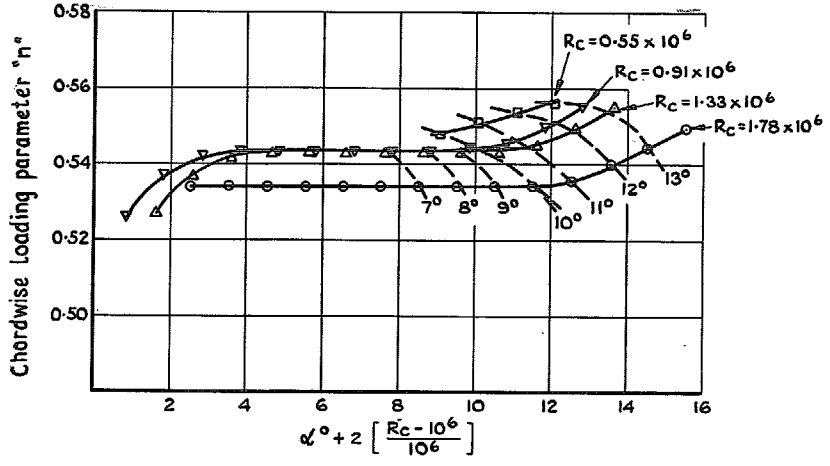

FIG. 39. Variation of chordwise loading parameter with incidence and Reynolds number (Method 2).

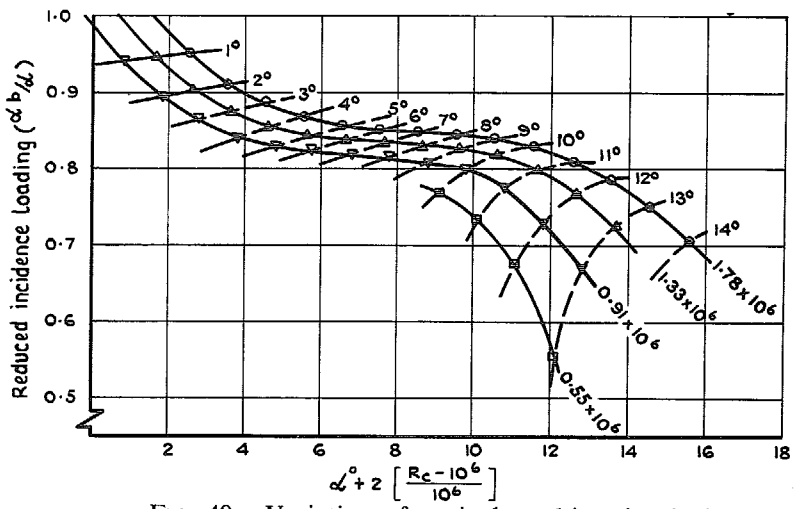

FIG. 40. Variation of equivalent thin wing incidence with incidence and Reynolds number (Method 3).

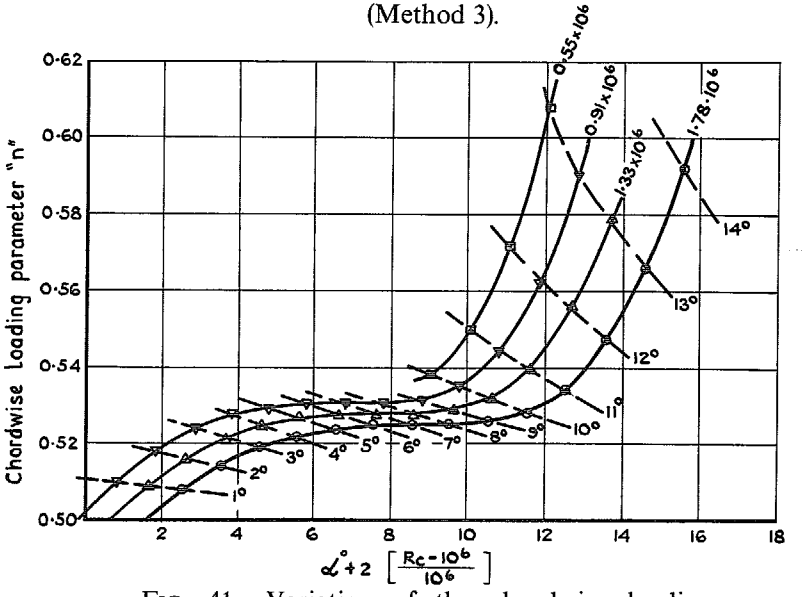

FIG. 41. Variation of the chordwise loading parameter 'n' with incidence and Reynolds number

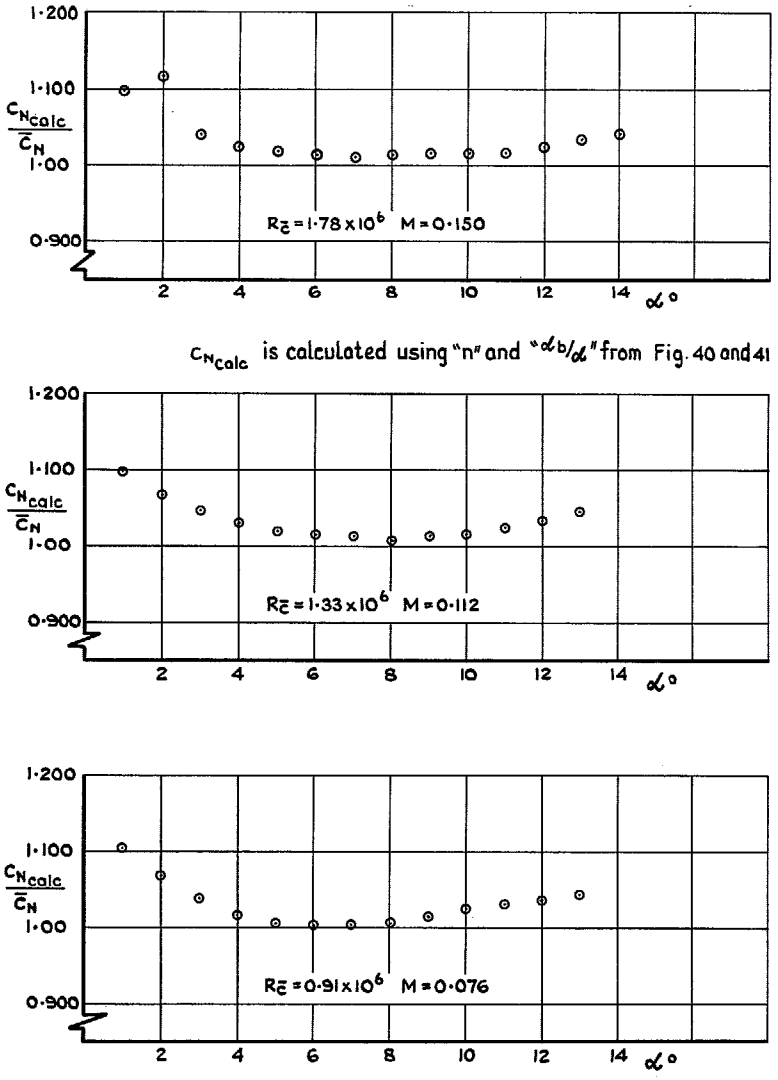

FIG. 42. Comparison of experimental values of $\bar{C}_N$ and those calculated from modified values of 'n' and 'α' (Method 3).

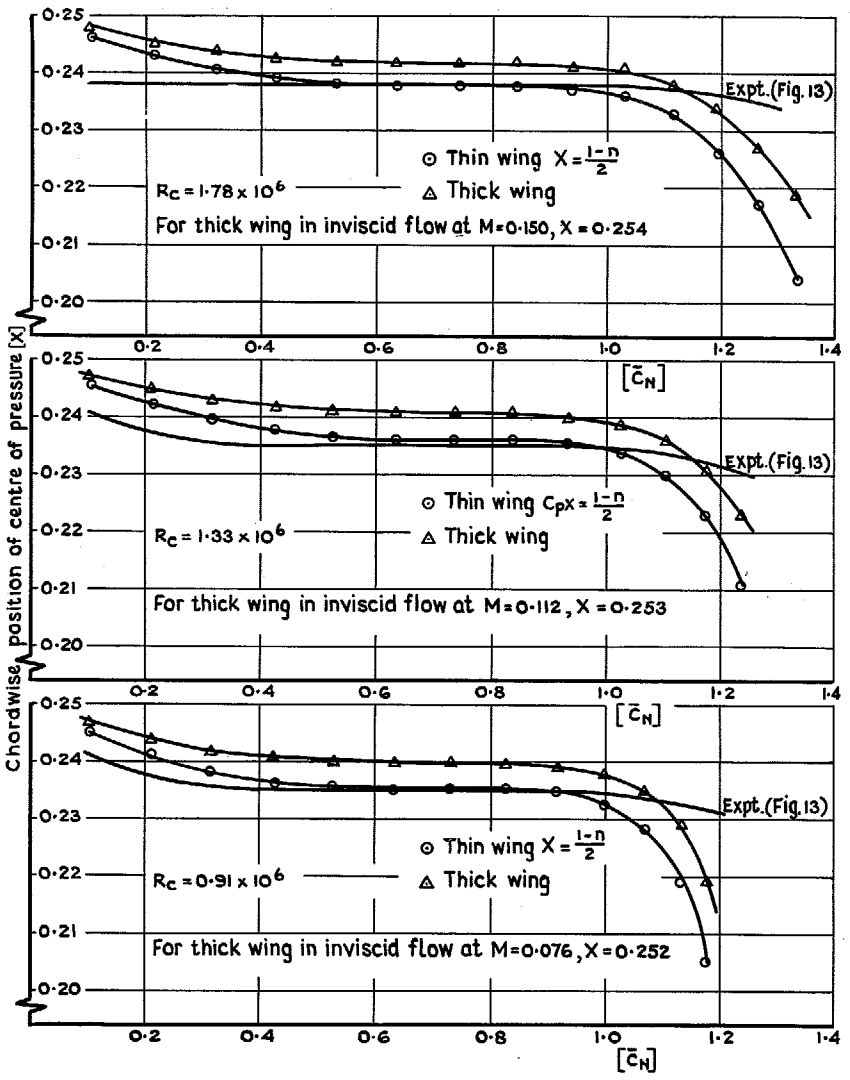

FIG. 43. Comparison of experimental values of X and those calculated by Method 3.

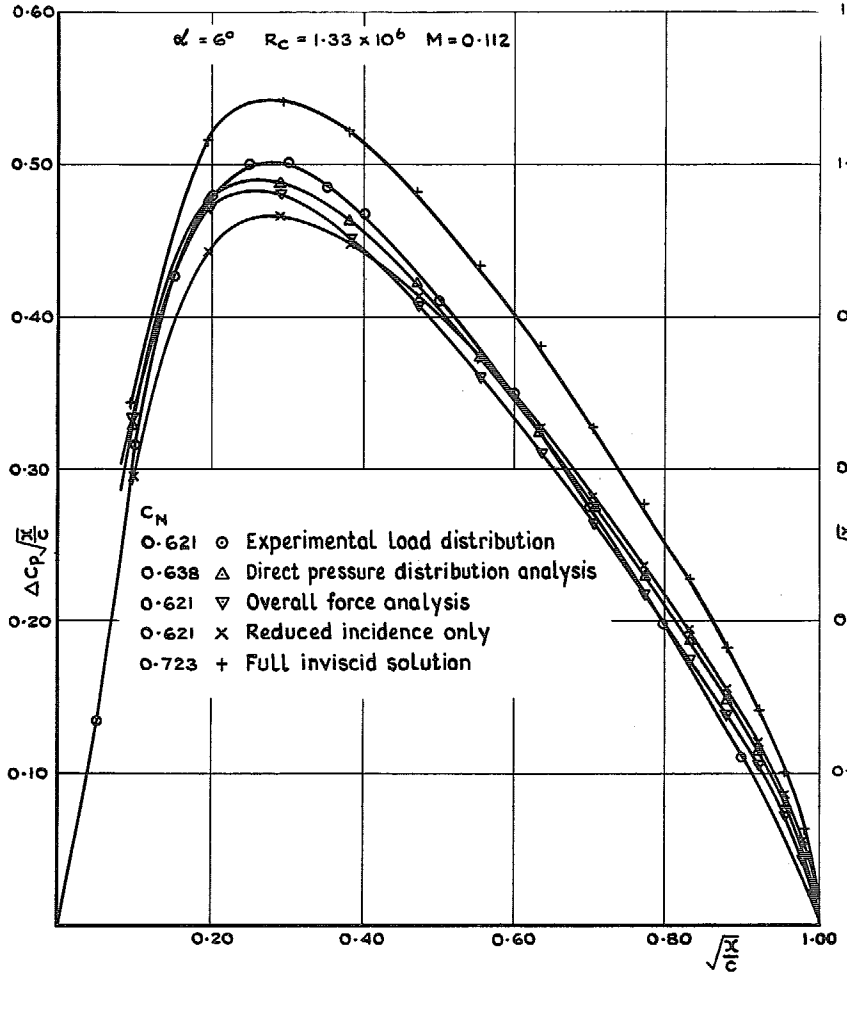

FIG. 44. Comparison of experimental and modified theoretical load distributions.

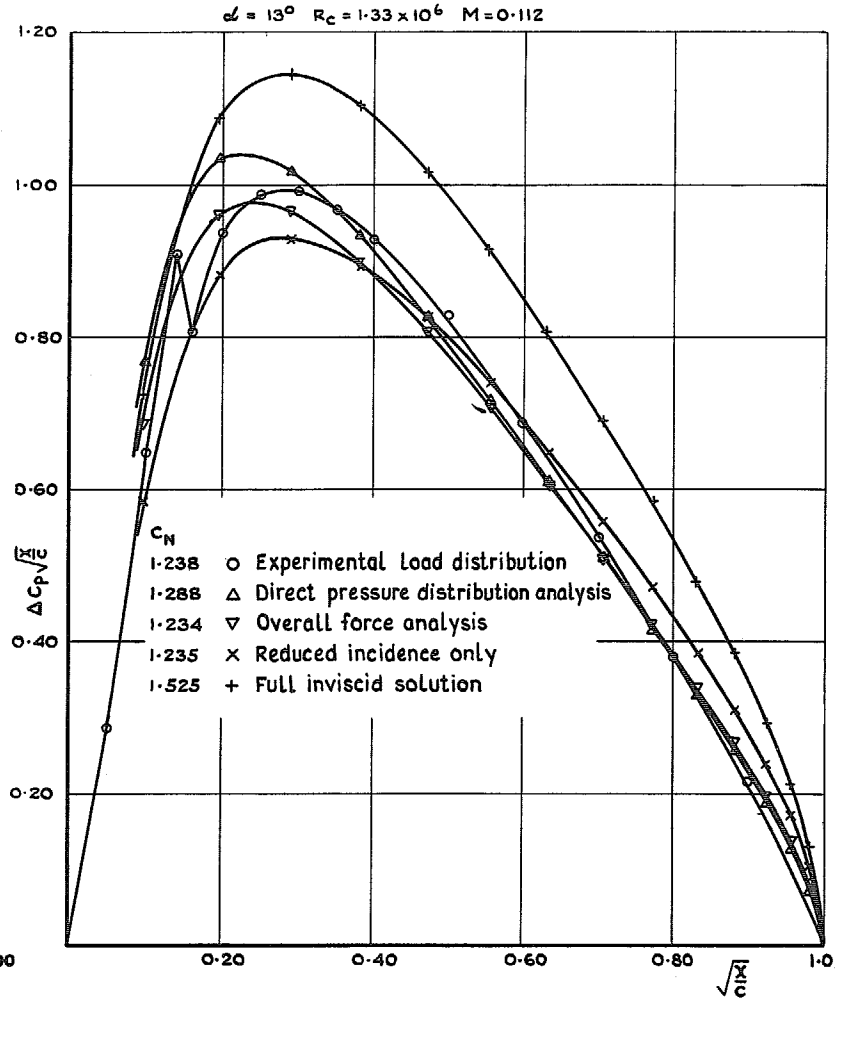

FIG. 45. Comparison of experimental and modified theoretical load distributions.

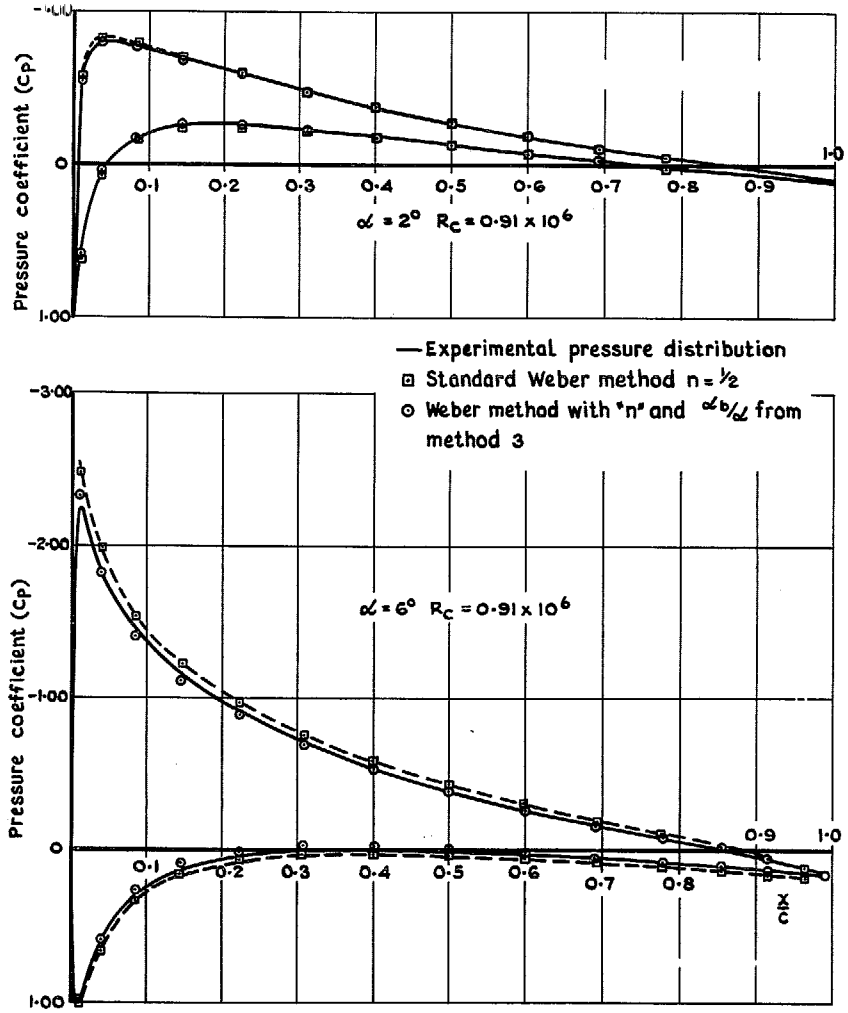

FIG. 46. Comparison of experimental and modified theoretical pressure distributions.

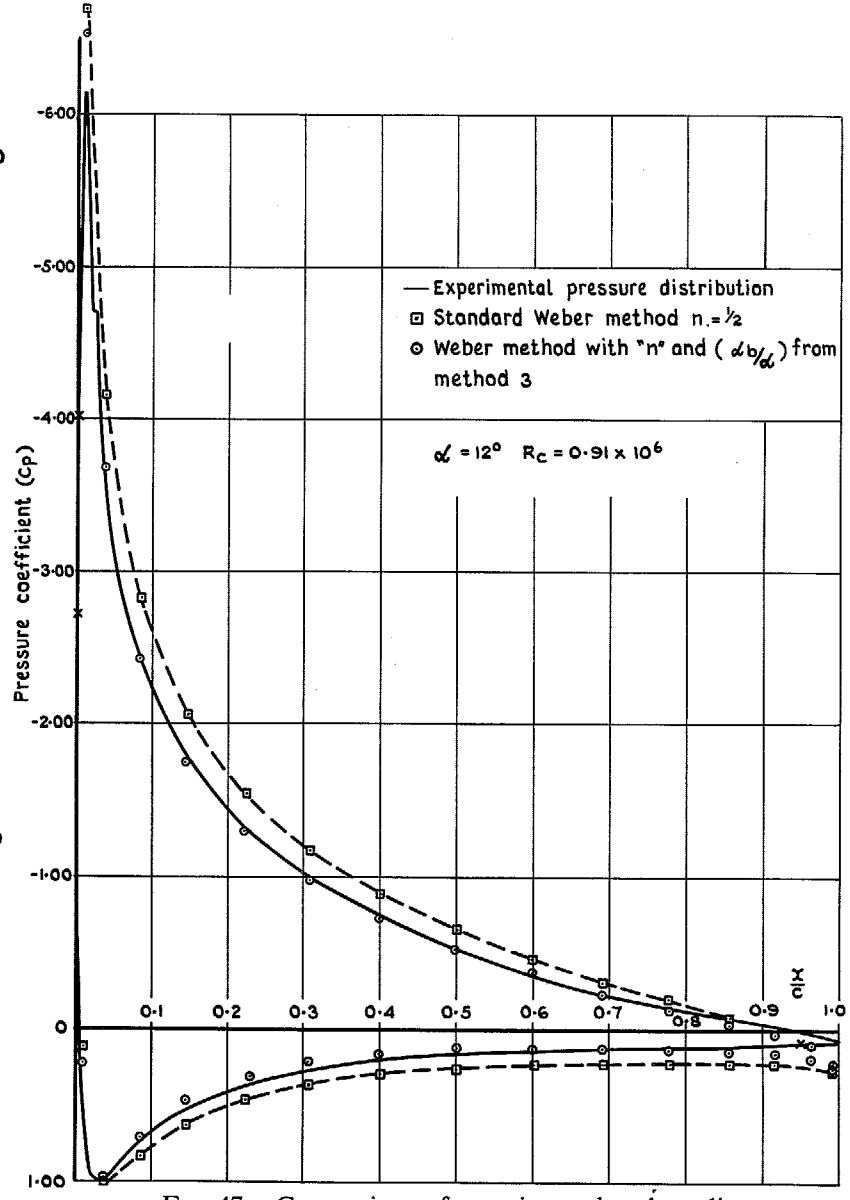

FIG. 47. Comparison of experimental and modified theoretical pressure distributions.

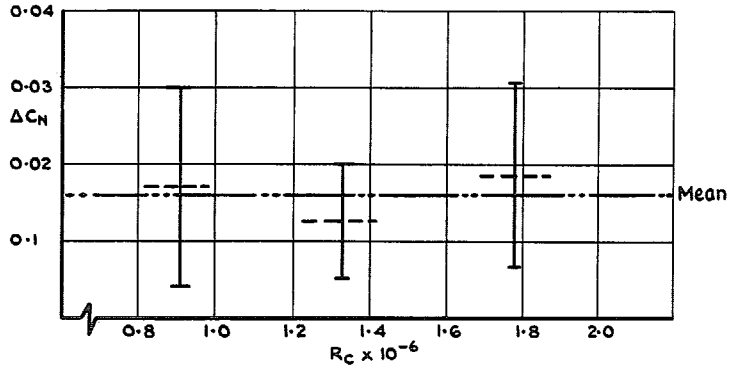

FIG. 48. Variation of ΔC_N due to flow camber with Reynolds number.

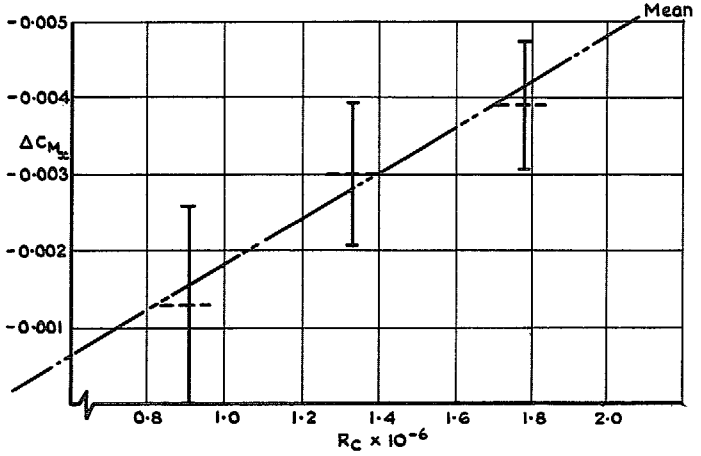

FIG. 49. Variation of ΔC_M due to flow camber with Reynolds number.

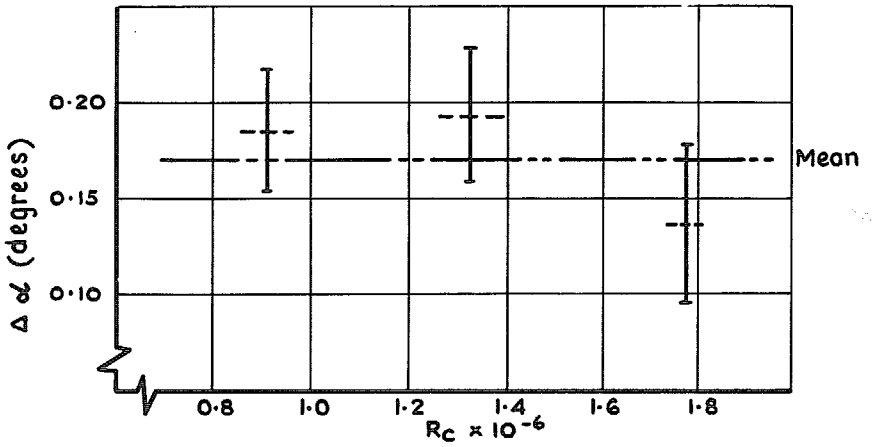

FIG. 50. Variation of $\Delta\alpha$ with Reynolds number.

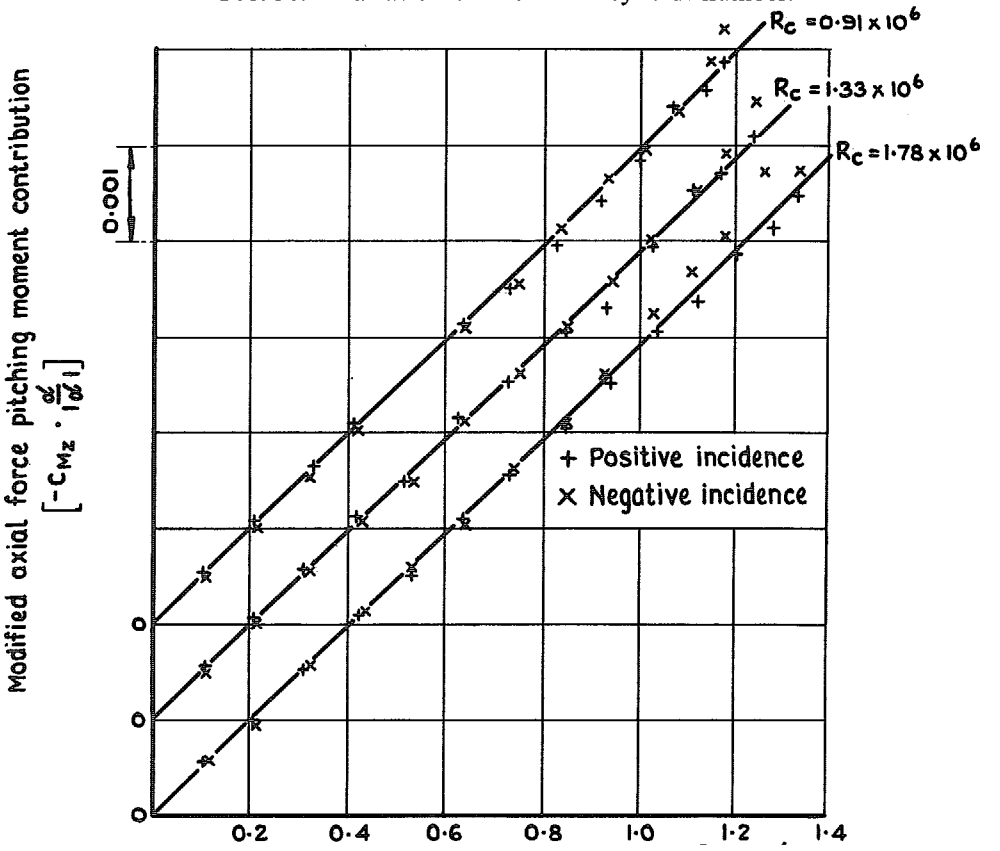

Printed in Wales for Her Majesty's Stationery Office by Allens Printers (Wales) Ltd.
Dd. 501372 K5.

Published by
HER MAJESTY'S STATIONERY OFFICE

To be purchased from
49 High Holborn, London WC1V 6HB
13a Castle Street, Edinburgh EH2 3AR
109 St Mary Street, Cardiff CF1 1JW
Brazennose Street, Manchester M60 8AS
50 Fairfax Street, Bristol BS1 3DE
258 Broad Street, Birmingham B1 2HE
7 Linenhall Street, Belfast BT2 8AY
or through booksellers

SBN 11 470368